NASA/CR—2019-220382

Feasibility of Electrified Propulsion for Ultra-Efficient Commercial Aircraft Final Report

D.K. Hall, E.M. Greitzer, A.P. Dowdle, J.J. Gonzalez,
W.W. Hoburg, J.H. Lang, J.S. Sabnis, and Z.S. Spakovszky
Massachusetts Institute of Technology, Cambridge, Massachusetts

B. Yutko, C. Courtin, W. Thalheimer, L. Trollinger, J. Tylko, and N. Varney
Aurora Flight Sciences, Cambridge, Massachusetts

A. Uranga, S. Byahut, and M. Kruger
University of Southern California, Los Angeles, California

December 2019

NASA STI Program . . . in Profile

Since its founding, NASA has been dedicated to the advancement of aeronautics and space science. The NASA Scientific and Technical Information (STI) Program plays a key part in helping NASA maintain this important role.

The NASA STI Program operates under the auspices of the Agency Chief Information Officer. It collects, organizes, provides for archiving, and disseminates NASA's STI. The NASA STI Program provides access to the NASA Technical Report Server—Registered (NTRS Reg) and NASA Technical Report Server—Public (NTRS) thus providing one of the largest collections of aeronautical and space science STI in the world. Results are published in both non-NASA channels and by NASA in the NASA STI Report Series, which includes the following report types:

- TECHNICAL PUBLICATION. Reports of completed research or a major significant phase of research that present the results of NASA programs and include extensive data or theoretical analysis. Includes compilations of significant scientific and technical data and information deemed to be of continuing reference value. NASA counter-part of peer-reviewed formal professional papers, but has less stringent limitations on manuscript length and extent of graphic presentations.

- TECHNICAL MEMORANDUM. Scientific and technical findings that are preliminary or of specialized interest, e.g., "quick-release" reports, working papers, and bibliographies that contain minimal annotation. Does not contain extensive analysis.

- CONTRACTOR REPORT. Scientific and technical findings by NASA-sponsored contractors and grantees.

- CONFERENCE PUBLICATION. Collected papers from scientific and technical conferences, symposia, seminars, or other meetings sponsored or co-sponsored by NASA.

- SPECIAL PUBLICATION. Scientific, technical, or historical information from NASA programs, projects, and missions, often concerned with subjects having substantial public interest.

- TECHNICAL TRANSLATION. English-language translations of foreign scientific and technical material pertinent to NASA's mission.

For more information about the NASA STI program, see the following:

- Access the NASA STI program home page at http://www.sti.nasa.gov

- E-mail your question to help@sti.nasa.gov

- Fax your question to the NASA STI Information Desk at 757-864-6500

- Telephone the NASA STI Information Desk at 757-864-9658

- Write to:
  NASA STI Program
  Mail Stop 148
  NASA Langley Research Center
  Hampton, VA 23681-2199

NASA/CR—2019-220382

Feasibility of Electrified Propulsion for Ultra-Efficient Commercial Aircraft Final Report

D.K. Hall, E.M. Greitzer, A.P. Dowdle, J.J. Gonzalez,
W.W. Hoburg, J.H. Lang, J.S. Sabnis, and Z.S. Spakovszky
Massachusetts Institute of Technology, Cambridge, Massachusetts

B. Yutko, C. Courtin, W. Thalheimer, L. Trollinger, J. Tylko, and N. Varney
Aurora Flight Sciences, Cambridge, Massachusetts

A. Uranga, S. Byahut, and M. Kruger
University of Southern California, Los Angeles, California

National Aeronautics and
Space Administration

Glenn Research Center
Cleveland, Ohio 44135

December 2019

Acknowledgments

Level of Review: This material has been technically reviewed by NASA expert reviewer(s).

Feasibility of Electrified Propulsion for Ultra-Efficient Commercial Aircraft Final Report

D.K. Hall, E.M. Greitzer, A.P. Dowdle, J.J. Gonzalez,
W.W. Hoburg, J.H. Lang, J.S. Sabnis, and Z.S. Spakovszky
Massachusetts Institute of Technology
Cambridge, Massachusetts 02139

B. Yutko, C. Courtin, W. Thalheimer,
L. Trollinger, J. Tylko, and N. Varney
Aurora Flight Sciences
Cambridge, Massachusetts 02142

A. Uranga, S. Byahut, and M. Kruger
University of Southern California
Los Angeles, California 90089

Program Abstract

MIT, Aurora Flight Sciences, and USC have collaborated to assess the feasibility of electric, hybrid-electric, and turbo-electric propulsion for ultra-efficient commercial transportation. The work has drawn on the team expertise in disciplines related to aircraft design, propulsion-airframe integration, electric machines and systems, engineering system design, and optimization. A *parametric trade space* analysis has been carried out to assess vehicle performance across a range of transport missions and propulsion architectures to establish how electrified propulsion systems scale. An *optimization approach* to vehicle conceptual design modeling was taken to enable rapid multidisciplinary design space exploration and sensitivity analysis. The results of the analysis indicate vehicle aero-propulsive integration benefits enabled by electrification are required to offset the increased weight and loss associated with the electric system and achieve enhanced performance; the report describes the *conceptual configurations* than can offer such enhancements. The main contribution of the present work is the definition of *electric vehicle design attributes* for potential efficiency improvements at different scales. Based on these results, key areas for future research are identified, and extensions to the trade space analysis suitable for higher-fidelity electrified commercial aircraft design and analysis have been developed.

Contents

References   **93**

1 Executive Summary

This document describes the research process and results of an investigation of the feasibility of electrified propulsion for ultra-efficient commercial aircraft. The work was carried out by a multiorganizational, interdisciplinary team of Aurora Flight Sciences, Massachusetts Institute of Technology (MIT), and University of Southern California (USC). MIT was the lead organization. The term electrified propulsion encompasses turbo-electric systems, in which a gas turbine engine is the prime mover, all electric aircraft powered by batteries, as well as hybrid combinations of these.

The objectives of the project, as stated in the proposal, were:

- Definition of the *right size, right architecture, and right mission* for electrified aircraft propulsion,
- Quantification of *vehicle benefits*,
- Development of *conceptual exploration/design tools*, and
- Identification of enabling technologies and advances required.

To address these, the team explored the configuration trade space of commercial aircraft having electrified propulsion systems. Four categories of aircraft were examined:

1. Thin Haul, nominal 500 nautical mile (nmi) range, 20 passengers payload;
2. Regional, nominal 1500 nmi, 80 passengers;
3. Medium Haul, 3000 nmi, 180 passengers; and
4. Long Haul, 6000 nmi, 350 passengers.

The performance evaluation was carried out using GPkit, a recently developed approach to aircraft performance evaluation and optimization using geometric programming. GPkit provided an enhanced capability to link the aircraft performance to the physical specifications of the components, rather than relying mainly on correlation based performance determination.

We identified the potential of different configurations: full or partial turbo-electrics, all electric (batteries), and hybrids. We addressed feasibility and efficiency; the metric used was *onboard energy usage per payload-range*. The trade space was defined in terms of configurations to be evaluated. The assessments show the potential benefits, but they do not define the specific designs needed to achieve these benefits. As an example, boundary layer ingestion (BLI) and distributed propulsion (DP) can be achieved by many methods; what is assessed in this document is the effect of these features.

The results show that electrified propulsion systems lead to feasible commercial aircraft. In terms of feasibility, battery powered aircraft are not likely candidates for an airliner.[1] There are substantial benefits, roughly 25% reduction in energy consumption, from DP, both from weight saving and propulsive efficiency improvement, and BLI. The configurations that show the largest benefits are different than current aircraft in the use of large amounts of DP and BLI. Some of the benefits may be achievable without electrified propulsion, e.g., with mechanically enabled distributed propulsion.

An important finding is the strong linkage between distributed propulsion and boundary layer ingestion and the use of electrified propulsion. The benefits of electrified propulsion are facilitated by large amounts of distributed propulsion and boundary layer ingestion; large amounts of distributed propulsion and boundary layer ingestion are facilitated by electrified propulsion.

Figures 1.1 and 1.2 show a summary of the results. The figures give the *productivity-specific energy consumption* (PSEC) in units of kJ/kg-km for the four different missions, based on projections of aircraft and battery technology (see the report for the descriptions of how the projections were defined). Figure 1.1 illustrates that none of the all electric designs were feasible for the indicated missions, even with optimistic battery energy density assumptions. Figure 1.2 shows that if the range is reduced so the

---

[1]The usage here is that of Epstein and O'Flarity, 2018: "an aircraft with GTOW of greater than 30 tonnes."

designs do close, i.e., the aircraft are feasible, there are all electric configurations in the thin haul range that can be attractive, as described further in the report.

The report also summarizes issues that we did not address and poses specific questions for further research.
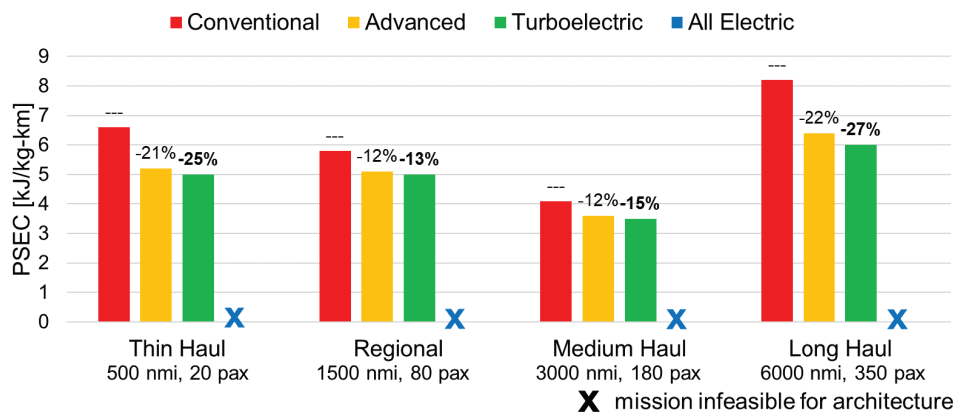

Figure 1.1: Productivity-Specific Energy Consumption (PSEC) versus mission and architecture; design range.
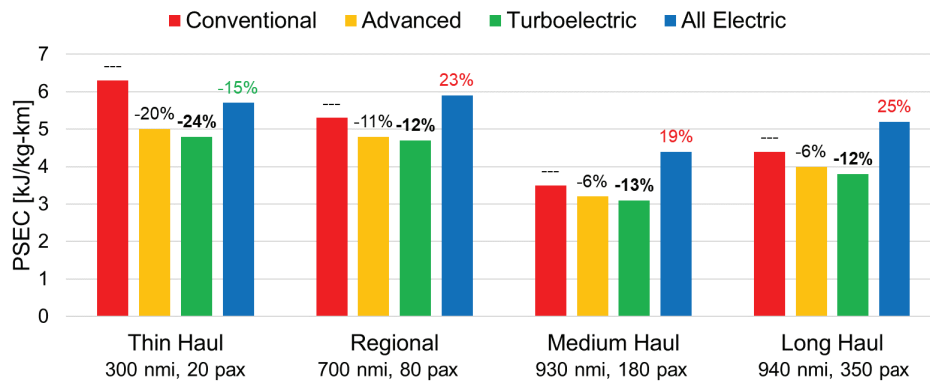

Figure 1.2: Productivity-Specific Energy Consumption (PSEC) versus mission and architecture; range reduced to enable all-electric architecture.

2 Objectives and Metrics

2.1 Program Objectives

This project aims at exploring the design space of aircraft with electrified propulsion systems, to determine the benefits, if any, of electrification over conventional propulsion in terms of *onboard energy usage*. The goal is to define the missions, aircraft configurations, and architectures, if any, for which the use of electrified aircraft could be advantageous.

The present work is a system study at the vehicle level. The metric for evaluating aircraft performance is thus chosen to be the onboard energy required to complete a given mission (i.e., bring a certain payload from one point to another), carried as a combination of hydrocarbon fuel and/or batteries that are assumed to be fully charged at take-off. Considerations of how the electrical energy is generated to originally charge the batteries are outside the scope of this work. Comments on this choice of metric are given in Section 2.2.

The focus is on commercially viable aircraft, and we thus consider only aircraft with a minimum capacity of 20 passengers. The design space extends to long-range aircraft with missions of 350 passengers and 6,000 nmi range.

We consider a variety of propulsion architectures. Current civil aircraft burn hydrocarbon fuel in gas turbine engines, generating mechanical shaft power that turns turbofans or propellers to generate thrust. An electrified aircraft can have one of three types of propulsion system architectures. A *turbo-electric* aircraft burns hydrocarbon fuel through gas turbines, which are connected to a generator that converts the energy into electricity, which is then used to run motors driving fans or propellers. An *all-electric* aircraft replies solely on batteries as the source of energy for propulsion. A *hybrid-electric* aircraft uses both hydrocarbon fuel with gas turbines and batteries as sources of energy.

There are some potential benefits that electrified propulsion offers over conventional propulsion. The components in the power-conversion chain from energy source to propulsion of an electric architecture (generator, converter, motor) have higher efficiencies than those in a conventional architecture (gas turbine, mechanical shaft). Electrified propulsion systems also facilitate the use of beneficial technologies, such as distributed propulsion (DP) and boundary layer ingestion (BLI), which can reduce energy consumption for a given mission.

There are also drawbacks of electrified propulsion. First, battery specific energy is much lower than the specific energy (energy per unit mass) of hydrocarbon fuels. The energy stored onboard hybrid- or all-electric aircraft is thus heavier than for conventional and turbo-electric aircraft. Electrified systems thus do not provide benefits if they are simply used in place of conventional engines. The design space needs to be opened to different aircraft configurations to realize the potential benefits of electrified propulsion.

A "clean-sheet" approach to propulsion system architecture design is presented in this report, using a generalized range equation for mission analysis with subsystem models based on parametrically defined component sizing and performance sizing relation (e.g., power densities and efficiencies). The range equation is used in a high-level framework to determine the fundamental trade-offs for electrified aircraft and to narrow the design space to regions that offer the most benefits from electrification. A higher-fidelity framework was also developed for specific component and subsystem point-design optimization and to look at sensitivities to various parameters. This modular framework enables use of different component models with varying levels of fidelity and complexity as required by the analysis.

The major questions answered by this work include:

- Are there missions (and if yes, which ones) for which electrification provides an onboard energy-usage advantage compared to hydrocarbon-based propulsion?
  - Can an all-electric aircraft be advantageous for a commercial mission (more than 20 passengers)?

- What level of technology (battery specific energy, motor size, etc.) would be needed for a regional / medium-haul / long-haul all-electric aircraft to be feasible?
- Is a turbo-electric architecture advantageous and when?
- Can a hybrid-electric architecture be beneficial and when?

- Is leveraging distributed propulsion and boundary layer ingestion enough to enable electrification?

2.2 Performance Metrics

A suitable metric is needed to evaluate various aircraft with different propulsion architectures. A key metric used in the air breathing propulsion industry is the thrust-specific fuel consumption (TSFC), which measures the fuel burned per unit thrust for an aircraft. This metric cannot be applied to electrified aircraft, since for hybrid-electric and all-electric architectures, part or all of the energy is stored in batteries. As a result, the metric needs to consider energy from both batteries and fuel and must be able to compare across different architectures.

The aircraft studied have stored energy onboard in the form of hydrocarbon fuel carried in the wings or the airframe, and/or electrical energy in the form of a battery that is fully charged at takeoff. Onboard energy is used as the performance metric. Considerations related to production of electrical energy to charge the batteries on the ground and the corresponding chain for hydrocarbon fuel delivery are outside the scope of this work. In other words, a "well-to-wake" analysis is not pursued for this work.

The energy use is defined in terms of *onboard energy storage*, but another possibility considered would have been to expand our control volume for the energy usage to include the fuel needed, in a ground based power generation, to fully charge the battery. If we take the grid to have the same overall efficiency as the turbofan engine of Ref. [1], this means the energy needed to charge the battery is *roughly* twice the useful electrical energy or, more relevantly, that the PSEC numbers for all-electric aircraft would, again roughly, double. We recognize, however, that electrical power generation is not necessarily related to fuel usage (e.g., wind, nuclear) and that there is another set of circumstances.[2] In recognition of these uncertainties, and to give all-electric the greatest chance to succeed, we have set the criterion as onboard energy and taken the battery at the start of flight to be fully charged.

2.2.1 Productivity-Specific Energy Consumption

The performance metric we use the productivity-specific energy consumption, defined as the mission energy per payload mass per unit range

$$\text{PSEC} = \frac{m_{\text{fuel}} h_{\text{fuel}} + m_{\text{batt}} \text{BSE}}{m_{\text{payload}} R} , \tag{2.1}$$

where m_{fuel}, m_{batt}, and m_{payload} are the masses of the fuel, battery,[3] and the payload respectively, h_{fuel} is the specific energy of hydrocarbon fuel, BSE is the battery specific energy, and R is the mission range. Thus, PSEC is a measure of the onboard energy required to bring passengers from point A to point B, and accounts for how efficiently the energy is used to perform that mission. The analysis only considers cruise fuel assumption without accounting for reserves, and the results should thus only be considered an assessment of the relative difference in performance between architectures for a given mission.

---

[2]In the most optimistic scenario, fossil fuels are no longer used, and the energy cost to produce synthetic hydrocarbons would be counted against the fuel energy in the larger system control volume.

[3]When a battery is on board, it is assumed to be fully charged at takeoff.

2.2.2 Terminology

Throughout this work, the term *conventional* is used to refer to a propulsion system architecture that uses hydrocarbon fuel as the sole source of energy and includes no electrical components for propulsion. A *turbo-electric* architecture refers to a propulsion system that retains the hydrocarbon fuel as the sole energy source, but employs electrical components in the conversion from source to load: one or more gas turbines generate power that is distributed to one or more fans through a component chain of a generator, converter, and motor. In a *fully turbo-electric* architecture, all the fans are electrically driven, whereas a *partial turbo-electric* design has both electrically and mechanically driven fans.

A *hybrid-electric* architecture relies on both batteries and hydrocarbon fuel to store energy for propulsion. Hybrid-electric architectures could be further classified as either *series* or *parallel*. In series, the propulsors receive only electrical power from the turbo-generator and the battery, whereas in parallel, the mechanical fans receive additional power from a battery-powered motor mounted on the same shaft as the turbine. Finally, in an *all-electric* architecture all the energy needed for propulsion is stored in batteries.

The term "*electrified*" is used to refer to a propulsion system that uses electrical components to generate thrust. It therefore encompasses turbo-electric, hybrid-electric and all-electric architectures.

2.2.3 Electrification Metrics

We parameterize the propulsion system based on on power split at the source and the load. The *source electrification factor*, f_S, quantifies the fraction of power supplied by batteries (electrical source), P_{batt}, versus that supplied by hydrocarbon fuel (mechanical source), P_{turb}. It is defined as

$$f_S = \frac{P_{\text{batt}}}{P_{\text{batt}} + P_{\text{turb}}} \, , \tag{2.2}$$

where the denominator is the total power. Conventional and turbo-electric aircraft have $f_S = 0$, hybrid-electrics have f_S between 0 and 1, and all-electrics have $f_S = 1$.

Useful load power is quantified by the mechanical flow power delivered by the propulsors, P_K, as defined by Drela [2]. Electrification of the load relates the flow power delivered via mechanically-driven propulsors (mechanical load), $P_{K,m}$, and via electrically-driven propulsors (electrical load), $P_{K,e}$. The *load electrification factor* is defined as

$$f_L = \frac{P_{K,e}}{P_{K,e} + P_{K,m}} \, , \tag{2.3}$$

where the denominator represents total power required by the propulsors. A conventional aircraft has $f_L = 0$, since all the flow power is mechanical. Partial turbo-electric and hybrid aircraft have f_L between 0 and 1. Fully turbo-electric and all-electric aircraft have $f_L = 1$. Load electrification thus distinguishes between partial and fully turbo-electric, as well as between hybrid- and all-electric architectures.

The entire design space of electrified propulsion architectures can be described by the two parameters f_S and f_L, providing a unified view of electrified propulsion systems.

2.3 Potential Electrification Benefits

2.3.1 Source to Load Conversion Efficiency

The chain of efficiencies from energy source to propulsor (fan or propeller), is shown in Fig. 2.1. New turbofan engines have overall efficiencies of roughly 40%, with gas turbines thermal efficiency of near 60% [3]. For an all-electric, battery-powered propulsion system, the efficiencies of the electrical components in the chain (motors and power electronics) can give an overall efficiency from source to propulsor of around 70% or more [1].
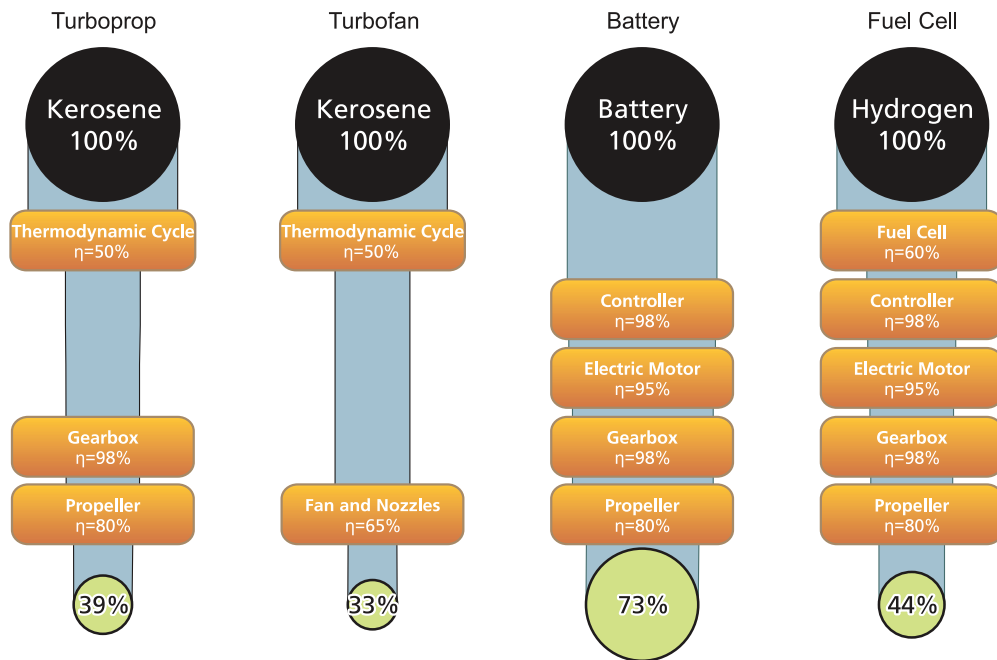
Figure 2.1: Potential energy-to-power conversion efficiency benefit of electric and hybrid-electric propulsion (from [1]).

Even if the propulsion system is only partly electrified, the higher electrical component efficiencies can be exploited with hybrid-electric and turbo-electric propulsion system architectures. Electrical components efficiencies are expected to reach values greater than 99% [4, 5], further improving the efficiency of electrified propulsion systems.

2.3.2   Boundary Layer Ingestion (BLI)

In a conventional engine installation, the propulsors are mounted away from the airframe. They ingest uniform free stream flow and their jets counteract the momentum defect in the airframe wake. At cruise, the jets and wakes sum to zero net momentum (thrust equals drag), but both the airframe wake and the propulsor jet represent wasted kinetic energy. A more efficient alternative is to place the propulsors in the boundary layer of the airframe, so they ingest the slower-moving fluid, as illustrated in Fig. 2.2. The resulting combined wake and jet has lower kinetic energy and lower losses than a conventional propulsor.

The process of having at least part of the airframe boundary layer ingested by the propulsion system is called boundary layer ingestion (BLI), and it is known [6–8] to increase the overall efficiency. The benefits of BLI come from four sources: (i) reduced propulsor jet dissipation and corresponding increased propulsive efficiency (this is the main source); (ii) reduced wake dissipation as the propulsors partially eliminate the wake; (iii) potential for reduced nacelle drag with smaller embedded nacelles with lower surface velocities; and (iv) potential for reduced aircraft weight due to a lighter, more efficiency propulsion system.

The level of benefit that BLI provides relative to a conventional engine installation is a function of the amount of boundary layer ingested. The largest benefits are realized when the entire boundary layer is ingested, but achieving full ingestion requires that the propulsor system inlets cover all the airframe trailing edges (including fuselage, wings, and tails). This can be difficult to realize in practice, especially if only a small number of large propulsors are to be used. One way to increase BLI is use of distributed
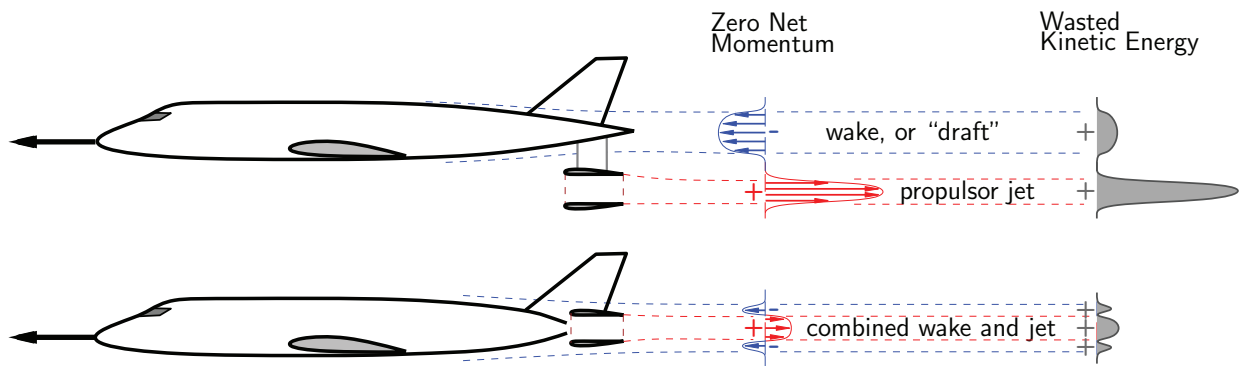
Figure 2.2: Illustration of the aerodynamic benefit of boundary layer ingestion [6].

propulsors integrated into the airframe, configurations than may be easier to achieve when power is distributed to the propulsors electrically, rather than mechanically via shafts.

2.3.3 Distributed Propulsion

Distributed propulsion (DP) can enable increased BLI, and it can also provide a weight reduction benefit. This can be seen by considering the relation between the propulsor mass and the mass flow through it. The mass of a propulsor, m_{prop}, can be assumed to scale roughly with its volume and hence with the cube of the characteristic length. The propulsor mass flow, $\dot{m}_{\mathrm{prop}}$, however, scales with its frontal area, represented by the characteristic length squared. The mass of a propulsor and the mass flow rate are thus linked by a cube-square relationship:

$$m_{\mathrm{prop}} \sim \dot{m}_{\mathrm{prop}}^{3/2}, \tag{2.4}$$

and the thrust-to-weight ratio decreases with $\dot{m}_{\mathrm{prop}}^{3/2}$.

As an example, consider the use of four small DP units instead of a large one as in Fig. 2.3. If the single large propulsor is replaced by the DP system with the same total thrust, then for the same total fan area, the weight would be reduced by half (mass factor of square-root of the number of propulsors). If, instead, the requirement were to maintain the same propulsion system weight, the four-unit DP system would provide 1.6 times more total fan face area (mass flow factor of cubic root of the number of propulsors), enabling reduced fan pressure ratio and increased propulsive efficiency.

The use of a distributed propulsion system can thus be lighter or more efficient, and the larger the number of propulsors the better, at least in principle.
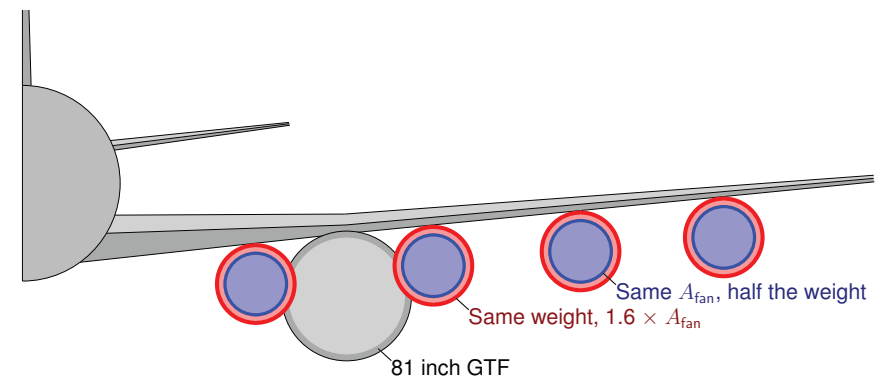
Figure 2.3: Illustration of distributed propulsion weight and propulsive efficiency benefits.

3 Technologies and Scenarios

A major performance driver for electrified aircraft is the mass of the electrical components. To determine the effect of technology on electrification, we consider three technology levels: current, conservative 2035, and optimistic 2035. Here, we present a rationale and values for the specific energy, power, and efficiencies used in the present work.

We model the electrical part of the propulsion system as a chain of components starting with the energy source (battery) and going to the electrical load (fans). For each electrical fan, an inverter converts the direct current from the battery to alternating current required to power the motor, which drives the fan to propel the aircraft. The battery, which works both as an energy and power source, is characterized by a specific energy and a specific power. The inverter and motor are defined by their specific power and efficiency. The efficiency is also used in sizing the thermal management system. The components in use today have low parameter values and are not specifically targeted for aerospace applications, but the trends in the future look encouraging [5].

3.1 Battery Technology

Battery specific energy (BSE) is defined as the energy per unit mass stored in a battery. The theoretical specific energy, $\mathrm{BSE_{th}}$, is set by the electrochemical reactions that generate the energy, and thus is based on the mass of the reactants only. In practice, batteries are made up of connections of several cells. Cell manufacturers quote the nominal capacity, Q_{nom}, nominal voltage, V_{nom}, and mass of the cell, to give the BSE at cell-level.

$$\mathrm{BSE_{cell}} \frac{V_{\mathrm{nom}}\, Q_{\mathrm{nom}}}{m_{\mathrm{cell}}} = \frac{[\text{voltage}] \times [\text{capacity}]}{[\text{cell mass}]} = \eta_{\mathrm{cell}}\, \mathrm{BSE_{th}} \tag{3.1}$$

The cell-level BSE includes the mass of electrodes (usually graphite), current collectors, electrolytes, separator, and binders, in addition to the mass of the reactants. As a result, $\mathrm{BSE_{cell}}$ can be expressed as an efficiency factor (less than unity) multiplying $\mathrm{BSE_{th}}$. The cell-level BSE is usually what is quoted in the literature.

A battery, made up of several cells in a pack, has additional mass due to the structure and the battery management system. Current high-energy density battery chemistries that include lithium-ion are susceptible to thermal runaway, caused by dendrite formation across the separator, leading to a short circuit, a large heat release, thermal runaway in neighboring cells, and the potential for a fire. As a result, a battery management system (BMS) is needed. The BMS, which monitors each cell for dendrite formation and isolates damaged cells to prevent thermal runaway, adds mass to a battery, thus lowering the BSE further at pack level.

The additional mass is included in a BSE defined at the pack level, which is the relevant parameter for electrified aircraft system level considerations.

$$\mathrm{BSE_{pack}} = \frac{N_{\mathrm{cell}} V_{\mathrm{nom}} Q_{\mathrm{nom}}}{m_{\mathrm{bat}}} = \frac{N_{\mathrm{cell}}\, m_{\mathrm{cell}}}{m_{\mathrm{bat}}}\, \mathrm{BSE_{cell}} = \eta_{\mathrm{pack}}\, \mathrm{BSE_{cell}} = \eta_{\mathrm{pack}}\, \eta_{\mathrm{cell}}\, \mathrm{BSE_{th}} \tag{3.2}$$

Mature batteries such as nickel-cadmium and nickel-metal-hydride achieve a cell efficiency of less than 40%. Lithium-ion chemistries, which are less mature, already exhibit cell efficiencies of around 30%. The Li-ion batteries used in the Boeing 787 and the Tesla Model S have cell efficiencies of 28% and 36% respectively; at the pack level, the BSE values are 78% and 59% respectively of the cell-level values [9, 10]. The all-electric Airbus E-Fan aircraft achieves a higher pack efficiency of 84% [11]. Pack efficiencies are expected to improve as cell manufacturers focus on improving not just cell chemistries of batteries, but also packaging materials.

Given the values of the cell and pack efficiencies, current lithium-ion chemistries are unlikely to yield a pack-level BSE of more than 250 W·h/kg in the 2035 time frame. Novel lithium-ion chemistries, like lithium sulfur (Li-S) and lithium-air (Li-air), with theoretical BSE values of 2600 W·h/kg and 3500 W·h/kg respectively, do offer substantially higher BSE potential. Li-air cells have been demonstrated to reach a BSE of 778 W·h/kg [12], which translates to a pack value of 540 W·h/kg with a pack efficiency of ∼70%.

A literature survey of conceptual hybrid-electric and all-electric designs is illustrated in Fig. 3.1, which gives a range of cell-level BSE predictions plotted against the envisioned entry-into-service (EIS) of the proposed aircraft. Conceptual designs such as the Boeing SUGAR Volt have assumed cell-level BSE between 500-2000 W·h/kg in the 2030s decade [13]. Although the authors do not mention the specific battery chemistries, it is assumed these predictions are for novel lithium chemistries. Tesla Motors predicts a growth rate of between 5% to 8% per year, which, starting from a 2012 value of 265 W·h/kg for the Model S car, leads to a value between $700-1300$ W·h/kg in 2035. Using a theoretical value BSE of 740 W·h/kg for current lithium-ion chemistries (like the $LiNiCoAlO_2$ in the Boeing 787), and an overall efficiency ($\eta_{pack}\,\eta_{cell}$) of 33%, the pack BSE is predicted to be about 250 W·h/kg in 2035. Using the same process for novel lithium chemistries, like Li-S (with $BSE_{th} = 2600$ W·h/kg), the pack BSE is predicted to be about 900 W·h/kg in 2035.

In terms of power, a battery is characterized by the battery specific power (BSP), defined as the maximum power available per unit mass. It is not possible to set BSP without taking into account battery discharge profiles, which vary widely between batteries and their use. We choose instead to fix the ratio of BSE to BSP at the value for NASA's X-57 Maxwell batteries [14], 1200 sec. To account for technological improvements, we assume that BSP improves with BSE, while their ratio remains fixed. The pack BSP is predicted to reach between 745–2700 W/kg in 2035.
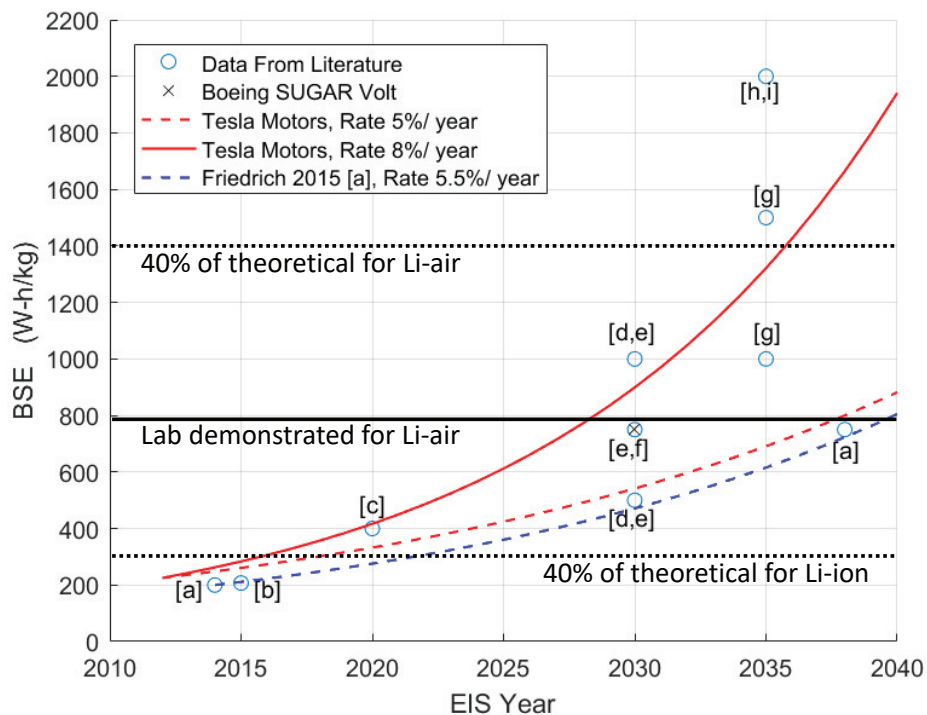
Figure 3.1: Cell-level BSE projections.

3.2 Electric Machine Technology

Electric machines, specifically motors and generators, are rated based on power. They are modeled here as having specific power and efficiency as parameters. Commercial-off-the-shelf (COTS) motors have specific powers of around 2 kW/kg and are rated in the 100 kW range. Motors for large electrified aircraft need to be in the megawatt class. A conservative 2035 estimate for motors predicts specific powers of 9 kW/kg, rated at 2 MW [4]. However, NASA is currently funding motor research for aerospace applications with motors rated between 1.0–2.5 MW at specific powers of up to 16 kW/kg [5], some of which are superconducting, but self-cooled. These levels are expected to be achieved on test-beds in the near term. Current motors are about 95% efficient, and this efficiency is projected to grow to 98–99% by 2035 [4, 5].

Superconducting designs are predicted to reach higher specific powers, as in the boxed data points in Fig. 3.2, and higher efficiencies. However, they need cryocoolers to reach the low temperatures required for superconductivity. The addition of a cryocooler adds complexity, and reduces the specific power at the overall system level. As a result, superconducting designs which require cryocoolers have not been considered here.

3.3 Power Electronics Technology

Similar extrapolations have been made for converters and inverters (collectively termed power electronics). Existing power electronics have power and specific power levels of 200 kW and 2.2 kW/kg respectively, not suitable for aerospace applications. Conservative power electronics parameter values are predicted to be 500 kW power and 9 kW/kg specific power by 2035 [4]. Based on the projects currently funded by NASA [5], optimistic estimates have been set at 19 kW/kg rated at 1 MW. Current power electronics are about 95% efficient, and are predicted to reach 98–99% efficiency by 2035 [4, 5].
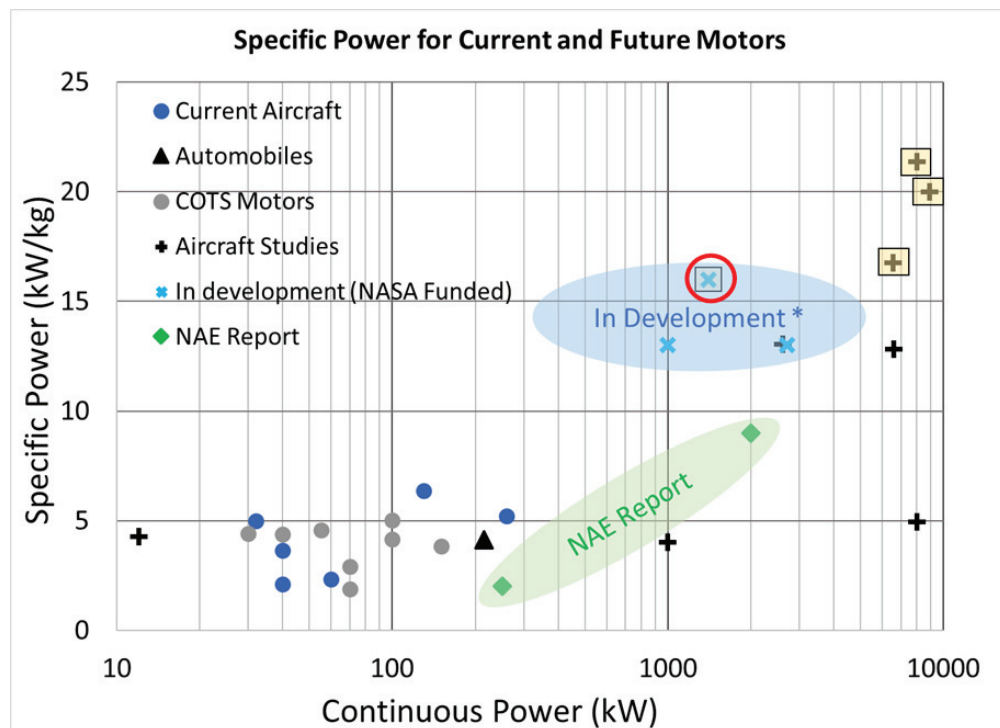
Figure 3.2: Electric machine specific power versus continuous power; existing machines and future design projections.
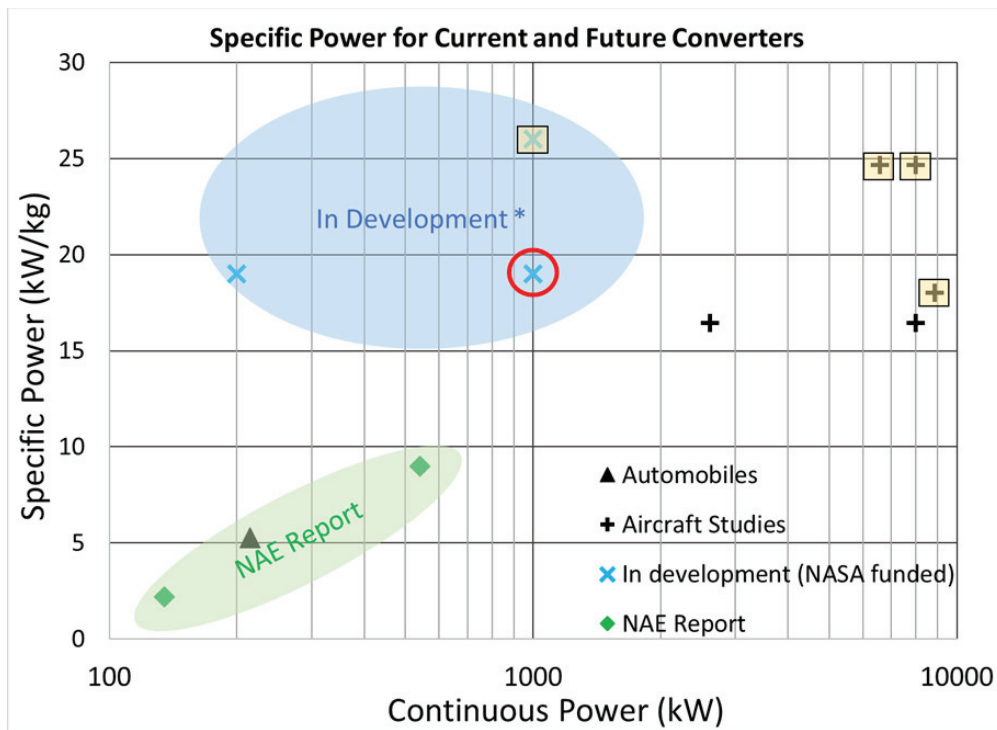
Figure 3.3: Power electronics specific power versus continuous power; existing designs and future design projections.

3.4 Electric Technology Scenario Assumptions

Table 3.1 summarizes the current and predicted 2035 technology scenarios. The current BSE was taken from the all-electric two-seater Airbus E-Fan. Conservative 2035 BSE assumes no new breakthroughs in battery chemistries, whereas the optimistic value assumes novel battery chemistries that are made rechargeable and commercialized by that time. In all three cases, the BSP scales with the BSE based on the BSE/BSP ratio for the NASA X-57 Maxwell [14].

For the other electrical components, the current and conservative specific powers and efficiencies are taken from [4]. Ongoing NASA-funded research programs project higher values [5], and these form the basis of the optimistic 2035 assumptions.

Table 3.1: Technology scenario assumptions

Parameter	Current State-of-the-Art	Conservative 2035	Optimistic 2035
Pack BSE (W·h/kg)	175	250	900
Pack BSP (W/kg)	520	745	2700
Motor Specific Power (kW/kg)	2	9	16
Converter Specific Power (kW/kg)	2.2	9	19
Electric Component Efficiency	0.95	0.98	0.99

4 Modeling Approach

This section describes the analysis and optimization approach used to assess aircraft performance for different missions and propulsion architectures. The details of the subsystem models are provided in Appendix A. Extensions of the trade space analysis, to higher fidelity models for electric components and aircraft conceptual design, are discussed in Section 6.

4.1 Air Vehicle Design Trade Space Model

A modular approach is taken to aircraft sizing and performance, as indicated schematically in Fig. 4.1, which shows the various subsystem models and the connections between them. The input variables to the configuration performance model are fuselage geometry, payload, range, and cruise speed – which define the overall mission – and energy source, propulsor load electrification and amount of BLI – which define the propulsion architecture.
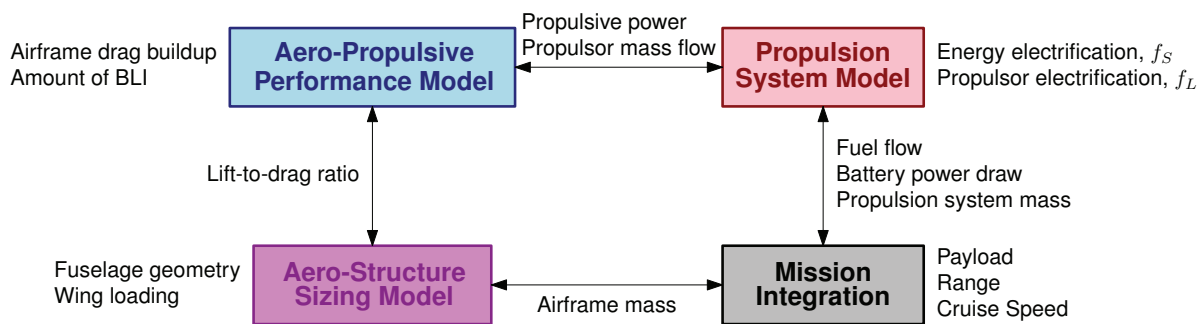
Figure 4.1: Modular approach to electrified aircraft performance trade space analysis.

4.1.1 Mission Integration

The overall vehicle fuel and battery energy consumption are found using an augmented Breguet range equation analysis for the general hybrid case with both fuel and battery energy storage. The fuel consumption is assessed assuming the fuel flow rate is proportional to the vehicle mass as fuel is consumed (e.g., for constant lift-to-drag ratio and thrust-specific fuel consumption). Under this assumption, the total mass of the vehicle is,

$$m(t) = m_{\text{TO}} \exp\left(-\frac{\dot{m}_{\text{fuel}}}{m}t\right), \tag{4.1}$$

where m_{TO} is the takeoff mass at time $t = 0$. Integrating Eqn. (4.1) over a mission of range R at velocity V yields an expression for the total fuel consumption.

$$\frac{m_{\text{fuel}}}{m_{\text{TO}} - m_{\text{fuel}}} = \exp\left(\frac{R}{V}\frac{\dot{m}_{\text{fuel}}}{m}\right) - 1 \tag{4.2}$$

The electrical energy consumption is determined assuming the battery discharge rate is also proportional to vehicle mass (i.e., f_S is constant). The total battery energy consumption, E_{batt}, is found using a similar integration of Eqn. (4.1) over the mission.

$$E_{\text{batt}} = m_{\text{TO}} \frac{(\dot{E}_{\text{batt}}/m)}{(\dot{m}_{\text{fuel}}/m)} \left[1 - \exp\left(-\frac{R}{V}\frac{\dot{m}_{\text{fuel}}}{m}\right)\right]. \tag{4.3}$$

For a given mission, PSEC is proportional to the sum of the fuel and battery energy, which can be related to their masses through the battery specific energy and fuel heating value,

$$E_{\text{total}} = E_{\text{batt}} + E_{\text{fuel}} \tag{4.4}$$

$$= m_{\text{batt}}\text{BSE} + m_{\text{fuel}}h_{\text{fuel}}. \tag{4.5}$$

Each configuration examined is sized for a single design point, with a takeoff mass, m_{TO}, including empty airframe and propulsion system masses described below, battery and fuel energy storage mass, and a specified payload,

$$m_{\text{TO}} = m_{\text{airframe}} + m_{\text{prop}} + m_{\text{batt}} + m_{\text{fuel}} + m_{\text{payload}}. \tag{4.6}$$

4.1.2 Aero-Structure Performance and Sizing

The airframe mass is estimated based on approximate sizing methods [15] for fuselage, wing, and tail areas, based on specified fuselage dimensions. The wing is sized for a specified wing loading, (W/S),

$$S_{\text{wing}} = \frac{m_{\text{TO}}}{(W/S)}, \tag{4.7}$$

and the horizontal and vertical tail are sized as a function of the fuselage and wing size using tail volume coefficients.

The aircraft aerodynamic efficiency, characterized by the lift-to-drag ratio, L/D, is estimated as a function of the wing aspect ratio and ratio of wing area to total airframe wetted area,

$$\frac{L}{D} = K_{(L/D)}\text{AR}\sqrt{\frac{S_{\text{wing}}}{S_{\text{wet}}}}. \tag{4.8}$$

The maximum aspect ratio for a given span is seen to always give the best performance; the performance can be calculated from a specified maximum span, b_{max}, and the wing area from Equation (4.7),

$$\text{AR} = \frac{b_{\text{max}}^2}{S_{\text{wing}}}. \tag{4.9}$$

The wing sizing and performance formulation described in Equations (4.7)-(4.9) captures trades involving airframe weight and aerodynamic efficiency that are important in the sizing and overall performance of electric vehicles. For battery-powered systems, the increase in energy-to-power conversion efficiency over conventional gas turbine systems trades against the weight of the low energy-density energy storage and reduced vehicle aerodynamic efficiency. This is illustrated conceptually in Fig. 4.2. The figure shows notional aero-structure sizing for equivalent vehicles with conventional and all-electric propulsion architectures. The all-electric vehicle weighs more than the conventional vehicle for the same mission, and for constant span and wing loading, this leads to decreased aspect ratio and lift-to-drag ratio.

4.1.3 Aero-Propulsive Performance

The vehicle mass and aerodynamic performance are related to the propulsion system power requirements using the power balance method [2], which allows treatment of BLI using the unpowered airframe performance. An integral form of the general power balance equation [8] is used to relate the

Conventional   **All-Electric**
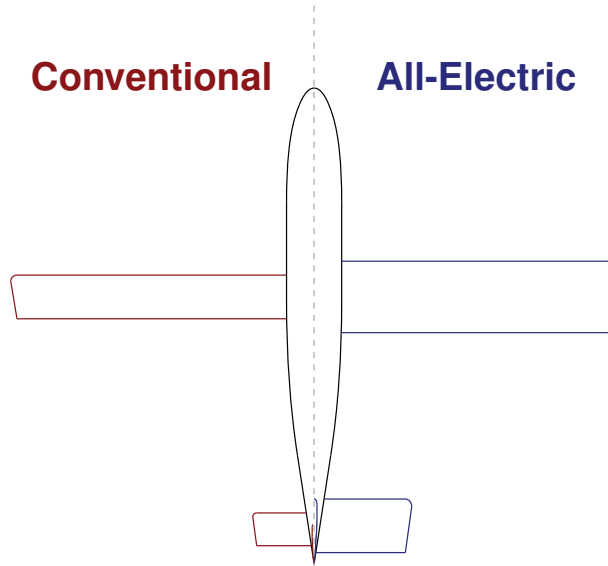
Figure 4.2: Notional conventional and all-electric vehicle planform shapes, illustrating the effect of takeoff weight on wing and tail sizing.

propulsor mass flow and jet velocity to the unpowered airframe drag as a function of a specified boundary layer ingestion fraction, f_{BLI}, and ratio of profile drag to total drag for the unpowered airframe, (D'_p/D'),

$$\dot{m}(V_{\text{jet}} - V_\infty) = \frac{m_{\text{TO}}}{L/D}\left[1 - f_{\text{BLI}}\left(\frac{D'_p}{D'}\right)\right]. \tag{4.10}$$

The propulsion system power requirement, as characterized by the mechanical flow power, P_K, is equal to the increase in mechanical energy imparted to the flow by the propulsor. It is calculated as a function of the propulsor mass flow, $\dot{m}$, jet velocity, V_{jet}, and the ingested dissipation in cases with BLI,

$$P_K = \frac{1}{2}\dot{m}(V_{\text{jet}}^2 - V_\infty^2) + f_{\text{BLI}}f_{\text{surf}}V_\infty\frac{m_{\text{TO}}}{(L/D)}, \tag{4.11}$$

where f_{surf} is the fraction of the airframe dissipation occurring in the fuselage boundary layer (approximately 0.9 for attached turbulent boundary layers). Equations (4.10) and (4.11) are evaluated on a per-propulsor basis (see Appendix A) to determine the power requirements in distributed and partial turbo- or hybrid-electric architectures.

4.1.4   Geometry Constraints for BLI Configurations

Constraints must also be included in the model to capture the aerodynamic trades of BLI. For example, a fan performing full fuselage BLI must be at least as large as the boundary layer. These constraints create an important trade in optimal fan size between BLI, and drag and weight. There are multiple ways to integrate propulsors to achieve BLI. Here, a ducted array of propulsors at the trailing edge performs wing BLI, a tail cone thruster performs full fuselage BLI, and two embedded fans perform partial fuselage BLI.

Wing BLI is subject to boundary layer height and spanwise geometry constraints. The fan diameter is set to be as large as the wing boundary layer thickness:

$$d_{\text{fan}} \geq \delta_{\text{wing}} = K_\delta \, c^{6/7} \tag{4.12}$$

where K_δ is 0.05 m$^{1/7}$.[4]

The array of N_{fan} fans must also extend along enough of the span to capture the specified wing BLI fraction, f_{wing}:

$$\frac{N_{\text{fan}} \, d_{\text{fan}}}{b - d_{\text{fuselage}}} = f_{\text{wing}} = 2 f_{\text{BLI,elec}} \tag{4.13}$$

For full fuselage BLI, the model requires a fan area greater than or equal to the estimated area of the fuselage boundary layer, Δ. The fans are assumed to have a hub-to-tip ratio of 0.3, and $\frac{\Delta}{\Theta^*} = 4.9$.[5] The boundary layer's kinetic energy area, Θ^*, is related to its kinetic energy defect which can be expressed as a function of aerodynamic and BLI parameters described in Appendix A.

$$A_{\text{fan}} = \pi \left(\frac{d_{\text{fan}}}{2} \right)^2 \geq \Delta = \frac{\Delta}{\Theta^*} \left(\frac{D'_p \, f_{\text{surf}} \, f_{\text{BLI,fuselage}}}{\frac{1}{2} \rho V_\infty^2} \right) \tag{4.14}$$

The partial fuselage BLI configurations are based on 40% fuselage BLI via embedded aft fuselage fans, as is the case for the D8. At relevant fan diameters, the boundary layer height is readily captured but the necessary breadth may not be. Optimization without boundary layer constraints mostly led to fan diameters that satisfied the following constraint:

$$N_{\text{fan}} \, d_{\text{fan}} \geq 0.5 \, d_{\text{fuselage}} \tag{4.15}$$

The inequality 4.15 was not applied as a model constraint and was rather referenced as a guideline. Section 5.1 discusses the treatment of a point design which did not meet this guideline. The drag and weight of nacelles of propulsors in an array were reduced by a factor of $\frac{2}{\pi}$ from the individually-podded model described in Appendix A. This applies to wing BLI and embedded fuselage BLI propulsors.

4.1.5 Propulsion System Performance and Sizing

Figure 4.3 shows a generalized propulsion system model, which can parametrically represent the range of conventional, turbo-electric, hybrid-electric, and all-electric configurations of interest. The inputs required are the source and load electrification factors defined in Section 2.1, f_S and f_L, and the number of turboshaft or turbofan cores and motor-powered propulsors. A power balance between the components is used to relate propulsor flow power (Equation (4.11)) to the fuel flow and battery discharge rate required by the mission integration model.

The electrical components are characterized by technology-dependent power-densities and efficiencies, as in Table 3.1. The turboshaft core and ducted fan propulsor performance are similarly characterized in terms of specified thermal and adiabatic efficiency. Their sizing is based on a power-law scaling with mass flow (less than cube-square was found to agree better with available engine data),

$$m_{\text{fan}} = K_{\text{fan}} \dot{m}_{\text{fan}}^{1.2}, \tag{4.16}$$

$$m_{\text{core}} = K_{\text{core}} \dot{m}_{\text{core}}^{1.2}. \tag{4.17}$$

$$\tag{4.18}$$

---

[4]Estimate based on flat plate turbulent boundary layer.

[5]From cubic spline boundary layer profile with wall slip velocity such that $H^* = 1.75$, a representative value for turbulent attached flow [2].
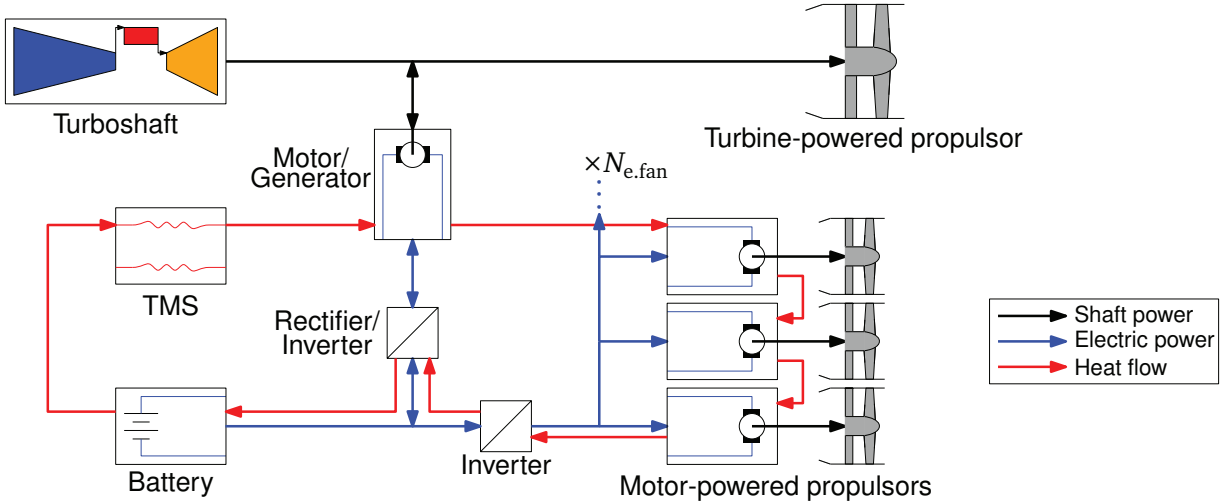
Figure 4.3: Electrified propulsion system.

The core mass flow is calculated from the core specific power, P_{sp},

$$m_{core} = \frac{P_{core}}{P_{sp}}. \tag{4.19}$$

Details of the propulsion system power balance and specified scaling parameters are provided in Appendix A.

4.2 Geometric Programming

The present aircraft configuration design model is formulated as a *signomial program* (SP), which can be solved using existing geometric programming methods. A *geometric program* (GP) is a non-linear optimization problem of the form,

$$
\begin{aligned}
\text{minimize} \quad & g_0(x), \\
\text{subject to} \quad & f_i(x) = 1, \quad i = 1, \ldots, m, \\
& g_j(x) \leq 1, \quad j = 1, \ldots, n
\end{aligned}
\tag{4.20}
$$

where the objective (g_0) and constraints (f_i and g_j) are formed from *monomials* and *posynomials*:

$$f(x) = c x_1^{a_1} x_2^{a_2} \ldots x_n^{a_n}, \tag{4.21}$$

$$g(x) = \sum_{k=1}^{K} c_k x_1^{a_{1,k}} x_2^{a_{2,k}} \ldots x_n^{a_{n,k}}, \tag{4.22}$$

where $c > 0$ are positive constant parameters and $x > 0$ are positive design variables raised to real constant powers, $a \in \mathbb{R}$. In log-space, GPs are *convex* optimization problems, which means they can be solved without an initial guess for the optimal value of the design variables, and with a guarantee of either global optimality or proof of infeasibility, using fast and robust "off-the-shelf" solvers. Further, the sensitivities of the objective function, g_0, to the constant design parameters, c, are calculated as part of the solution, providing insight into the impact of design requirements, constraints, and assumptions on performance.

If the constant coefficients, c, in Equation (4.22) are allowed to be negative, $g(x)$ becomes a *signomial*, and the resulting SP can be solved via sequential solutions of GP approximations. Even more permissive signomial equality constraints can be treated using trust region methods. The benefit of allowing SPs is that it enables modeling of a broader range of functions encountered in engineering design; any analytic function can effectively be modeled by a signomial Taylor series approximation. The drawback of SPs is that the guarantee of global optimality is lost, and appropriate initial guesses for variables in the signomial constraints are sometimes necessary to converge on a solution. Most functional relationships encountered in engineering design can be cast as GP or SP constraints, i.e., as relationships between products of design variables raised to constant powers. In many cases, depending on the objective function, the impact of signomial equalities can be adequately modeled as GP inequality constraints that are always active; when this is not possible, addition of a small number of well-formed signomial constraints can still yield a robust SP model.

The model described here is implemented in GPkit [16], an open source Python package for creating, manipulating, and solving GP and SP models. GPkit leverages Python's object-oriented framework to enable modular development of multi-disciplinary models from constituent component models with varying levels of fidelity. Another practical benefit in formulating the configuration model as an optimization problem is that the existing solution algorithms provide an iteration procedure for solving the entire system of equations. In other words, the optimization framework eliminates the need for "inputs" and "outputs" for each of the subsystem modules, allowing simultaneous solution of the system of non-linear constraints.

4.3 Baseline Missions

To span the space of aircraft sizes and missions, four baseline missions were defined for initial assessment with different electrified architectures. Table 4.1 lists the specified design payload, range, cruise speed, and altitude, and Figure 4.4 shows the nominal sizing and configurations. Additional details of mission-specific design parameters, e.g., fuselage dimensions and wing loading, are provided in Appendix A. The results in Section 5 consider optimized electrified propulsion architectures for each of the baseline missions with different technology assumptions and the sensitivity of performance to variations in both payload and range.

4.4 Trade Space Exploration

4.4.1 Propulsion System Configurations

In addition to aircraft mission and technology level, attributes of the propulsion system must be specified in order to define an aircraft design and evaluate its performance (i.e. its PSEC). Many attributes are treated as optimizable parameters within the GP framework (e.g., gas generator size, electric component size, battery capacity, propulsor size, electric propulsor count, and BLI fraction). However, some aircraft

Table 4.1: Baseline missions

Mission	Payload (passengers)	Range (nmi)	Cruise Speed	Cruise Altitude (ft)
Thin Haul	20	500	150 knots	20,000
Regional	80	1,500	Mach 0.785	35,000
Medium Haul	180	3,000	Mach 0.785	35,000
Long Haul	350	6,000	Mach 0.840	35,000

Figure 4.4: Notional vehicle sizing for baseline missions with conventional propulsion.

attributes are discrete and must be specified a priori (e.g., propulsion system architecture, gas generator count, propulsor integration, and BLI and battery presence).

This motivates the concept of a configuration, which constitutes the minimum set of decisions needed to assess aircraft performance. A configuration (i) consolidates the discrete attributes of a propulsion system and (ii) samples a subset of the trade space by converging to the best-performing point within the range of optimizable attributes. Trade space exploration consists of selecting configurations, evaluating their performance, and compiling the best-performing outputs. Figure 4.5 shows sample configuration sketches that illustrate the discrete attributes of two configurations.

4.4.2 Exploration Rationale

To summarize the considered trade space, a conceptual two-dimensional test matrix is developed. One dimension of the matrix describes the baseline missions (thin haul, regional, etc.) and the other gives architecture classifications (conventional, turbo-electric, and all-electric). Any given "cell" in the ma-

Figure 4.5: Sample configuration sketches and component legend for (a) B737-like conventional aircraft with under wing turbofans, (b) STARC-ABL-like turbo-electric aircraft with under wing turbofans and generators powering a BLI tail cone thruster.

trix may represent many configurations. The intent is to populate the cells with point designs that correspond to best-performing configurations.

Since electrification allows for more varied configurations, the architecture classifications capture parts of the trade space of different sizes. The conventional baseline classification represents the continuation of contemporary aircraft design and contains only one configuration. The advanced conventional case allows for novel non-electric configurations with the assumption that non-electric configurations preclude substantial propulsion distribution. This space includes more than one configuration, but the D8 conceptual design was identified as a representative configuration. This decision was also based on a performance comparison between partial fuselage BLI and tail cone fuselage BLI.

The electrified architecture classifications reflect the wider trade space: wing and fuselage BLI are possible, electric fan size and count may vary, batteries may be included, turbo-electrics may have turbofans (partial turbo-electric) or turbogenerators (full turbo-electric), and so on. Figure 4.6 presents a set of configurations assembled from combinations of architectures and attributes; these configurations will be considered in determining the best performing configuration.

These configurations are not exhaustive and there are assumptions and constraints that stem from limitations in the current model's implementation. Specifically:

- Only tube-and-wing airframes are considered.
- All mechanical fans in a design are the same size.
- All electrical fans in a design are the same size.
- Only ducted fans are considered.
- Distributing propulsion on the wing implies wing BLI via a ducted array of fans at the trailing edge. Propulsors fully embedded in the wing without BLI are not considered.
- Fuselage BLI is achieved via a tail cone thruster (full), or two embedded fans (partial).
- Fuel-burning configurations have two cores.

(a) Turbo-electrics *

(i)   (ii)   (iii)

Full turbo-electric

(iv)   (v)   (vi)

Partial turbo-electric

(vii)   (viii)

*all turbo-electrics may also utilize
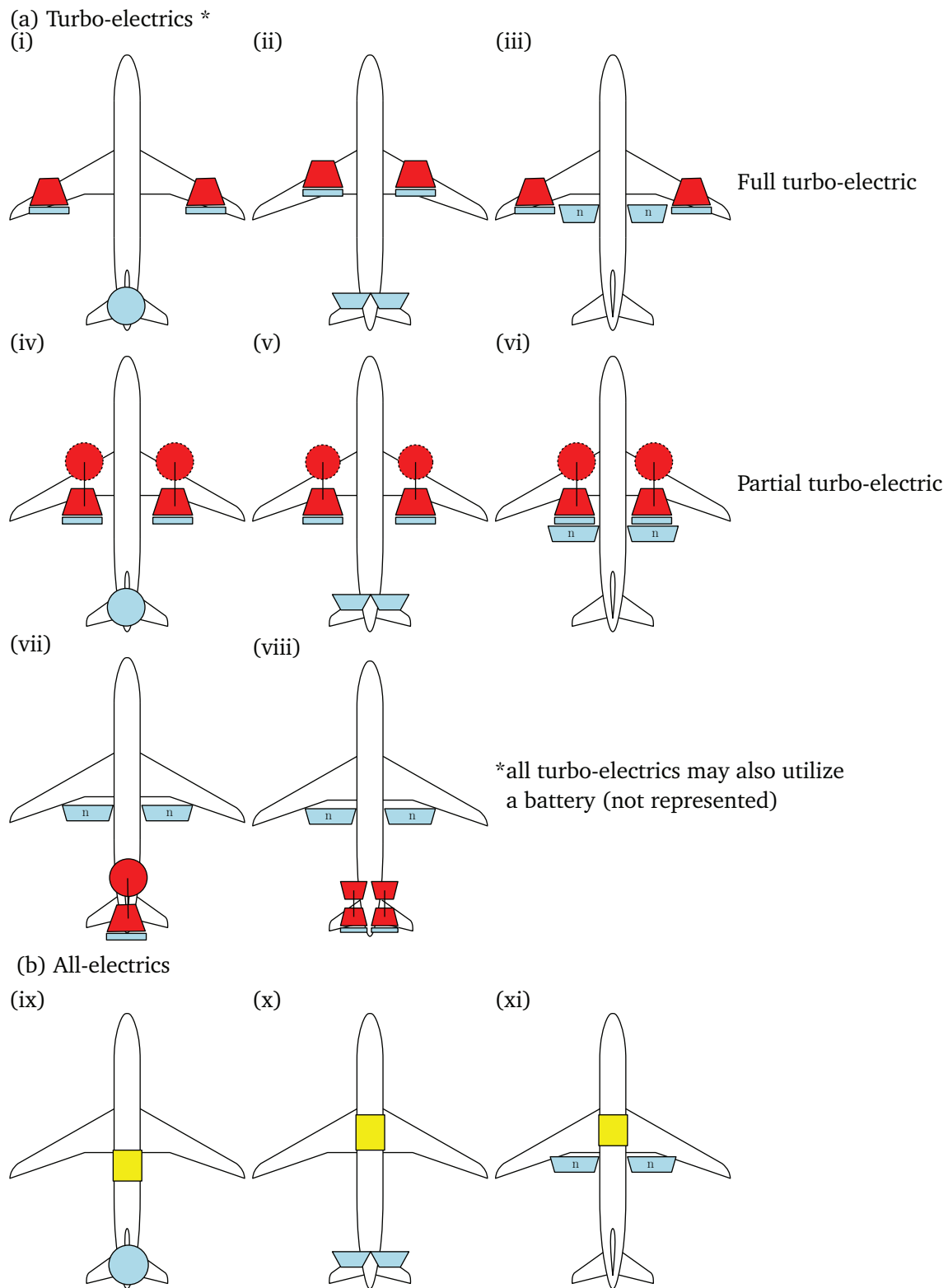 a battery (not represented)

(b) All-electrics

(ix)   (x)   (xi)

Figure 4.6: Electrified configurations considered in trade space assessment (see legend in Figure 4.5).

5 Trade Space Analysis

5.1 Propulsion Configuration Studies

5.1.1 Configuration Selection

The analysis described above combined the configurations that were identified with the baseline missions, and identified the best performers in terms of PSEC. For turbo-electrics, configuration (iii) performed best for the thin-haul mission and configuration (viii) did so for all other missions. Within the all-electrics, configuration (xi) performed best for all missions. Table 5.1 describes the architecture classifications and the best-performing configuration within each one.

In the case of a configuration (viii) aircraft flying a thin-haul mission, the mechanical fan diameters optimized to zero. This violated inequality 4.15. Since fuselage BLI was treated as a discrete choice, the trade in fan size and BLI benefit was not captured. To exclude the non-physical result of BLI with zero-diameter fans, full turbo-electric designs were selected as the best-performing over partial turbo-electric for thin-haul missions.

5.1.2 Performance with Optimistic 2035 Technology Level

Figure 5.1 presents the minimum PSEC attained by optimized designs for each mission and architecture. The percentage reductions in PSEC relative to the conventional baseline are noted above the bars for other architectures.

Comparing the minimum-PSEC design from the selected configurations between architectures shows

Table 5.1: Summary of architecture classifications (columns of test matrix)

| Architecture classification	Description	Best-performing configuration
Conventional (Baseline)	Turbofans only	Two podded turbofans
Advanced Conventional	BLI turbofans, no distribution	Two embedded turbofans, 40% fuselage BLI.
Turbo-electric	Turbofans or turbo-generators powering electrical fans BLI and electrical distribution	Thin-haul: fully turbo-electric with wing BLI Larger classes: Partial turbo-electric with wing BLI Two turbofans with generators, 40% fuselage BLI
All-electric	Battery-powered electrical fans BLI and distribution	Fully turbo-electric with wing BLI
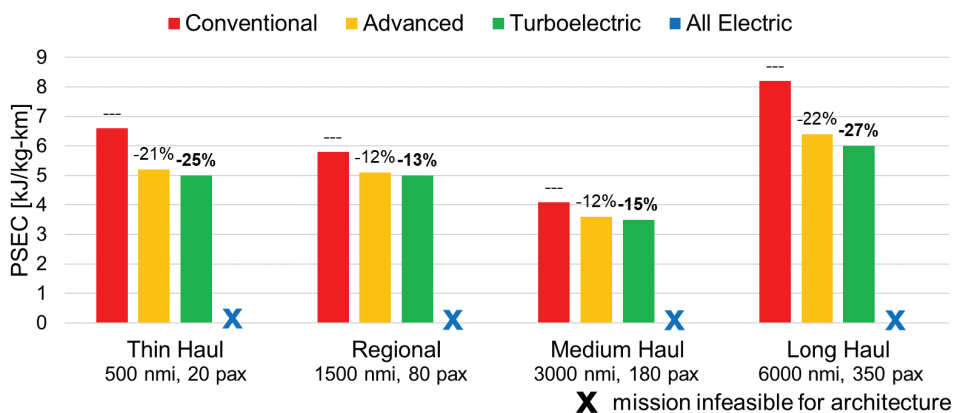
Figure 5.1: Productivity-Specific Energy Consumption (PSEC) versus mission and architecture; design range.

a hierarchy of performance. Advanced conventional (non-electric partial fuselage BLI) and turbo-electric demonstrate a PSEC reduction benefit of approximately equal magnitude, 12-27%. The all-electric designs are not feasible at any scale because the required battery mass is larger than the airframe parameters can support.

Although all-electric is non-competitive for the design missions, reducing the mission range so the all-electric aircraft designs close allows an assessment of the architecture. Figure 5.2 presents the minimum PSEC for each combination of architecture and mission, where each mission is the maximum range at which the all-electric architecture closes.

Electrification on batteries alone decreases PSEC by 15% for a reduced thin haul mission compared to conventional aircraft, but offers no benefit for the other missions. Advanced and turbo-electric aircraft maintain performance improvements, though the benefit decreases with reduced mission length. Both trends are the result of the logarithmic nature of fuel-burning range. Specifically, conventional aircraft get lighter throughout the mission, requiring less power. Battery-powered flight does not share this advantage. All else equal, shorter ranges reduce the benefits of losing mass in flight and increasing overall efficiency, as seen in the decreased performance of advanced and turbo-electric architectures relative to design missions.

As context for the subsequent discussions, it is important to note that, as might be expected, the accuracy of the results depend on the fidelity of the physical models used. Some of the models, for example that used for the aero-structural sizing, are rudimentary and not meant to represent performance predictions of specific vehicle designs over large ranges of parameters. The results should therefore be viewed as a comparison of propulsion architectures *within a given mission class*, where the consistency of the modeling assumptions allows an appropriate comparison. Even with these limitations, however, the electrification trends are consistent across a wide range of missions; this, in turn, suggests the results are broadly applicable. Further, the framework can be extended to include higher-fidelity models, as described in Section 6.2, to allow more accurate assessment of specific configurations if desired.

5.1.3 Performance with Conservative 2035 Technology Level

Reducing the technology level parameters to conservative 2035 values markedly reduces the space of beneficial electric designs. All electrics remain infeasible. Turbo-electric architecture still reduces the baseline PSEC but offers no benefit over advanced conventional due to the greater mass penalty from motors and power electronics. Partial turbo-electric designs optimize to $f_L = 0$ (i.e. the advanced conventional architecture). The benefit of the full turbo-electric thin-haul design decreases to 19% from
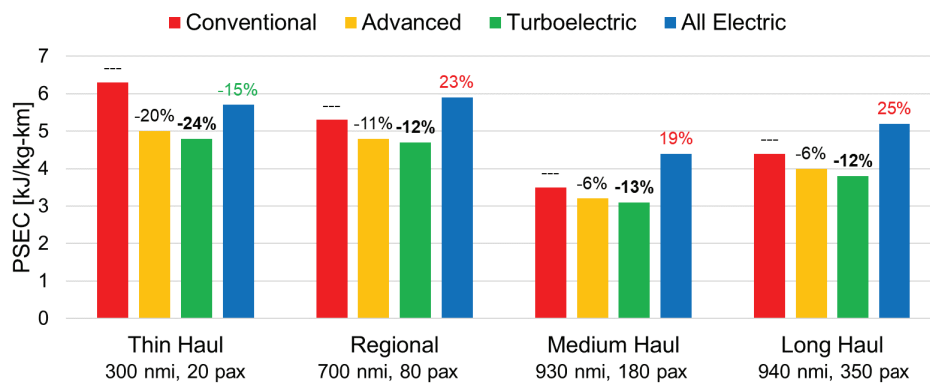

Figure 5.2: Productivity-Specific Energy Consumption (PSEC) versus mission and architecture; range reduced to make all-electric architecture feasible.

24%, offering 2% less energy benefit than the corresponding advanced conventional design. Advanced and baseline conventional aircraft are unaffected by the decreased electric technology level.

5.1.4 Minimum Battery Technology Level

Increasing the battery technology level allows the all-electric designs to close at increased range. Figure 5.3 lists the minimum BSE for an all-electric to close for design missions. At a minimum, the required BSEs are 60% greater than the optimistic 2035 value; batteries alone are unlikely to power aircraft at current design missions.

5.1.5 Features of Efficient Electrified Aircraft

The best-performing electrified aircraft have highly-distributed propulsion and BLI, as reflected in propulsor arrays with many (>250) small (<12 inch) fans. Table 5.2 summarizes the main propulsion system parameters for these best-performers, indicating the high degree of distribution. Partial turbo-electric designs minimize PSEC for regional missions and longer, while full turbo-electrics do so for thin haul missions. The PSEC benefit stems from two synergistic effects of distribution: (i) the mass scaling, which favors smaller propulsors, and (ii) the aero-propulsive performance improvement from BLI. The configurations with distributed propulsion are also aided by the reduction in nacelle mass and drag from propulsor arrays.

The reported optimized designs bound the benefits found in the study. However, practical considerations may preclude full wing BLI and hundreds of fans. Limiting the fan count results in smaller PSEC reductions, as in Figure 5.4, which compares a 24-fan thin-haul turbo-electric design with the conventional baseline. For a turbo-electric thin-haul aircraft, the PSEC reduction shrinks from 25% to 13%. This is an improvement over the conventional baseline, but it is less than the conventional advanced configuration, which reduced PSEC by 21%.

5.1.6 Trends and Main Trade of Distributed Propulsion

The propulsor scaling laws imply that decreases in size result in less weight per unit mass flow. The highly-distributed systems, however, have heavier, electrified propulsion components. Figure 5.5 illustrates the system level performance trends as an advanced conventional concept is electrified with the addition of wing BLI. The quantities shown are overall performance (PSEC), aero-propulsive performance (propulsive efficiency and effective lift-to-drag ratio), and propulsion system mass all as functions of the fraction of electrical distribution on the wing.
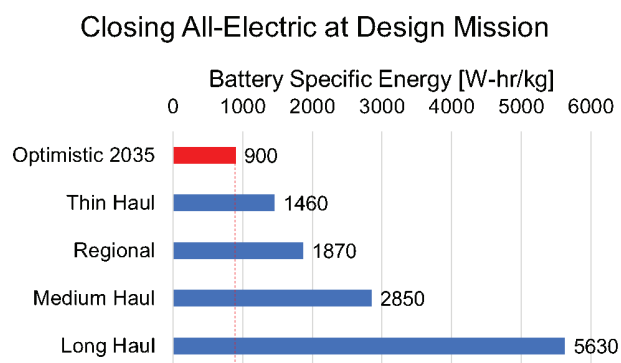
Figure 5.3: Minimum BSE required to close all-electric architecture at design missions.

Table 5.2: Propulsion system parameters for minimum PSEC point designs

Mission	f_S	f_L	Mechanical Fans			Electrical Fans		
			N	d_{fan} (in)	$f_{\text{BLI,m}}$	N	d_{fan} (in)	$f_{\text{BLI,e}}$
Thin-haul (20 pax, 500 nmi)	0	1	2	—	0	254	4.5	0.5
Regional (80 pax, 1500 nmi)	0	0.55	2	31	0.2	248	3.8	0.5
Medium-haul (180 pax, 3000 nmi)	0	0.48	2	45	0.2	308	4.1	0.5
Long-haul (350 pax, 6000 nmi)	0	0.43	2	86	0.2	296	7.3	0.5

Turbo-Electric Thin-Haul Transport Concept

PSEC	= 5.77 kJ/kg-km (**-13%**)
Gross takeoff weight	= 4530 kg
Payload	= 1950 kg
Range	= 500 nmi
Cruise speed	= 150 kt
Number of fans	= 24
Fan diameter	= 10.0 in
Motor power	= 1.80 kW
Propulsion system mass	= 421 kg
Fuel mass	= 242 kg

Conventional Baseline

PSEC	= 6.59 kJ/kg-km
Gross takeoff weight	= 4490 kg
Payload	= 1950 kg
Range	= 500 nmi
Cruise speed	= 150 kt
Number of engines	= 2
Fan diameter	= 30.9 in
Core power	= 256 kW
Propulsion system mass	= 363 kg
Fuel mass	= 277 kg

Figure 5.4: Moderately-distributed fully turbo-electric concept for thin haul mission compared to conventional baseline; fan count specified prior to optimization.

The propulsion system mass increases as electrical equipment is added due to the growing electric components. There is a shrinking propulsor mass, which decreases by 44% from full distribution, $f_{wing} = 0$ to 1. The distribution-enabled BLI improves the propulsive efficiency, η_p, by 2 percentage points and the effective lift-to-drag ratio, $C_L/C_{\Phi,AC}$ by 30%. The aero-propulsive effects have a larger effect than the added mass, netting a benefit in fuel burn.

This trade of weight and efficiency is sensitive to the considered parameter space. As discussed in Section 5.1.4, lower electric technology level decreases the PSEC benefit such that the turbo-electric configuration underperforms relative to the advanced conventional architecture. There are analogous engineering constraints that can limit the benefit of distributed BLI. For example, imposing a minimum fan size may reduce and even negate the aero-propulsive BLI benefits. Figure 5.6 demonstrates how a
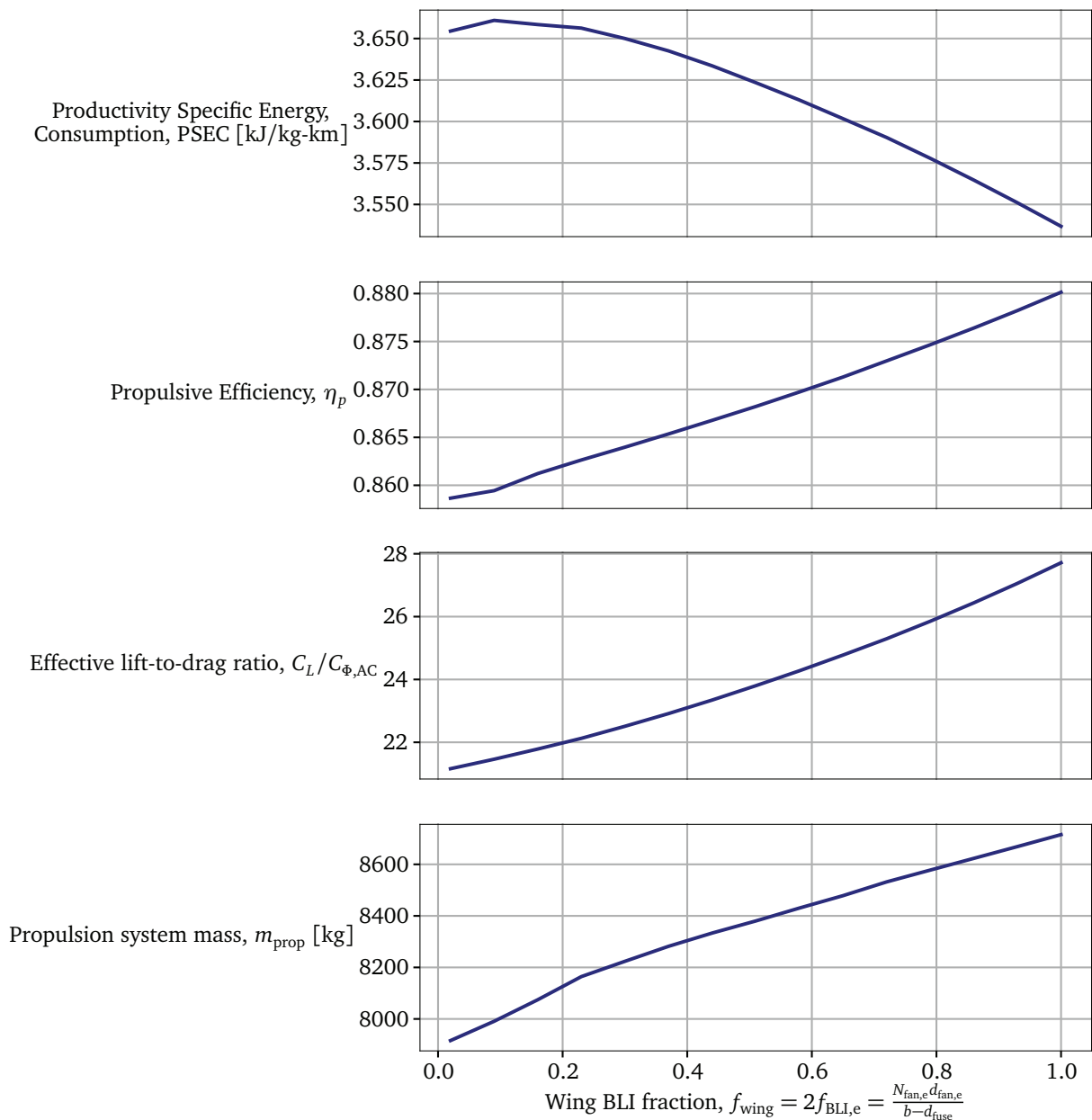
Figure 5.5: Medium haul advanced conventional aircraft is electrified via wing BLI propulsors (partial turbo-electric); system parameters as a function of electric distribution.

minimum fan size constraint reverses the trend of fuel burn benefit with greater BLI. The figure shows, as the wing BLI fraction increases, fans shrink until they reach the specified minimum size (6 inches). For $f_{\text{wing}} \geq 0.52$, the marginal benefit of distributing decreases, resulting in a shallower fan count slope. The marginal benefit becomes negative at $f_{\text{wing}} = 0.7$ and PSEC increases with further distribution. This behavior highlights boundary layer height considerations for BLI since these constraints often drive electric fan size (Section 4.1.4).
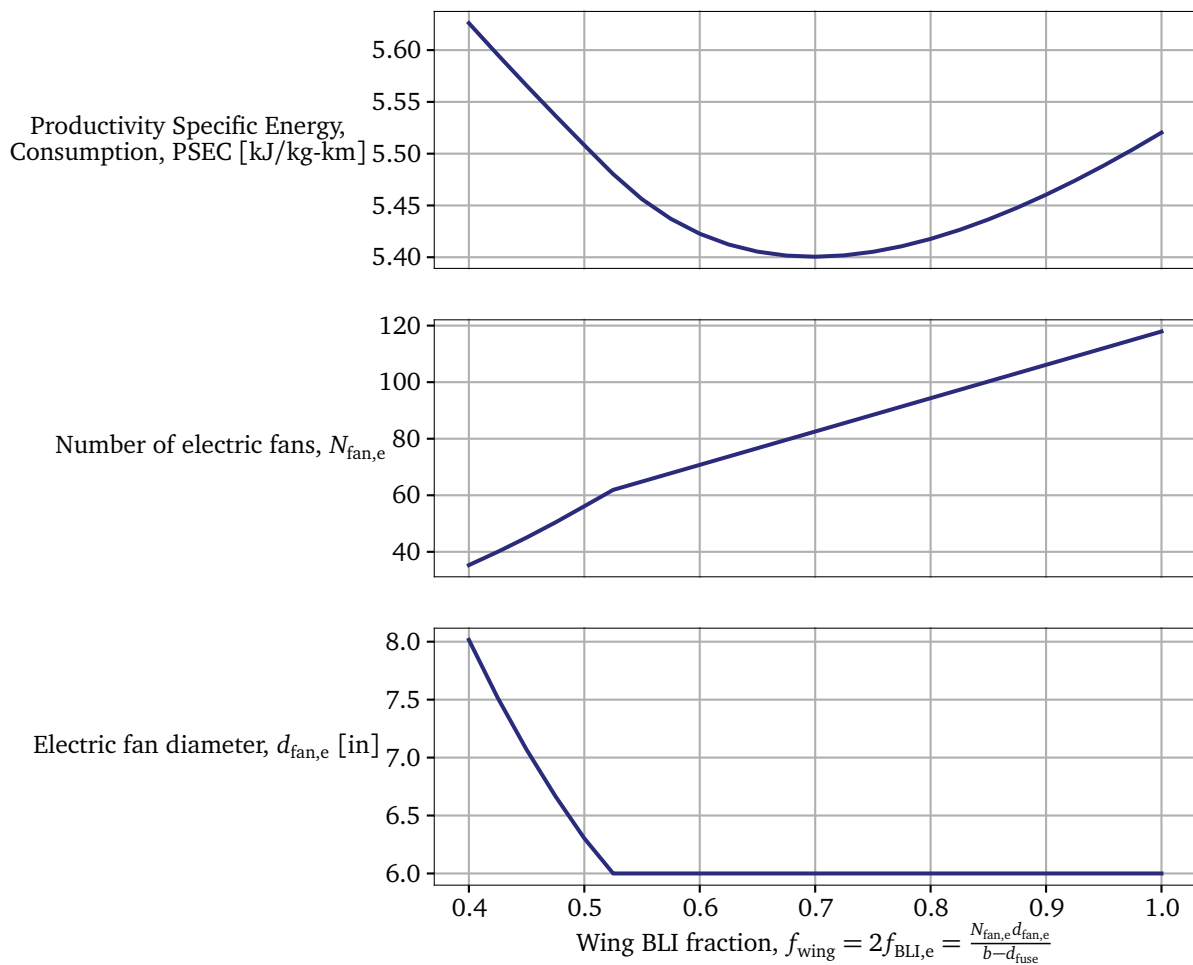
Figure 5.6: Performance and fan parameters of full turbo-electric, thin-haul design as a function of distribution, with minimum fan size constraint ($d_{\mathrm{fan},e} \geq 6$ in.).

5.1.7 Propulsion Configurations Summary

Turbo-electric architectures offer the lowest PSEC across all design missions via fully turbo-electric configuration (iii) for thin haul missions and partial turbo-electric configuration (viii) for all other missions. The advanced conventional architecture decreases PSEC by similar amounts. An all-electric architecture cannot fly any of the design missions due to the battery weight. Reduced mission length allow the all-electric designs to close, but only offer PSEC reduction benefit for the thin-haul mission. Since the all-electric architecture is non-competitive with turbo-electric or advanced conventional architectures outside of highly-reduced ranges, Section 5.2 discusses battery-powered flight in this corner of the trade space.

5.2 Mission Studies

An objective of the current work was to determine the relation between mission (defined here as a combination of payload and range) and electrified aircraft performance. Two important questions to be answered were: (i) for what missions are electrified aircraft feasible, and (ii) for what missions might electrified aircraft provide a reduction in PSEC relative to an equivalent conventional aircraft?

In this section the results of a mission-related trade space analysis is presented. It should be noted

that the aircraft considered take advantage of highly distributed architectures which facilitate high levels of boundary layer ingestion (BLI). The number of fans and fraction BLI used in this section is believed to be in line with determining the best possible performance that can be achieved by electrified aircraft, although these numbers of fans are not necessarily desirable from a practical standpoint.

5.2.1   Thin-Haul: All-electric

Figure 5.7 shows PSEC and takeoff mass data for an all-electric thin-haul aircraft as a function of range, for the optimistic 2035 technology assumptions described in Section 3.

For this case, the range of the aircraft had to be reduced to 300 nmi for the design to be feasible. Over the ranges shown in Fig. 5.7 there is a reduction in PSEC for all the levels of BLI. The maximum reduction in PSEC is achieved at a range of about 100 nmi, although this is a flat minimum and a reduction on the order of 50% is predicted for ranges between 50 and 200 nmi with 50% BLI and only slightly less with no BLI. For this aircraft class, increasing BLI also increases the feasible range of the aircraft; the maximum feasible range goes from 240 nmi (no BLI) to 300 nmi (50% BLI).

Figure 5.7 also shows that the aircraft weight increases rapidly with range due to the battery weight becoming a larger fraction of the total weight. As an example, at the range of maximum PSEC reduction (100 nmi) the all-electric aircraft is 10% heavier than the conventional aircraft sized for the same range and at the maximum feasible range (300 nmi) it is 45% heavier. This increase is slightly diminished with BLI.

For the conservative 2035 technology assumptions, this aircraft is only feasible up to 60 nmi with 50% BLI, and is thus not shown.

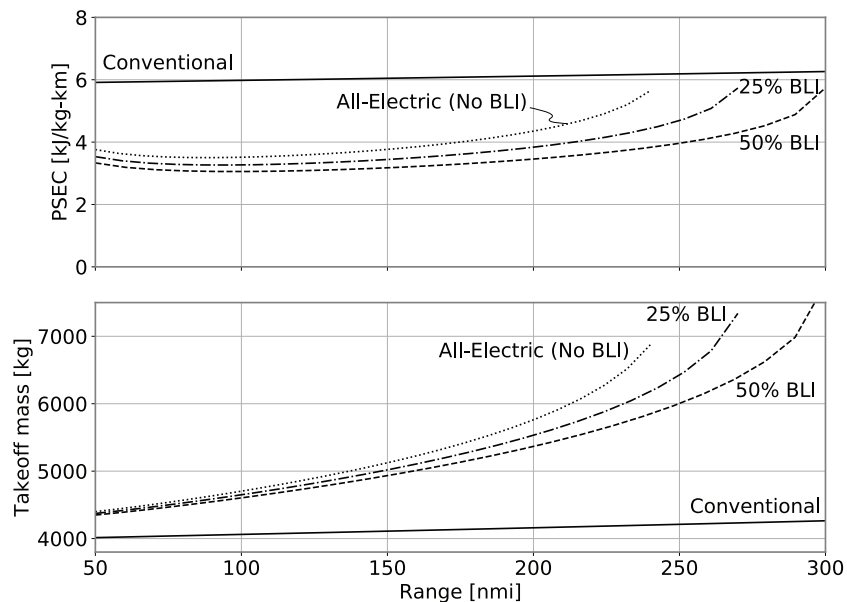Figure 5.7: PSEC and takeoff mass versus range for all-electric thin-haul aircraft; $BSE = 900$ W·h/kg, $[P/m]_{\text{mot}} = 16$ kW/kg, $[P/m]_{\text{conv}} = 19$ kW/kg, $f_S = 1$, $f_L = 1$; $N_{\text{fan}_E} = 146$, $d_{\text{fan}_E} = 0.12$ m.

5.2.2   Thin-Haul: Turbo-electric

Figure 5.8 shows PSEC and takeoff mass as a function of range for a fully turbo-electric thin-haul aircraft for the optimistic 2035 technology assumptions.

It was shown in Section 4.4.2 that the fully turbo-electric architecture ($f_L = 1$) gives the lowest PSEC for the thin-haul and was thus used for the current analysis. Figure 5.8 shows that over the entire range considered this architecture results in a reduction in PSEC of about 25% when 50% BLI is employed and about half of that with no BLI. The turbo-electric architecture also slightly reduces the takeoff mass compared to the conventional, even without the benefit of BLI.

With the conservative 2035 technology assumptions, a reduction in PSEC is only obtained if BLI is used and there is no change in takeoff mass.

5.2.3   Thin-Haul: Hybrid-electric

For the results in this section, the source electrification factor f_S was optimized for minimum PSEC. The load electrification was fixed at $f_L = 1$, meaning that all flow power is provided by electrically powered fans.

The result of sweeping over range while optimizing f_S is shown in Figure 5.9. When $0 < f_S < 1$ the configuration is a hybrid-electric and the energy required to produce propulsive power comes from both fuel and batteries. Such a design could be instantiated by using a fuel-powered turbo-generator to supply some electric power to the propulsive fans, with the remaining fraction supplied by a battery.

Figure 5.9 shows a summary of thin-haul aircraft behavior. For low ranges, all-electric architecture ($f_S = 1$) results in the lowest PSEC, but for the higher ranges the all-electric is no feasible, and turbo-electric architecture ($f_S = 0$) has better PSEC performance. Over a small intermediate range, hybrid-electric architecture with an energy split between fuel and batteries is optimal. The effect of BLI is to improve the all-electric and hybrid-electric performance, shifting the transition region to the right.
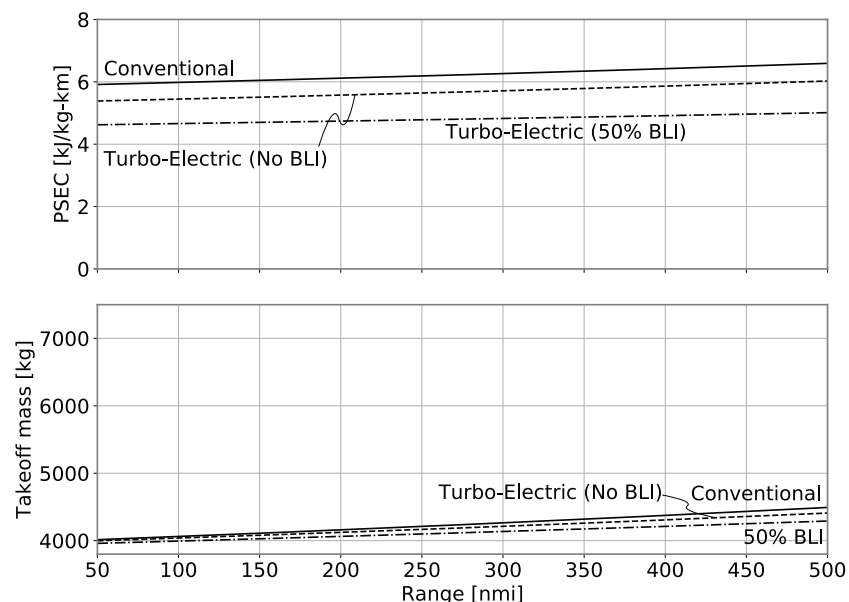
Figure 5.8: PSEC and takeoff mass versus range for turbo-electric thin-haul aircraft; $[P/m]_{\text{mot}} = 16\,\text{kW/kg}$, $[P/m]_{\text{conv}} = 19\,\text{kW/kg}$, $f_S = 0$, $f_L = 1$; $N_{\text{fan}_E} = 254$, $d_{\text{fan}_E} = 0.071\,\text{m}$.
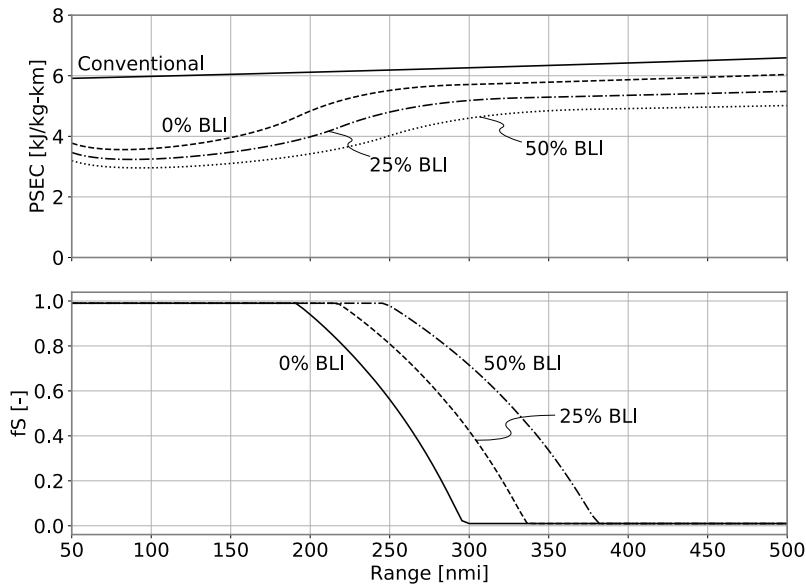
Figure 5.9: PSEC and source electrification factor f_S versus range for thin-haul aircraft; $[P/m]_{mot} = 16\,\text{kW/kg}$, $[P/m]_{conv} = 19\,\text{kW/kg}$, $f_L = 1$; $N_{\text{fan}_E} = 254$, $d_{\text{fan}_E} = 0.071\,\text{m}$.

For the conservative 2035 technology assumptions the all-electric design is infeasible for ranges greater than 60 nmi and a hybrid-electric investigation is therefore not shown for those assumptions.

5.2.4 Thin-Haul: Payload sensitivity

Another mission-related parameter is payload weight. The sensitivity of PSEC to variations in payload weight was assessed for design payload of 14, 17, and 20 passengers. Figure 5.10 shows the results for all-electric and turbo-electric architectures.

For the all-electric, PSEC is insensitive to the number of passengers over most of the range, except at the highest ranges where some benefit is achieved by carrying fewer passengers. This insensitivity to payload can be explained as follows. By reducing the number of passengers the aircraft weight and energy requirement is reduced, but the reduction in payload has a negative effect on PSEC and these two effects nearly balance. At higher ranges where a large fraction of the aircraft weight is battery weight, the reduction in energy required outweighs the reduction in productivity leading to a slight reduction in PSEC.

For the turbo-electric case the PSEC is insensitive to the number of passengers over the entire range considered, with the same trend observed for the conservative 2035 technology assumptions.

5.2.5 All-electric: All classes

The trends observed for the larger aircraft classes are similar to the thin-haul aircraft and will thus not be shown in the same level of detail.

The relative PSEC benefit compared to the baseline conventional aircraft is shown for all-electric aircraft for all classes with the optimistic 2035 assumptions in Fig. 5.11. The all-electric aircraft only provide a substantial PSEC reduction at low ranges. The PSEC benefit for medium- and long-haul aircraft are very nearly equal even though these aircraft differ considerably in size. For ranges higher than those for the minimum PSEC, battery and thus aircraft weight grows so fast that the efficiency benefits of all-electric architectures are negated and the PSEC benefit drops rapidly.
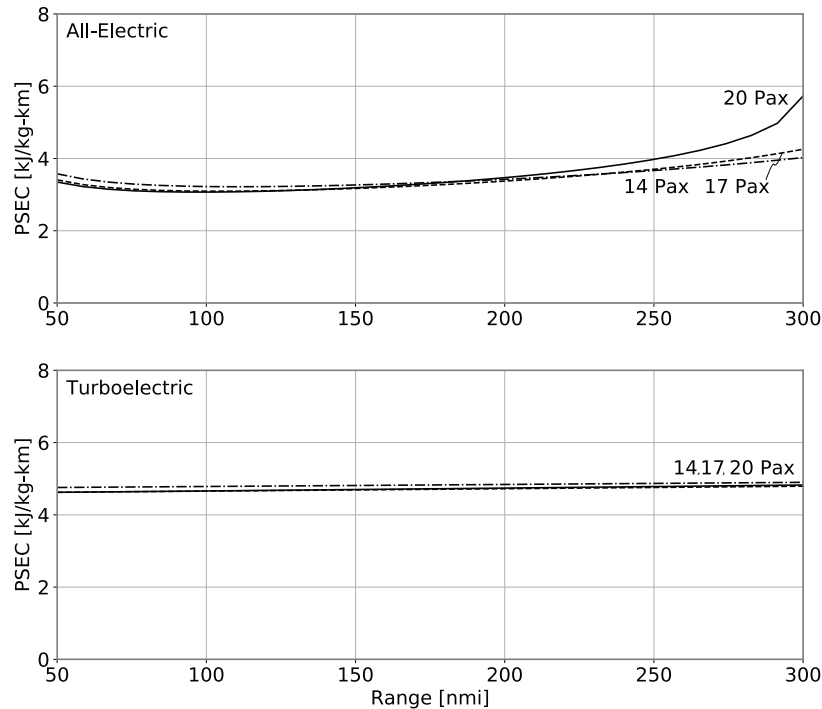
Figure 5.10: PSEC versus range for all-electric and turbo-electric thin-haul aircraft with various payloads; $BSE = 900$ W·h/kg, $[P/m]_{\text{mot}} = 16$ kW/kg, $[P/m]_{\text{conv}} = 19$ kW/kg, $f_{\text{BLI}_E} = 0.5$; all-electric with $N_{\text{fan}_E} = 146$, $d_{\text{fan}_E} = 0.122$ m; turbo-electric with $f_L = 1$, $N_{\text{fan}_E} = 254$, $d_{\text{fan}_E} = 0.071$ m.

For the conservative 2035 technology assumptions, even with 50% BLI, all-electric architecture is only feasible for very low ranges: 60 nmi for thin-haul, 130 nmi for regional and 200 nmi for medium- and long-haul. For these technology assumptions, none of the larger classes lead to a PSEC benefit over the ranges for which they are feasible.

5.2.6 Turbo-electric: All classes

Figure 5.12 shows the PSEC benefit as a function of range for turbo-electric aircraft for all classes with the optimistic 2035 assumptions. The thin-haul is a fully turbo-electric, but the larger classes are partial turbo-electric with approximately 50% of the flow power coming from a conventional turbofan ($f_L \approx$ 0.5), as was found optimal in Section 4.4.2. A PSEC benefit of up to 25% is found for the thin-haul, 13% for the regional class, 15% for the medium-haul and 27% for the long-haul aircraft. All architectures provide a PSEC benefit over the ranges considered and the PSEC benefit increases with aircraft design range.

For the conservative 2035 technology assumptions, the PSEC benefit is reduced approximately 2%, shifting all the curves in Fig. 5.12 downwards.

5.2.7 Hybrid-electric: All classes

Figure 5.13 shows the optimal load electrification factor, f_S, and the PSEC reduction, relative to a conventional aircraft sized for the same mission, as a function of range for all classes considered. For all
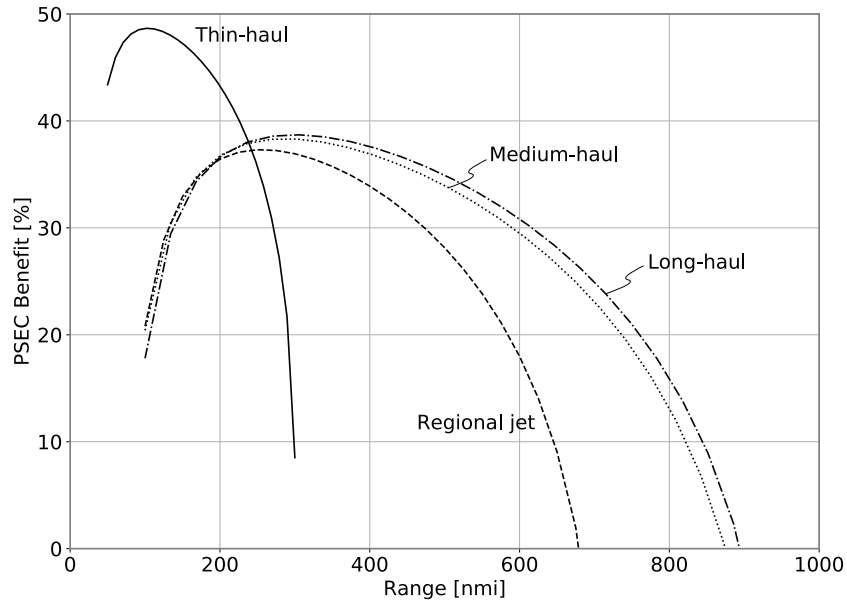
Figure 5.11: Relative PSEC benefit for all-electric aircraft for all classes; $BSE = 900\,\mathrm{W{\cdot}h/kg}$, $[P/m]_{\mathrm{mot}} = 16\,\mathrm{kW/kg}$, $[P/m]_{\mathrm{conv}} = 19\,\mathrm{kW/kg}$, $f_{\mathrm{BLI}_E} = 0.5$; $f_S = 1$, $f_L = 1$; thin-haul with $f_{\mathrm{BLI}_M} = 0$; $N_{\mathrm{fan}_E} = 146$, $d_{\mathrm{fan}_E} = 0.122\,\mathrm{m}$; regional with $f_{\mathrm{BLI}_M} = 0.2$; $N_{\mathrm{fan}_E} = 98$, $d_{\mathrm{fan}_E} = 0.246\,\mathrm{m}$; medium-haul with $f_{\mathrm{BLI}_M} = 0.2$; $N_{\mathrm{fan}_E} = 94$, $d_{\mathrm{fan}_E} = 0.343\,\mathrm{m}$; long-haul with $f_{\mathrm{BLI}_M} = 0.2$; $N_{\mathrm{fan}_E} = 118$, $d_{\mathrm{fan}_E} = 0.464\,\mathrm{m}$.

classes the load electrification factor is set to $f_L = 1$, meaning all flow power is provided by electrically powered fans.

The transition from all-electric to turbo-electric occurs in the same manner, but at higher ranges, for the larger classes as for the thin-haul. Reducing f_S from unity has the benefit of extending the feasible range of aircraft to higher ranges than all-electric architecture can achieve.

As f_S transitions from one to zero the PSEC benefit reduces and levels off at about 8% for the larger classes and 22% for thin-haul. This effect occurs because PSEC is much less sensitive to range for turbo-electrics than for all-electrics.

Parallel hybrid-electric architectures were found to provide a PSEC reduction similar to series hybrid architectures for a given mission.

All-electrics are only feasible for ranges less than 60 nmi with the conservative 2035 technology assumptions, and they were therefore not considered for the hybrid-electric study.

5.2.8 Mission Trade-Space Analysis Summary

All-electric aircraft are only feasible for ranges shorter than those for existing commercial aircraft. The maximum feasible range with optimistic 2035 battery and electrical machine technology assumptions are 300 nmi for thin-haul, 700 nmi for regional jet, 930 nmi for medium-haul and 940 nmi for long-haul aircraft. With the conservative 2035 technology assumptions, the feasible ranges are reduced even further to 60 nmi for thin-haul, 130 nmi for regional, and 200 nmi for medium- and long-haul.

For turbo-electric configurations, there are reductions in PSEC relative to conventional for all classes and ranges considered, both with optimistic 2035 and conservative 2035 technology assumptions. The magnitude of the benefit is much less sensitive to range than that of all-electric architectures. Additionally, the benefit increases with range for all classes with partial turbo-electric architectures. This
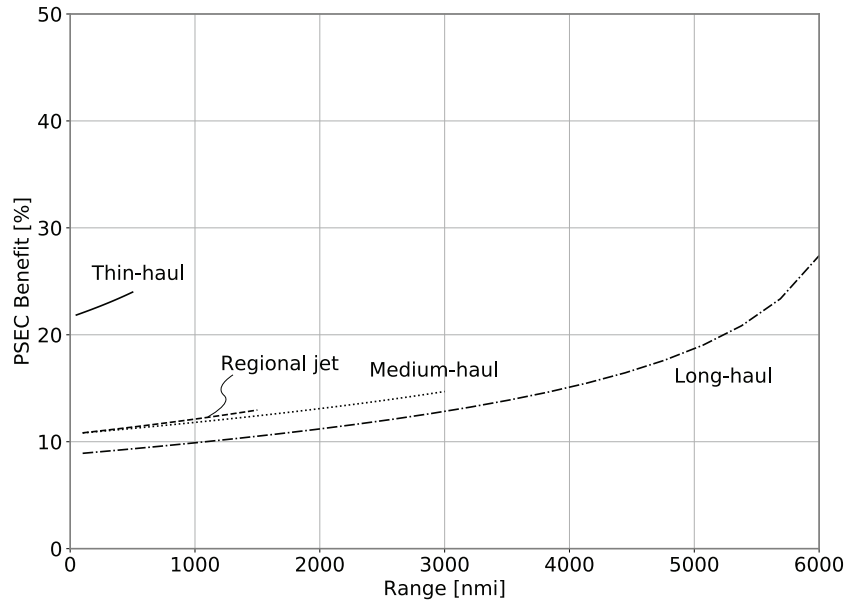
Figure 5.12: Relative PSEC benefit for turbo-electric aircraft for all classes; $[P/m]_{\text{mot}} = 16\,\text{kW/kg}$, $[P/m]_{\text{conv}} = 19\,\text{kW/kg}$, $f_{\text{BLI}_E} = 0.5$; thin-haul with $f_L = 1$, $f_{\text{BLI}_M} = 0$; $N_{\text{fan}_E} = 254$, $d_{\text{fan}_E} = 0.071\,\text{m}$; regional with $f_L = 0.55$, $f_{\text{BLI}_M} = 0.2$; $N_{\text{fan}_E} = 248$, $d_{\text{fan}_E} = 0.097\,\text{m}$; medium-haul with $f_L = 0.48$, $f_{\text{BLI}_M} = 0.2$; $N_{\text{fan}_E} = 308$, $d_{\text{fan}_E} = 0.104\,\text{m}$; long-haul with $f_L = 0.43$, $f_{\text{BLI}_M} = 0.2$; $N_{\text{fan}_E} = 298$, $d_{\text{fan}_E} = 0.185\,\text{m}$.

insensitivity to range might have advantages if off-design and fleet-wide considerations are taken into account, since different aircraft in a fleet will likely fly different ranges. Turbo-electric architectures appear to be the best choice for electrified propulsion for missions similar to those of conventional commercial aircraft.

The range-extending property of a turbo-generator added to an all-electric configuration, i.e., a hybrid-electric architecture, allows the efficiencies of aircraft with high source-electrification to be achieved at larger ranges than an all-electric architecture. Hybrid architecture provides no benefit at larger ranges because the efficiency benefits of the battery trades against the low energy density of batteries (relative to hydrocarbon fuel), and turbo-electric architectures are optimal for ranges not much larger than the maximum feasible all-electric range. There is thus a narrow intermediate band of short ranges at which hybrid-electric provides a PSEC benefit. Both series and parallel architectures provide approximately the same benefits compared to conventional propulsion.

5.3 Electric Component Technology Studies

In this section, we examine the effect of technology level on the feasibility and performance of electrified aircraft, to quantify the benefits as technology improves. All-electric aircraft have been shown to be feasible only at reduced ranges for all sizes; to illustrate the effects of electrified propulsion for all architectures, we assess the performance of a reduced-range thin-haul aircraft as a function of technology parameters.

The baseline conventional aircraft, which carries 20 passengers over a range of 100 nmi, is assumed to be powered by two mechanically driven fans without BLI ($f_S = 0$, $f_L = 0$, and $f_{\text{BLI}_M} = 0$). The all-electric aircraft ($f_S = 1$ and $f_L = 1$) flies the same mission. It is assumed that electrification enables distributed propulsion (DP) and boundary layer ingestion (BLI). Battery effects (BSE and BSP) and
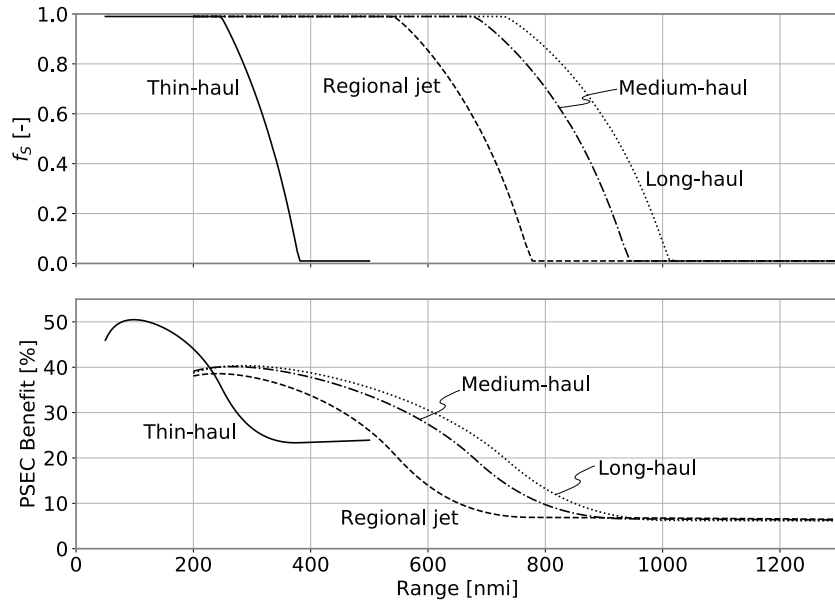
Figure 5.13: Relative PSEC benefit for hybrid-electric aircraft for all classes; $[P/m]_\mathrm{mot} = 16\,\mathrm{kW/kg}$, $[P/m]_\mathrm{conv} = 19\,\mathrm{kW/kg}$, $f_{\mathrm{BLI}_E} = 0.5$; $f_L = 1$; thin-haul with $f_{\mathrm{BLI}_M} = 0$; $N_{\mathrm{fan}_E} = 254$, $d_{\mathrm{fan}_E} = 0.071\,\mathrm{m}$; regional with $f_{\mathrm{BLI}_M} = 0.2$; $N_{\mathrm{fan}_E} = 248$, $d_{\mathrm{fan}_E} = 0.097\,\mathrm{m}$; medium-haul with $f_{\mathrm{BLI}_M} = 0.2$; $N_{\mathrm{fan}_E} = 308$, $d_{\mathrm{fan}_E} = 0.104\,\mathrm{m}$; long-haul with $f_{\mathrm{BLI}_M} = 0.2$; $N_{\mathrm{fan}_E} = 298$, $d_{\mathrm{fan}_E} = 0.185\,\mathrm{m}$.

other component effects (specific powers of motors and converters) are considered separately. When one set of parameters is varied, the other technology parameters are set at the optimistic 2035 values from Section 3.4.

5.3.1   Effects of Battery Technology

For a reduced-range 100 nmi mission, the all-electric aircraft is not feasible at current and conservative 2035 battery technology. Figure 5.14 shows the effect of increasing BSE (and with it, BSP) on PSEC. The conventional aircraft has a constant PSEC as BSE varies because it carries no batteries. In terms of configuration, the closest all-electric aircraft has two electric fans and no BLI. When the BSE is under 350 W·h/kg, this all-electric aircraft is infeasible. Between 350–400 W·h/kg, the all-electric aircraft becomes feasible, but it requires more energy than the conventional aircraft. As BSE increases further, the battery mass to carry the mission energy decreases, leading to a sharp drop in the PSEC. For the optimistic 2035 battery technology assumptions, the all-electric aircraft consumes about 37% less energy than the conventional aircraft. At higher BSE values, the PSEC curve flattens out, due to the battery mass becoming a smaller fraction of the aircraft takeoff mass, and further increases in BSE provide diminishing benefits in energy consumption.

The all-electric aircraft becomes more beneficial with a greater number of smaller-diameter fans. With distributed propulsion, the all-electric aircraft with more fans becomes feasible at lower BSE values. It also provides a larger PSEC reduction at a given BSE value. For the optimistic 2035 battery technology assumptions, the 20-fan all-electric aircraft provides a PSEC benefit of about 40% over the conventional. As with increasing BSE, however, increasing DP has diminishing returns: going from 20 fans to 100 fans provides less benefits than going from two to 20.

Figure 5.15 shows the range of propulsor configurations available for the all-electric aircraft by
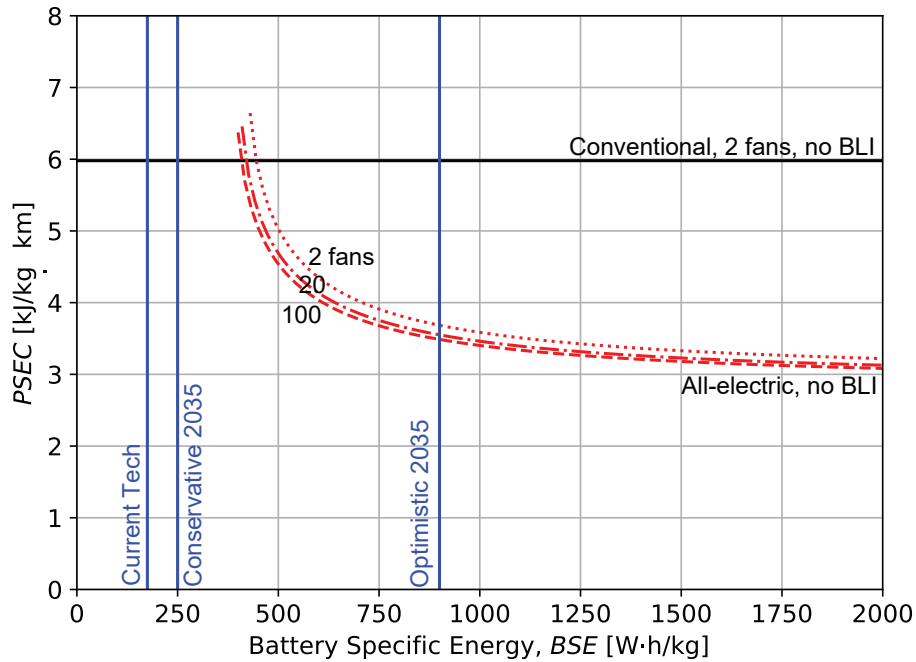
Figure 5.14: Effect of battery technology on $PSEC$ with DP for 100 nmi all-electric thin-haul aircraft; $[P/m]_{\text{mot}} = 16\,\text{kW/kg}$, $[P/m]_{\text{conv}} = 19\,\text{kW/kg}$, $f_S = 1$, $f_L = 1$.

varying the number of fans and BLI. At optimistic 2035 battery technology, the all-electric aircraft with 2 fans and no BLI consumes less energy than the conventional baseline. When the design space is opened up to include massive distribution of fans and BLI, the benefits are twofold: (i) the aircraft becomes feasible at smaller BSE values, and (ii) it offers even greater $PSEC$ reduction at a given BSE value. It can also be seen that all-electric aircraft are feasible at reduced ranges within the predicted BSE numbers. Further, they provide a PSEC benefit over conventional aircraft, and this benefit increases with DP and BLI.

5.3.2 Effects of Component Specific Power

Figure 5.16 shows the effects of increasing component (motors and inverter) specific powers on PSEC. All-electric aircraft are feasible and beneficial over conventional aircraft even with current technology (although BSE and BSP are still set to optimistic 2035 values). Again, the conventional aircraft has a constant PSEC as component specific powers improve, since it does not carry any converters or motors. For the all-electric aircraft, PSEC improves as specific powers increase. Even with 2 electric fans, current technology already provides a benefit of about 25% over conventional. At conservative and optimistic 2035 values, this benefit increases to 28% and 30% respectively.

With DP enabled, the all-electric aircraft provides even greater PSEC benefits, however, with diminishing returns. Going from 2 fans to 20 provides a PSEC benefit of about 3%, whereas going from 20 fans to 100 fans only provides a 2% further improvement for conservative 2035 numbers.

Figure 5.17 also shows the effect of DP and BLI on PSEC. At conservative 2035 values, an all-electric aircraft with 2 fans and no BLI offers a PSEC reduction of about 42% over conventional, which increases to 48% with 100 fans and 50% BLI. Little benefit is obtained for values higher than 8 kW/kg since the components' mass make up an increasingly smaller fraction of the aircraft takeoff mass. The flattened PSEC curve also suggests that the metric is less sensitive to component specific powers than it is to
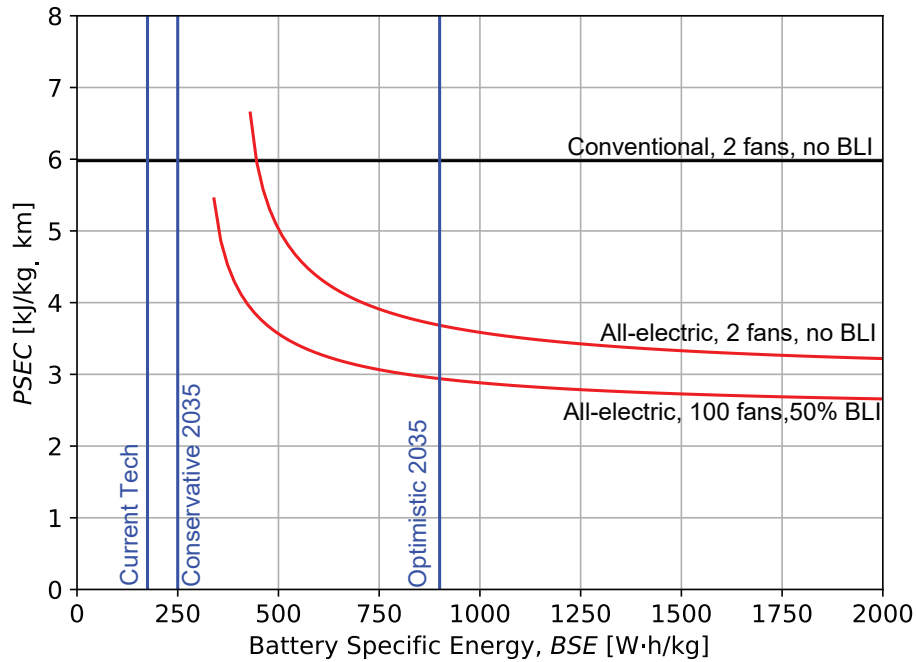
Figure 5.15: Effect of battery technology on $PSEC$ with DP and BLI for 100 nmi all-electric thin-haul aircraft; $[P/m]_{\mathrm{mot}} = 16\,\mathrm{kW/kg}$, $[P/m]_{\mathrm{conv}} = 19\,\mathrm{kW/kg}$, $f_S = 1$, $f_L = 1$.
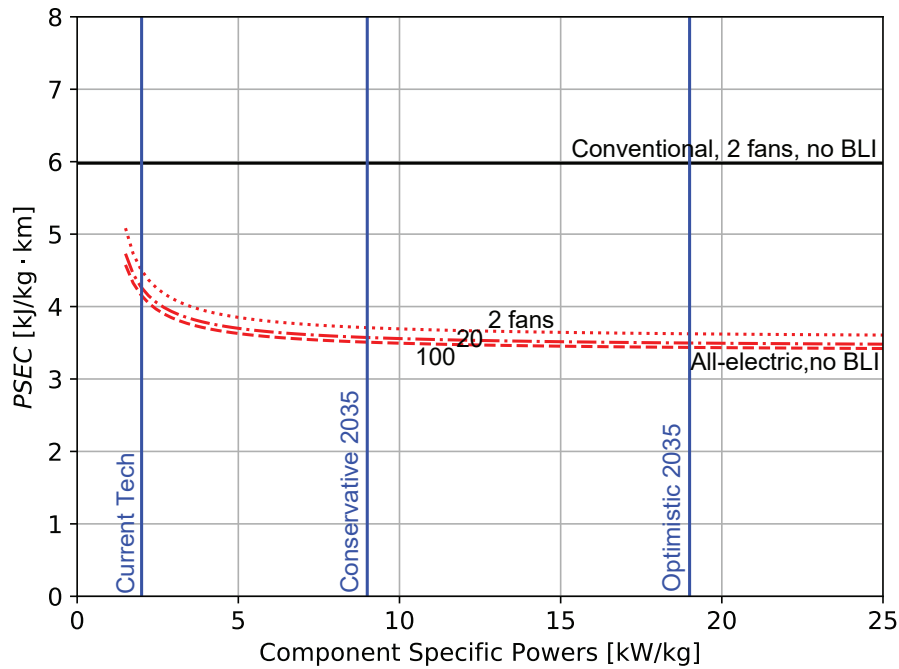
Figure 5.16: Effect of component specific powers on $PSEC$ with DP for 100 nmi all-electric thin-haul aircraft; $BSE = 900\,\mathrm{W\cdot h/kg}$, $f_S = 1$, $f_L = 1$.

battery technology, This indicates that the obstacles for a feasible all-electric aircraft lie with battery technology, rather than with motors and converters.
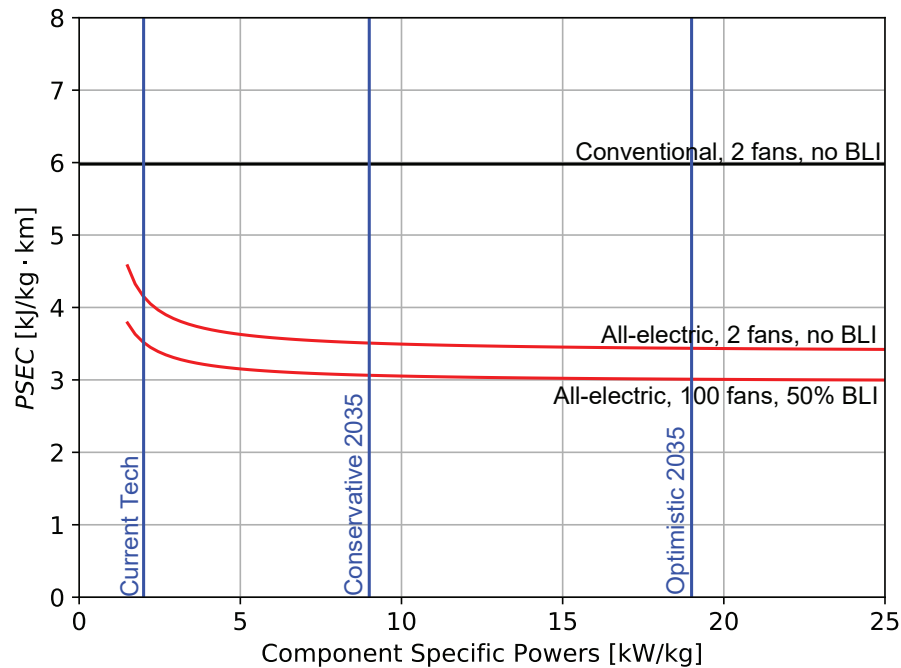
Figure 5.17: Effect of component specific powers on *PSEC* with DP and BLI for 100 nmi all-electric thin-haul aircraft; $BSE = 900$ W·h/kg, $f_S = 1$, $f_L = 1$.

Following this conclusion, a turbo-electric architecture (no batteries) could be feasible even with current technology. Figure 5.18 demonstrates this, here for a larger medium-haul aircraft designed to carry 180 passengers over 3000 nmi. The conventional aircraft has two mechanically driven fans with no BLI and a PSEC of about 4.2 kJ/kg·km. The turbo-electric aircraft has 308 electrically distributed fans, ingesting 20% of the total boundary layer over the fuselage and 50% over the wing.

Even with current technology, the turbo-electric aircraft has a PSEC benefit of 7% over the conventional. This advantage increases to 16% with conservative 2035 technology and to 19% with optimistic 2035 technology. Thus, while all-electric aircraft may be infeasible for longer missions, turbo-electrics are feasible for longer missions. This was demonstrated here for the medium-haul, but was found to be true for all classes.

5.3.3 Technology Analysis Summary

For the different mission profiles, analysis of technology levels shows that currently, batteries have specific energy and power too low to enable all-electric propulsion for all missions. Motor and converter specific powers are high enough to allow turbo-electric aircraft. However, these aircraft have little to no benefit over the corresponding conventional aircraft. Benefits are seen by adding distributed propulsion (DP) and boundary layer ingestion (BLI) enabled by electrification. At conservative 2035 technology levels, battery technology is still too low to render all-electric aircraft feasible. BSE and BSP must increase significantly for all-electric aircraft, even for the smallest class and shortest missions. However, conservative 2035 technology more than adequate to enable turbo-electric aircraft across all missions, providing PSEC benefits over the conventional cases. With optimistic 2035 technology, the results for turbo-electric aircraft stand with greater PSEC reduction, and battery technology also improves enough to enable hybrid- and all-electric thin-haul aircraft, albeit at lower ranges.

Looking at the results from another angle, optimistic 2035 technology allows for all-electric thin-
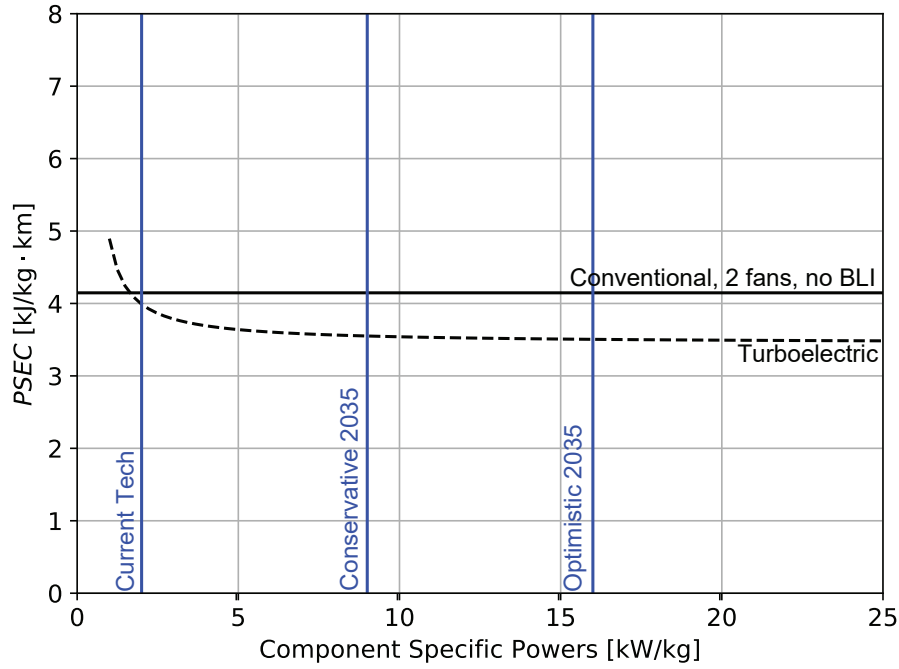
Figure 5.18: Effect of improving component specific powers on PSEC for a medium-haul aircraft; turbo-electric: $f_L = 0.48$, $f_{\text{BLI}_M} = 0.2$, $N_{\text{fan}_M} = 2$, $d_{\text{fan}_M} = 1.14\,\text{m}$, $f_{\text{BLI}_E} = 0.5$, $N_{\text{fan}_E} = 308$, $d_{\text{fan}_E} = 0.104\,\text{m}$.

haul aircraft at a reduced range of 100 nmi with an energy consumption benefit over the conventional case. The design mission of 500 nmi, however, requires a BSE 1.6 times higher than the optimistic 2035 numbers. For a design regional mission (80 passengers, 1500 nmi), the BSE would have to be twice the optimistic prediction for 2035. For all-electric aircraft, specific energy is more important than specific power, so battery technology needs to improve substantially before commercial missions with such aircraft are possible.

If the battery is not in consideration, as with turbo-electric aircraft, design thin-haul, regional, and medium-haul missions are feasible with energy benefit within conservative 2035 specific powers. Overall, improvements in electrical component technology make electrified aircraft feasible, and enable lower energy consumption than the current conventional aircraft.

5.4 Limiting Cases

5.4.1 Wake Propulsion Ideal

As seen in the power balance framework, airframe parameters and propulsion system parameters determine the aero-propulsive performance of an aircraft with or without BLI [2, 8]. Specifically, the power coefficient, $P_K/(D'V_\infty)$, is determined by the fraction of boundary layer ingested, f_{BLI}, the ratio of non-BLI profile drag to total non-BLI drag, D'_p/D', the fraction of non-BLI viscous dissipation occurring before ingestion, f_{surf}, and a propulsor mass flow parameter, $\dot{m}V_\infty/D'$. The power coefficient is the mechanical power delivered to the flow non-dimensionalized by the non-BLI drag power. The power savings coefficient, PSC, is the percentage reduction in flow power for a given BLI airframe relative to the non-BLI flow power.

$$\text{PSC} = \frac{P_{K,\text{non-BLI}} - P_{K,\text{BLI}}}{P_{K,\text{non-BLI}}} \tag{5.1}$$

Table 5.3 identifies the power balance parameters for representative aircraft derived from TASOPT models [17]. These values inform the parameter space in Figures 5.19 and 5.20, which show trends in power coefficient and PSC from full BLI, respectively. The power parameters are plotted as functions of mass flow parameter with vertical lines indicating $\dot{m}V_\infty/D'$ for the identified aircraft. The figures consider multiple values of profile drag fraction and f_{surf} is 0.9.

The figures show lower power coefficients for full BLI cases relative to non-BLI cases, resulting in PSCs greater than 15% for the plotted range of parameters. PSC increases with profile drag fraction because BLI produces benefit from axial wake defects; as more of the total drag is induced drag, BLI accomplishes less power reduction. In the ideal wake case, there is no induced drag and the propulsive streams return the wake to free stream conditions, resulting in the minimum power coefficient with full BLI. With increasing mass flows, propulsor jet velocity decreases and propulsive efficiency increases. This performance improvement affects non-BLI cases more than full-BLI cases, resulting in a decrease in PSC with greater mass flow parameter. An aircraft with representative profile drag fraction ($D'_p/D' =$ 0.65) and a high mass flow parameter ($\dot{m}V_\infty/D' = 3$) can reduce flight power by 18% with full BLI.

Practical considerations may limit the amount of achievable BLI. Partial BLI offers appreciable benefit nonetheless. The change in BLI benefit with f_{BLI} is given by Figure 5.21 for the aircraft described in Table 5.3.

Table 5.3: BLI parameter values for relevant aircraft from TASOPT models

Aircraft	$\frac{\dot{m}V_\infty}{D'}$	$\frac{D'_p}{D'}$	f_{surf}
Boeing 737-800 (CFM56)	1.36	0.66	0.84
Boeing 777-300ER	2.14	0.63	0.84
D8.2b (non-BLI)	1.42	0.65	0.87
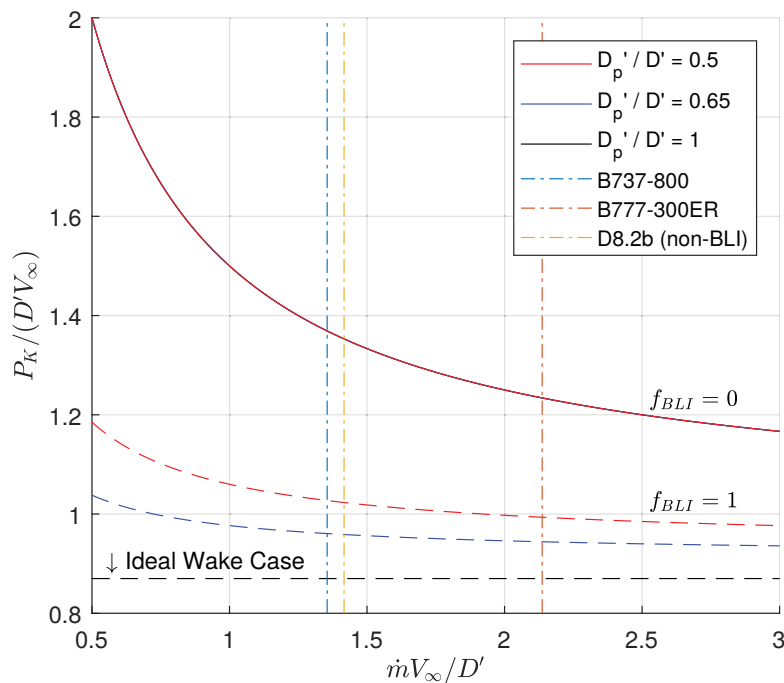
Figure 5.19: Power coefficient variation with BLI parameters as in Table 5.3. Mass flow parameter values given for reference aircraft.
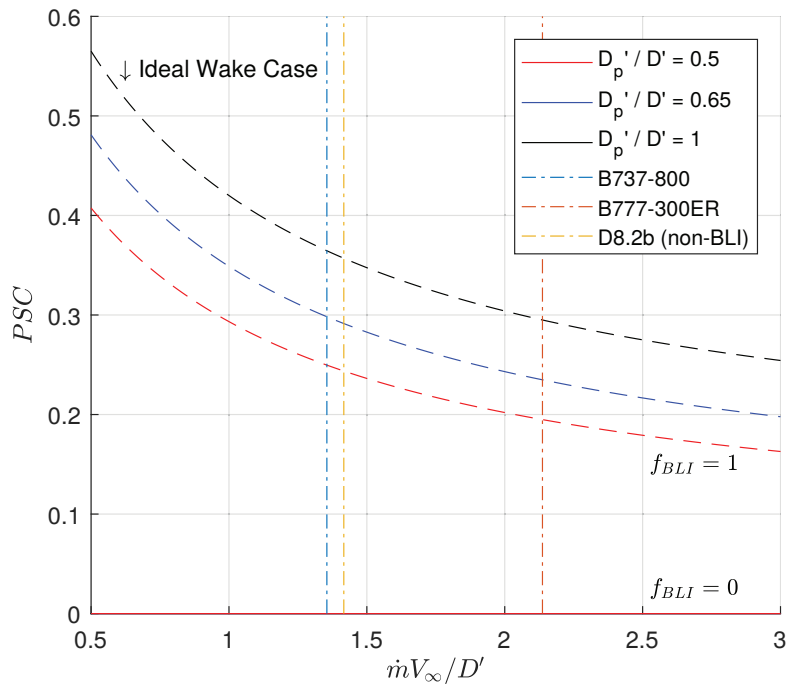
Figure 5.20: Power saving coefficient variation with BLI parameters as in Table 5.3. Mass flow parameter values given for reference aircraft.

The estimated flow power savings can be translated to reduction in fuel weight via a modified Breguet range equation:

$$\text{Range} = \eta_{\text{th}} \left(\frac{h_{\text{fuel}}}{g} \right) \left(\frac{P_K}{D'V_\infty} \right)^{-1} \left(\frac{L}{D'} \right) \ln \left(\frac{W_i}{W_f} \right) \tag{5.2}$$

Figure 5.22 shows fuel weight reduction as a function of BLI fraction for relevant aircraft parameters (Table 5.3) assuming the other factors, such as empty airframe weight, are constant. For full BLI, fuel weight is reduced by up to 30%.

The relative benefit increases when considering fuel burn due to the logarithmic nature of the range equation – less fuel is needed to carry a lighter plane. It should be emphasized, however, that the analysis neglects the impact of alternate (e.g., distributed, electrified) propulsion system configurations on airframe weight and performance. The significant propulsion system changes needed to achieve a high f_{BLI} motivate the higher-fidelity model with which the trade space study was conducted.

5.4.2 Battery Specific Energy

In Section 5.3.3, it was noted that the feasibility and efficiencies of electrified aircraft improves with improvements in technology parameters. Analyses were done based on different predicted technology levels. This section approaches the matter a little differently – how would electrified aircraft perform with the "best of the best" technology numbers? In other words, if the battery is considered, there is a drop in its specific energy and specific power at the aircraft system level compared to the theoretical values. How would the aircraft performance change if the theoretical numbers were used?

For novel lithium-ion chemistries, the lithium-air battery has the highest theoretical specific energy of 3500 W·h/kg. In the literature, values as high as 11,000 W·h/kg are quoted; however, those numbers
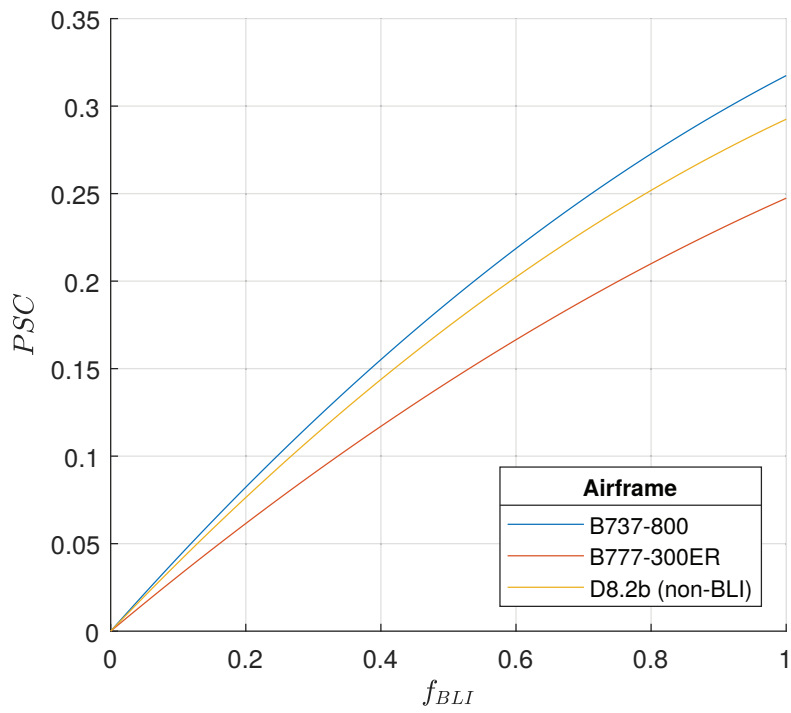
Figure 5.21: Power savings coefficient variation with extent of BLI for reference aircraft at fixed mass flow parameter.
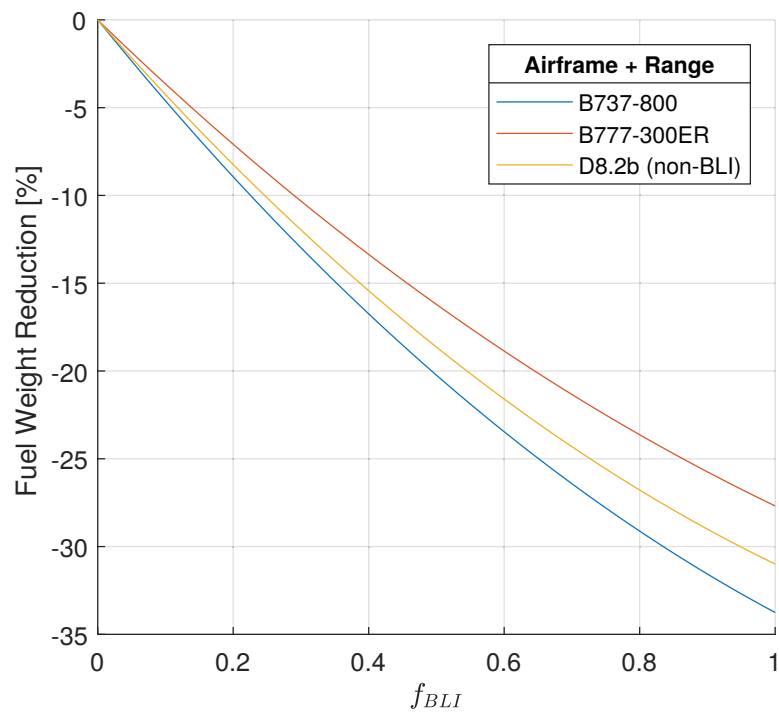
Figure 5.22: Relative fuel weight reduction from ideal BLI for extant aircraft configurations and missions.

are misleading as they only take into account the mass of lithium in the reaction. The other reactant, oxygen, is drawn by the battery from its environment and accumulates, adding to the battery mass as it discharges. When the mass of the oxygen is accounted for, the lower 3500 W·h/kg value is obtained. Using this value, scaling the battery specific power appropriately, and keeping all other parameters at the optimistic 2035 level, each class of all-electric aircraft was flown on its design mission and the resulting productivity-specific energy consumption (PSEC) was compared with the respective conventional aircraft, as shown in Table 5.4.

As can be seen, where the aircraft is feasible, the results show a substantial reduction in the specific energy consumption over the smaller mission. The energy benefit decreases as the mission grows in payload and range. At the Li-ion theoretical BSE of 3500 W·h/kg, the specific energy is still smaller compared to that of hydrocarbon fuel, so as more energy is required on-board, the less the benefit. On the other hand, even this high BSE is not enough to facilitate all-electric aircraft for long haul missions. For those missions, the design will have to be turbo-electric or hybrid-electric even for the highest possible BSE values.

5.4.3   Electrical Component Power Density

In section 5.3.3, it was noted that the electrified designs were a lot more sensitive to battery specific energy (BSE) than to component specific powers. To remove the effects of BSE, only turbo-electric designs were considered in this section, in order to isolate the effects of drastically improving specific powers. In section 5.3.2, it was also observed that the PSEC curves flattened out for increasing specific powers, leading to PSEC benefits with diminishing returns. This section compares the conventional aircraft for each mission with the respective turbo-electric aircraft for the same mission, but with the component specific powers set to 100 kW/kg. The results are shown in Table 5.5.

Across all missions, the high component specific powers enable a reduction in the on-board energy consumed. The PSEC benefits are higher for thin haul and long haul compared to regional and medium haul missions. The varying level of benefits can be attributed to the different baseline turbo-electric designs used in each case, as discussed in section 5.1. In the absence of a minimum fan diameter constraint in the optimizer, the results when the number of electric fans was allowed to float led to a large number (thousands) of very very small (less than micrometer-scale) fans, which was deemed impractical. However, improving component specific powers for turbo-electric designs results in smaller PSEC benefits compared to improving BSE for all-electric designs, so this drastic improvement in component specific powers is unlikely to yield substantial PSEC benefits over the optimistic 2035 predictions.

Table 5.4: Comparison of all-electric with limiting BSE vs conventional

Mission	Conventional PSEC [kJ/kg·km]	All-electric PSEC [kJ/kg·km]	Percent benefit
Thin haul	6.593	2.816	57.3%
Regional	5.764	3.080	46.6%
Medium haul	4.147	2.713	34.6%
Long haul	8.247	–	–

Table 5.5: Comparison of turbo-electric with limiting specific power vs conventional

Mission	Conventional PSEC [kJ/kg·km]	Turbo-electric PSEC [kJ/kg·km]	Percent benefit
Thin haul	6.593	4.860	26.3%
Regional	5.764	4.898	15.0%
Medium haul	4.147	3.467	16.4%
Long haul	8.247	5.757	30.2%

6 Conceptual Design Framework Extensions

6.1 Detailed Electric Component Design Model

This section presents electric component models that incorporate additional information (e.g., maximum operating voltage and current) for estimation of their specific power and efficiency. These higher-fidelity models could be substituted into the analyses that have been described, which used specified efficiency and specific power, to explore the electric propulsion system design space in more depth.

6.1.1 Cable Model

The cable model captures the impact of operating the propulsion system at different voltage and current levels. From Appendix B, the efficiency of the cable is,

$$\eta = \frac{P_{\text{load}}}{P_{\text{source}}} = \frac{P_{\text{load}}}{P_{\text{load}} + I^2 R}. \tag{6.1}$$

For a fixed load power, the efficiency can be increased by either decreasing the resistance of the cable or decreasing the current (i.e., increasing the source voltage).

The cable resistance is,

$$R = \rho \frac{\ell}{A_c}, \tag{6.2}$$

where ρ is the cable resistivity, ℓ its length, and A_c its conductor cross-sectional area. The resistivity is fixed by the choice of conductor material, and the length of the cable is fixed by the aircraft configuration, thus the remaining degree of freedom to change the cable resistance is the conductor area; the efficiency of the cable can be improved by increasing A_c. However, the mass of the cable is directly proportional to A_c, and there is a trade-off between cable specific power and efficiency. Figure 6.1 shows this trade-off for a cable using the material parameters from Appendix B; increasing the conductor area yields diminishing marginal benefits in efficiency. A 6 meter cable that delivers 250 kW of power to the load at 270 Vdc was assumed, values which may be representative of a real aircraft power cable.
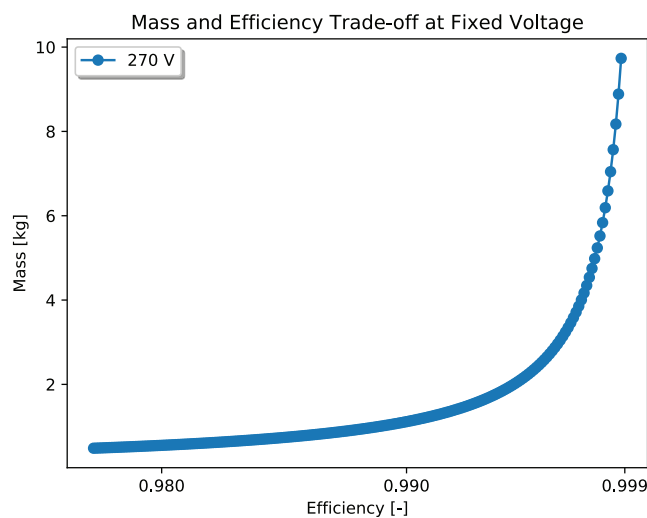
Figure 6.1: The conductor area presents a trade-off between cable mass and resistance (i.e., efficiency).

The efficiency of the cable can also be improved by decreasing the current. However, the necessarily larger source voltage increases the dielectric thickness of the cable, which increases its mass. Figure 6.2 shows a similar trade-off between mass and efficiency for a 250 kW cable as that in Fig. 6.1, at different voltage levels. An increase in voltage results in a lighter cable, but there is a diminishing marginal benefit. This is relevant to aircraft power systems which are traditionally limited to low voltages due to electric breakdown concerns.

6.1.2 Electrical Machine Model

A survey on motor power-to-mass ratios shown in Fig. 6.3 shows that power-to-mass ratio is not constant across rated power [18].

Generally, the power-to-mass ratio improves at lower power levels, but even then spans a wide range. This variation depends on a variety of factors, such as cost, materials, cooling technology, and rotor integrity (burst limit). To capture these effects and better understand these trade-offs, a more
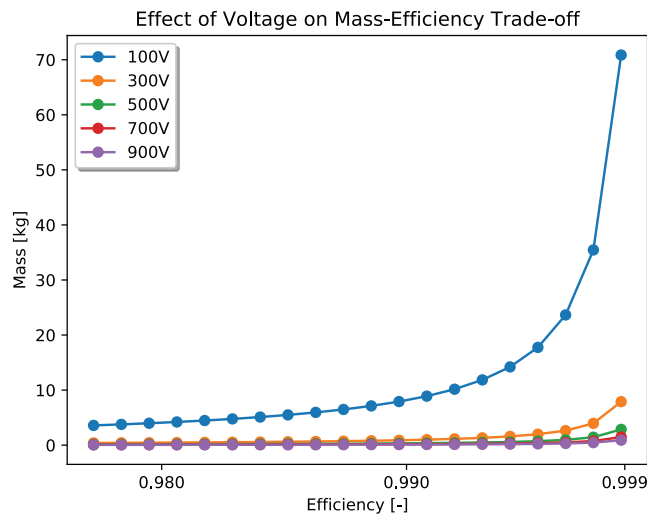
Figure 6.2: Increasing voltage improves the cable efficiency but gives diminishing marginal benefit.
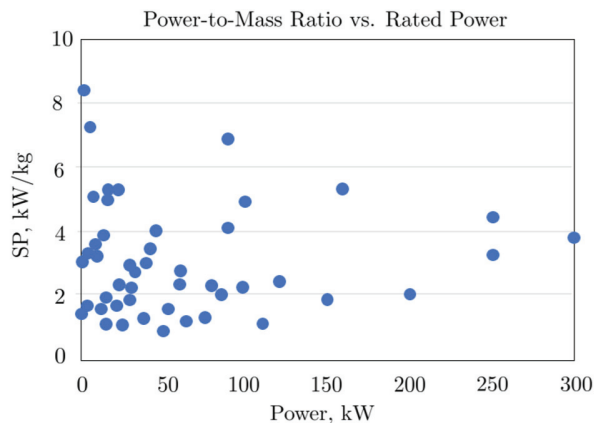
Figure 6.3: Survey of power-to-mass ratios versus rated power for a variety of motors [18].

detailed, GPkit-compatible electrical machine model was developed as documented in Appendix B.

Data from existing electrical machines for vehicular applications was used to assess the fidelity of the model. First, the dimensions and material properties from the MIT Cheetah Motor [19], shown in Fig. 6.4, were substituted into the analytic expressions captured in Appendix B. This motor uses Neodymium magnets and Hiperco-50 steel. The angular speed and hence power level of this motor were not specified, so torque and masses only were checked, as in Tab. 6.1.

Second, an MIT outer rotor, electric automobile motor [20] was used for verification. This motor was designed with chromate plated NdFeB magnets and 29 Gage M-19 steel. The power level and angular speed were also not specified, so only torque and mass were compared, as in Tab. 6.2. The constituent masses (e.g., the magnet mass) differ by larger percentages, which may be explained from the motor design considering additional details such as slot skewing [20].

The motor model can be used to explore trade-offs between design parameters. Fig. 6.5 shows the trade-off between specific power and ohmic heating losses from optimizing the motor geometry while varying the current density for a motor designed for 25 kW, 2000 rpm, and 200 m/s tip speed.

Reference [21] shows that the trade-off between specific power and efficiency is due to the armature reaction of the machine. For a machine with saturated teeth operating at the theoretical shear stress limit, the theoretical efficiency due to ohmic heating losses is given by [21]

$$\eta = 1 - 2\sqrt{2}\frac{\rho J}{B_{\text{sat}}U} \tag{6.3}$$

where J is the slot current density, B_{sat} is the saturation flux density in the magnet material, and U is the tip speed.
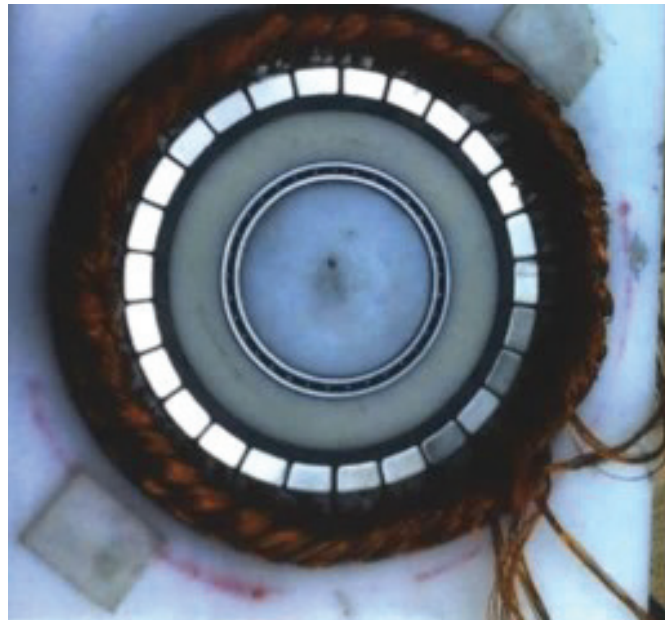
Figure 6.4: Photo showing the layout of the MIT Cheetah Motor [19].

Table 6.1: Gen-2 Cheetah Robot Inner Rotor

Parameter	Predicted	Measured [19]	% Difference
Mass	1.05 kg	1.07 kg	1.9%
Torque	42 Nm	42.36 Nm	0.85%

Table 6.2: Electric Automobile Outer Rotor

Parameter	Predicted	Measured [20]	% Difference
Mass	24.5 kg	25.1 kg	2.4%
Magnets	1.88 kg	1.7 kg	10.7%
Rotor Back-Iron	5.87 kg	5.9 kg	0.5%
Stator Teeth	5.57 kg	6.6 kg	-15.6%
Stator Back-Iron	4.80 kg	4.8 kg	0%
Conductors	6.36 kg	6.1 kg	4.3%
Torque	457.1 Nm	450 Nm	1.6%
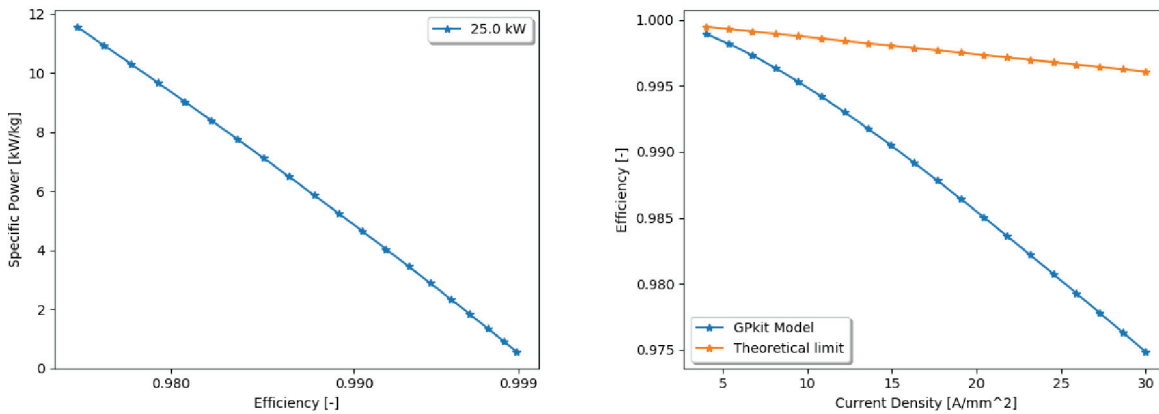
Figure 6.5: A Pareto frontier of the motor specific power and efficiency (left) and the Ohmic heating loss compared to the theoretical limit from Ref. [21] (right).

Figure 6.5 shows that the model captures this trend. An increase in current density results in greater Ohmic heating losses, but also a lighter motor because the conductor size can be decreased. This result was generated by optimizing the motor model to minimize mass while varying the maximum allowable slot current density. The motor load power, angular speed, and tip speed were held constant at 25 kW, 2000 rpm, and 200 m/s, respectively. If this model was incorporated into an aircraft configuration and mission, these parameters could also be variables optimized to minimize the vehicle-level objective.

6.2 Aircraft Conceptual Design Model

This section presents the results of a signomial programming (SP) airframe conceptual design model, applied to the NASA STARC-ABL turbo-electric aircraft configuration [22,23]. The mission performance, propulsion system, and aero-propulsive performance models described in Section 4 are used, but the aero-structure model has been replaced with higher-fidelity sizing and performance models for the airframe components listed in Table 6.3. The objective was to extend the trade space exploration tool to a fidelity suitable for conceptual design of a commercial aircraft while retaining the benefits of the GP optimization approach. The details of the component models are provided in Appendix C.

6.2.1 Comparison with Existing Aircraft Data

Figure 6.6 shows an assessment of estimated aircraft empty mass for a range of commercial transports currently in production. Inputs to this sizing-only model are wing, fuselage, and tail dimensions, max

Table 6.3: Airframe and propulsion sub-system component models

Sub-system	Components	Sizing Model	Performance Model
Airframe	Fuselage	Torenbeek [24]	Schaufele drag fit [25]
	Wing	Raymer [15]	Oswald efficiency, airfoil polar fits
	Vertical tail	Torenbeek	TASOPT drag model [26]
	Horizontal tail	Torenbeek	TASOPT drag model
	Nacelle	TASOPT weight buildup	TASOPT drag model
	Non-propulsive systems	TASOPT weight buildup	
Propulsion	Gas generator core	corrected flow cube-squared	specified thermal efficiency
	Ducted fan	corrected flow cube-squared	specified efficiency
	Electric generator	specified power density	specified efficiency
	Power electronics	specified power density	specified efficiency
	Electric motor	specified power density	specified efficiency
	Thermal management	specified mass per heat flow	
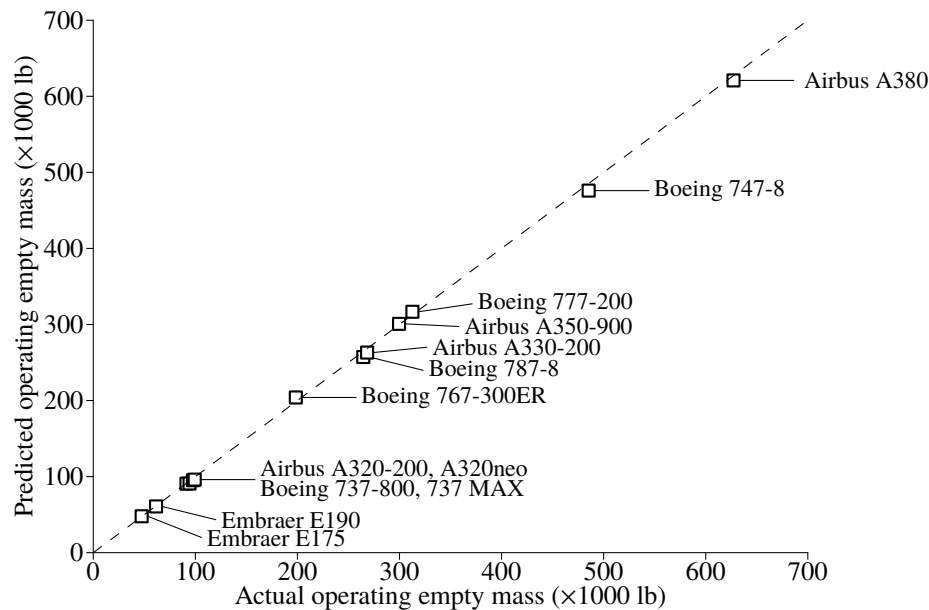
Figure 6.6: Predicted vs actual operating empty weight for range of commercial transport aircraft.

payload and max takeoff mass, propulsion system mass, and fan diameter, all of which were obtained from aircraft and engine Type Certificate Data Sheets and Airport Planning Manuals. The model is a GP with 45 design variables, which solves in approximately 0.1 seconds on a personal computer. The model matches empty mass to within 4% of design data for aircraft from regional to super-jumbo scale. The mass of the Boeing 787 and Airbus A350 are well-predicted without accounting in any way for the primarily composite construction of the airframe, suggesting mass reduction factors [15, 24] used to estimate composite fuselage structural mass may be optimistic.

Figure 6.7 shows the empty mass buildup compared with the Boeing SUGAR Free and Refined SUGAR single aisle concepts [13]. The model shows excellent agreement with the data, capturing component component masses to within 20%, and matching overall empty weight to within 3% for both designs. For the Refined SUGAR model, component mass reduction factors of 8%–16% were applied, consistent with the N+3 advanced composite technology assumptions; combined with reduced fuel mass due to improved efficiency, this results in a 14% reduction in empty mass relative to the
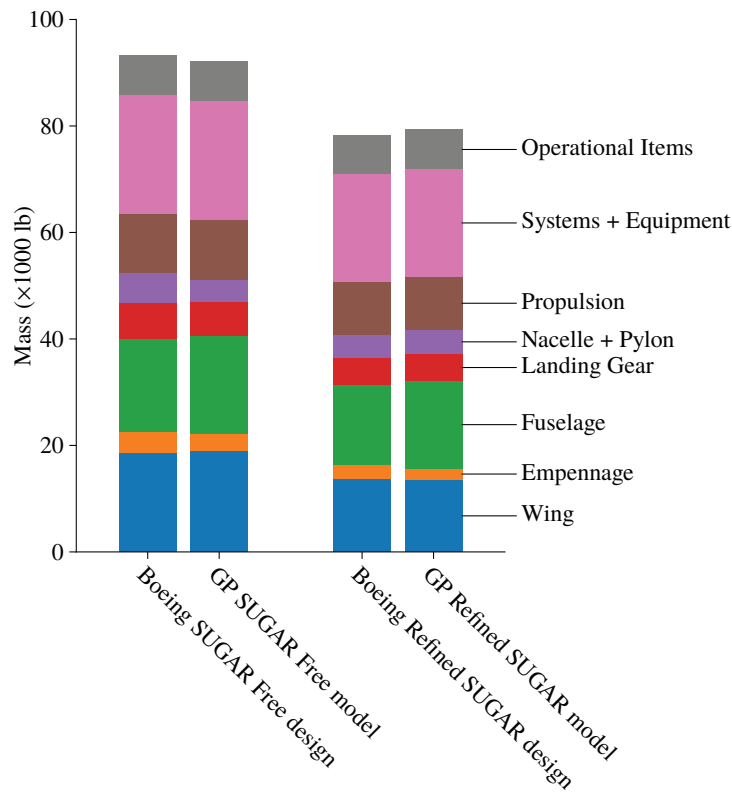
Figure 6.7: Comparison of SUGAR aircraft concept empty weight buildup; published design [13] vs current model; baseline and N+3 technology assumptions.

baseline technology SUGAR Free. In the next section, the Refined SUGAR model is used as a baseline for comparison of the STARC-ABL configuration, consistent with the N+3 time frame assumed for the original design [22, 23].

6.2.2 Conventional Tube-and-Wing Baseline Performance

To calibrate and assess the configuration performance model and to provide a baseline for comparison with the STARC-ABL configuration, we have developed a model for the Refined SUGAR concept. Table 6.4 lists the model inputs and provides a comparison of the published sizing and performance with the model estimates. The gas generator specific power and thermal efficiency were selected to yield agreement in engine bypass ratio and thrust-specific fuel consumption, as described in the previous section. The inclusion of a reserve range fraction of 15% results in less than 1% error in predicted maximum takeoff mass. The resulting model matches the sizing and performance parameters in the range equation – empty mass, max takeoff mass, fuel consumption, and lift-drag ratio – to within 0.5%. The mission fuel burn is underpredicted by 3%. The largest discrepancies are the propulsion system mass and tail moment arms, indicating potential room for improvement in the ducted fan, gas generator, and tail sizing descriptions.

6.2.3 STARC-ABL Configuration Performance

Table 6.5 lists the design variables for the baseline Refined SUGAR model and an equivalent STARC-ABL configuration. Payload mass, range, cruise altitude and Mach number, wing span, fuselage dimensions, tail moment arms, and wing loading were held constant to provide a fair comparison of the concepts (i.e.,

Table 6.4: Comparison of conventional tube-and-wing baseline configuration model with Boeing Refined SUGAR sizing and performance

	Parameter		Refined SUGAR [13]	Baseline Configuration	
Inputs	Payload mass	[lb]	46,000		
	Range (max payload, +15% reserve)	[nmi]	1450		
	Cruise altitude	[ft]	37,000		
	Cruise Mach number		0.74		
	Wing reference area	[ft^2]	1358		
	Wing span	[ft]	118		
	Wing taper ratio		0.16		
	Wing sweep	[deg]	20.1		
	Horizontal tail area	[ft^2]	268		
	Horizontal tail aspect ratio		6.24		
	Vertical tail area	[ft^2]	213		
	Vertical tail aspect ratio		1.94		
	Fuselage length	[ft]	125		
	Fuselage diameter	[ft]	12.7		
	Fan diameter	[in]	70		
Outputs	Propulsion system mass	[lb]	9027	8124	(-10%)
	Operating empty mass	[lb]	77,042	77,030	(-0.02%)
	Max takeoff mass	[lb]	**136,412**	**135,900**	**(-0.4%)**
	Wing loading	[lb/ft^2]	100	100	(–)
	Horizontal tail moment arm	[ft]	60.7	53.0	(-13%)
	Vertical tail moment arm	[ft]	56.3	50.8	(-10%)
	Lift-to-drag ratio		**20.9**	**20.9**	**(–)**
	Thrust-specific fuel consumption	[1/hr]	**0.528**	**0.529**	**(+0.2%)**
	Mission fuel mass	[lb]	**13,370**	**12,910**	**(-3%)**

both aircraft can be assumed to meet similar constraints such as balanced field length requirements). The STARC-ABL propulsion systems fan diameters and electric motor power were specified, consistent with the most recent STARC-ABL design revision [23]. Performance calculations yield a 5.4% *increase* in fuel required for the mission being considered (max range at max payload).

Examination of the optimized design variables shows that the specified STARC-ABL propulsion system trades reduced specific fuel consumption for increased mass and drag. The reduced under wing fan diameter yields a 8% reduction in turbofan mass, but the total propulsion system mass is 38% higher than the baseline turbofan, in large part due to the tail cone fan mass. The re-sized distributed propulsion system results in a 23% increase in total nacelle mass and a 28% increase in total nacelle drag. In total, the empty mass is 7% higher and the lift-drag ratio is 2% lower than the Refined SUGAR baseline. On the other hand, the increased losses in the electric distribution system and the mixing of the under wing jet (which has a lower propulsive efficiency than the conventional baseline) are more than offset by propulsive power savings of BLI, yielding a net decrease in thrust-specific fuel consumption of 1.5%.

6.2.4 Sensitivity of Performance to Model Parameters

As described in Section 4.2, a benefit of the GP optimization approach is that parameter sensitivities of the objective function are provided as part of the solution. Figure 6.8 shows the 30 parameters with the largest sensitivities in our STARC-ABL model, grouped into parameters related to mission, propulsion system, and airframe. The values are the magnitudes of the *Lagrange multipliers* for each parameter, which indicate the relative change in the objective function that would result for a given relative change

Table 6.5: Comparison of baseline and STARC-ABL configuration sizing and performance

Parameter		Baseline Configuration	STARC-ABL Configuration	
Max takeoff mass	[lb]	135,900	141,800	(+4.3%)
Operating empty mass	[lb]	**76,940**	**82,210**	**(+6.8%)**
Under wing nacelle mass (×2)	[lb]	2212	1573	(-29%)
Tail cone nacelle mass	[lb]	–	2311	
Total propulsion system mass	[lb]	**8124**	**11,190**	**(+38%)**
Under wing fan diameter	[in]	70	57	(-19%)
Turbofan mass (×2)	[lb]	4062	3755	(-7.6%)
Generator mass (×2)	[lb]	–	238	
Rectifier mass (×2)	[lb]	–	183	
Cable mass	[lb]	–	451	
Circuit protection mass	[lb]	–	226	
Inverter mass	[lb]	–	357	
Thermal management system mass	[lb]	–	110	
Motor mass	[lb]	–	438	
Tail cone fan diameter	[in]	–	77	
Tail cone fan mass	[lb]	–	1261	
Wing area	[ft^2]	1358	1417	(+4.3%)
Wing aspect ratio		10.3	9.8	(-4.9%)
Airframe lift-drag ratio (L/D')		**20.9**	**20.4**	**(-2.4%)**
Effective TSFC ($\dot{m}_{\text{fuel}}g/D'$)	[1/hr]	**0.529**	**0.521**	**(-1.5%)**
Mission fuel mass	[lb]	**12,910**	**13,610**	**(+5.4%)**

in the parameter in question, including the effect of re-optimization. Red bars indicate positive sensitivities, for which an increase in the parameter results in an (undesired) increase in the objective function; conversely, blue bars indicate negative sensitivities, where an increase in the parameter decreases the objective function. Sensitivities are local, i.e., they only indicate the direct effect of small changes in parameters, so that larger changes have a nonlinear impact on the objective function. Further, the sensitivities will change with a change in design parameter; for example, in the case of the optimized propulsion system presented in the next section, the sensitivities to fan diameter go to zero as they are optimized.

In many cases, the sensitivities indicate well-understood impact of design parameters or level of technology on overall performance. For example, the large sensitivities of fuel burn to payload mass, range, thermal efficiency, and fan efficiency show the direct effect of those parameters on the range equation. The largest sensitivity, which is to maximum wing span, is because higher aspect ratios and lift-drag ratios can be achieved with larger span. A majority of the smaller sensitivities shown are constant factors that directly impact component mass or drag. In some cases, sensitivities can point to an issue with the model. For example, the large sensitivity to cruise altitude an artifact of the fan sizing model, which assumes a fixed altitude, and thus does not capture the correct trend with free stream stagnation conditions. Another parameter of this type is the tail cone fan efficiency, which is assumed constant, but could be degraded due to inlet distortion; in this case the sensitivity provides useful information about how such changes in efficiency would impact overall performance.

The sensitivities to number of under wing engines and both fan diameters suggest design choices to improve overall configuration performance. The former is the benefit of distributed propulsion; more small propulsors yield better performance than fewer large ones, assuming the nacelle, fan, and core sizing and performance models are appropriate at smaller scale. The latter indicates the specified fan sizes, and thus the design fan pressure ratios, are not optimal for minimum fuel burn.
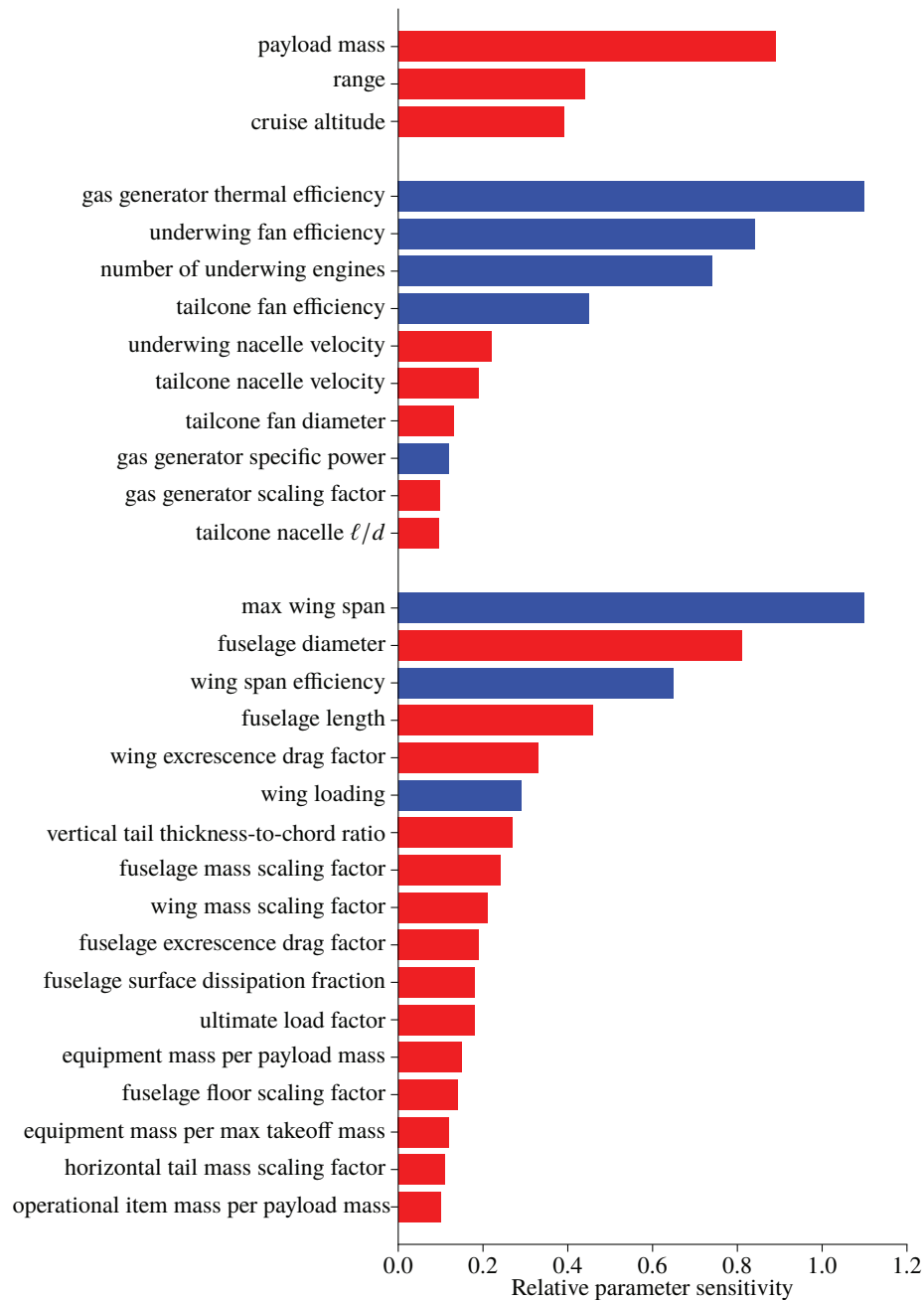
Figure 6.8: Sensitivities of baseline STARC-ABL configuration fuel burn to constant design parameters.

6.2.5 Propulsion System Optimization

A second STARC-ABL configuration model with optimized fan diameters and electric motor power was also considered to determine the minimum fuel burn for a fixed airframe. To provide a fair comparison, the Refined SUGAR fan diameter was also optimized, with the results shown in Table 6.6. The baseline tube-wing configuration is seen to be near-optimal, with optimization increasing the fan diameter from

70 to 73 inches, yielding a 10 lb (0.1%) decrease in mission fuel. Optimization of the STARC-ABL configuration, on the other hand, leads to a quite different propulsion system than the specified design, with under wing fan diameters approaching that of the tube-wing design, and the electric motor power reduced by 72%.[6] This results in a 5% improvement in performance over the initial design, but the optimized STARC-ABL configuration consumes 0.5% more fuel than the optimized baseline tube-wing configuration.[7]

The limited fidelity of the propulsion system models (to which the fuel burn benefit has been shown to be sensitive) and the limited scope of the design study do not allow us to draw any firm conclusions concerning the benefit of the STARC-ABL configuration. It is also worth mentioning that the present analysis assumes a mission and conventional configuration baseline based on the Refined SUGAR concept [13], with different design parameters – cruise Mach number and design range – than that of the initial STARC-ABL studies [22, 23]. For the current assumptions, the results suggest the STARC-ABL concept is near the "break-even" point, with little or no benefit in performance over a advanced technology baseline with conventional turbofan propulsion. The sensitivity and optimization analyses also show the importance of system-level optimization for new configurations, where system performance trades of conventional designs do not apply, and typical design choices based on engineering judgment may not provide the best performance.

Table 6.6: Comparison of conventional tube-and-wing and STARC-ABL configuration sizing and performance with and without propulsion system optimization

		Baseline Tube-Wing	Optimized prop. sys.		Baseline STARC-ABL	Optimized prop. sys.	
Under wing fan diameter	[in]	70	73	(+4.3%)	57	68	(+19%)
Tail cone fan diameter	[in]	–	–		77	29	(-62%)
Tail cone motor power	[hp]	–	–		3500	972	(-72%)
Total propulsion system mass	[lb]	8124	8401	(+3.4%)	11,190	9231	(-18%)
Effective TSFC ($\dot{m}_{\text{fuel}}g/D'$)	[1/hr]	0.529	0.522	(-1.3%)	0.521	0.522	(+0.3%)
Effective lift-drag ratio (L/D')		20.9	20.8	(-0.5%)	20.4	20.8	(+2.0%)
Operating empty mass	[lb]	77,030	77,780	(+1.0%)	82,210	78,490	(-4.5%)
Max takeoff mass	[lb]	135,900	136,700	(+0.6%)	141,800	137,400	(-3.1%)
Mission fuel mass	[lb]	**12,910**	**12,900**	**(-0.1%)**	**13,610**	**12,960**	**(-4.8%)**

---

[6]To approximate the effect of the smaller tail cone fan on the amount of BLI, f_{BLI_f} is assumed to scale linearly with fan diameter, with a value of unity at the initial design diameter of 77 inches.

[7]The fact that the STARC-ABL doesn't simply optimize to the conventional configuration is an artifact of the cable model, which is effectively a fixed weight associated with the electric distribution system, regardless of size, combined with the slight BLI benefit that can be achieved if it is used.

7 Aspects Not Addressed and Questions for Future Research

The scope of the current program meant that there were a number of relevant aspects that we could not address. First, the analysis carried out was quasi-steady and aimed at the cruise condition; It did not include off-design performance and examination of electrical and mechanical dynamical systems in terms of stability and control of aircraft, propulsion operability, and electric power distribution. We also did not consider other (i.e., more than direct propulsive efficiency or weight) possible benefits from distributed propulsion and boundary layer ingestion.

The next steps involve the trajectory from trade-space analysis to the research needed to enable concept and design. At a high level, these questions are:

- How do we create an efficient distributed propulsion system?
- How do we create high levels of boundary layer ingestion efficiently?
- If either of the above is accomplished electrically, what are the challenges of the electrical distribution network?

Questions such as the above can be asked at a fundamental level, but their resolution casts a light up the TRL ladder. They call for basic analysis and computation, coupled with targeted experiments to design the technology paths. They also call for close integration of different fields of expertise to address, as a team, a challenge that cuts across disciplines.

The next level of attack should involve the development of integrated sub-systems and demonstration of performance to increase TRL of enabling technologies. For airframe-propulsion integration, these are distributed propulsion (DP) for ultra-low fan pressure ratio (ULFPR), boundary layer ingestion (BLI), lift augmentation, and flight control. For the propulsor module, these are electro-mechanically integrated fan and motor sub-systems including aero-thermal integration of fan flow and thermal management system. For the electrified propulsion system, the configuration of the architecture (turboelectric, hybrid, partial, etc.) serves as an enabling concept across system-level trades.

Technical challenges associated with these system attributes include

- *Ultra-integrated electrified vehicle concept design and performance estimation* – Develop and use new multi-disciplinary design tools to define and analyze commercial aircraft concepts that leverage increased integration of vehicle subsystems and electrified propulsion system architectures to reduce noise, emissions, and fuel/energy consumption with operating costs favorable compared with conventional designs.

- *High specific power electrical machines, drives, transformers, and protection equipment* – Introduce ultra-efficient electrical components to reduce total electro-mechanical energy conversion and transmission losses and develop high-fidelity multi-physics models for system integration.

- *Thermal management of electrified propulsion systems and components* – Integrate of thermal management into early stage conceptual design of electric power distribution system for optimal allocation of losses and weight across different components.

- *Electric vehicle system dynamics* – Develop analytical methodologies to describe design and off-design performance including examination of electrical and mechanical dynamical systems in terms of stability and control of aircraft, propulsion operability, and electric power distribution. This implies assessment of interactions between systems with different characteristic dynamic time scales. A preliminary analysis of this type was developed under the current effort, and is documented in a separate report [28].

- *Airframe-integrated distributed propulsion for improved aerodynamics* – Leverage flexibility of electric-drive distributed propulsion to enable ultra-low fan pressure ratios, boundary layer ingestion, and

flow control to improve propulsive efficiency, reduce effective drag, and reduce wing, tail, trim, and control surface area and weight.

- *Compact, efficient electric propulsor module design* – Integrate the aerodynamic, mechanical, electrical, and thermal design optimization of electrically-powered propulsors to enhance overall specific power, efficiency, disturbance rejection, operability, noise, and off-design performance.

Appendix A

Trade Space Analysis Models

This section describes the details of the mission integration, aero-structure sizing, aero-propulsive performance, and electric propulsion system architecture models that make up the trade space analysis. Each model consists of a set of governing equations that can be formed as GP or SP constraints, a list of design variables to be optimized, and a list of constant parameters defining the mission and technology assumptions.

A.1 Mission Integration

The aircraft zero fuel mass is the sum of the airframe empty mass, propulsion mass (defined in later sections), battery mass (defined below), and a specified payload mass; the takeoff mass is the sum of the zero fuel mass and the mission fuel mass.

$$m_{\text{ZF}} = m_{\text{airframe}} + m_{\text{prop}} + m_{\text{batt}} + m_{\text{payload}} \tag{A1}$$

$$m_{\text{TO}} = m_{\text{ZF}} + m_{\text{fuel}} \tag{A2}$$

The mission fuel mass is defined using a form of the Breguet Range Equation, assuming the fuel mass flow is proportional to the mass of the vehicle (i.e., constant lift-to-drag ratio and thrust-specific fuel consumption). For all-electric architectures, the fuel mass is zero; for hybrid-electric architectures, the required fuel flow is reduced by power supplied by the battery, but the expression for total fuel consumption is unchanged. To make the expression GP, the exponential function is represented with a truncated Taylor series expansion, with $N = 4$ terms seen to be more than sufficient to provide accurate results.

$$m_{\text{fuel}} = m_{\text{ZF}} \left[\exp\left(\frac{\dot{m}_{\text{fuel}}}{m_{\text{TO}}} \frac{R}{V} \right) - 1 \right] \tag{A3}$$

$$\approx m_{\text{ZF}} \sum_{i=1}^{N} \frac{1}{i!} \left(\frac{\dot{m}_{\text{fuel}}}{m_{\text{TO}}} \frac{R}{V} \right)^i \tag{A4}$$

The total battery energy required is defined similarly assuming the battery power is proportional to to the mass of the vehicle. For conventional architectures, the battery mass is zero; for all-electric architectures, the battery power consumption is constant, simplifying the analysis.

$$E_{\text{tot}} \geq \frac{\dot{E}_{\text{batt}}}{(\dot{m}_{\text{fuel}}/m_{\text{TO}})} \left[1 - \exp\left(-\frac{\dot{m}_{\text{fuel}}}{m_{\text{TO}}} \frac{R}{V} \right) \right] \tag{A5}$$

$$\approx \frac{\dot{E}_{\text{batt}}}{(\dot{m}_{\text{fuel}}/m_{\text{TO}})} \frac{\sum_{i=1}^{N} \frac{1}{i!} \left(\frac{\dot{m}_{\text{fuel}}}{m_{\text{TO}}} \frac{R}{V} \right)^i}{\sum_{i=0}^{N} \frac{1}{i!} \left(\frac{\dot{m}_{\text{fuel}}}{m_{\text{TO}}} \frac{R}{V} \right)^i} \tag{A6}$$

$$\tag{A7}$$

The battery mass related to both minimum energy requirement and the maximum battery power through the BSE and BSP, from which the battery efficiency is also determined, using a simple voltage-resistance circuit model.

$$m_{\text{batt}} = \frac{E_{\text{tot}}}{\text{BSE}} \tag{A8}$$

$$m_{\text{batt}} = \frac{P_{\text{max}}}{\text{BSP}} \tag{A9}$$

$$P_{\text{batt}} \leq P_{\text{max}} \tag{A10}$$

$$4\eta_{\text{batt}}(1 - \eta_{\text{batt}}) = \frac{P_{\text{batt}}}{P_{\text{max}}} \tag{A11}$$

$$\dot{E}_{\text{batt}} = \frac{\dot{E}_{\text{batt}}}{\eta_{\text{batt}}} \tag{A12}$$

Tables A1 and A2 list the design variables to be optimized and constant parameters related to the vehicle sizing and mission energy consumption.

Table A1: Mission integration design variables

Quantity	Dimension	Description
E_{tot}	Wh	total battery energy capacity
$\dot{E}_{\text{batt}}$	W	battery discharge rate
m_{airframe}	kg	empty airframe mass; no propulsion system
m_{batt}	kg	battery mass
m_{fuel}	kg	mission fuel mass
m_{prop}	kg	propulsion system mass
m_{TO}	kg	aircraft takeoff mass
m_{ZF}	kg	aircraft zero fuel mass
$\dot{m}_{\text{fuel}}$	kg	cruise fuel consumption (at takeoff mass)
P_{max}	W	max battery power
η_{batt}	-	battery efficiency

Table A2: Mission integration constant parameters

Quantity	Value	Dimension	Description
BSE	175 / 250 / 900[A1]	Wh/kg	battery specific energy
BSP	520 / 745 / 2700	W/kg	battery specific power
m_{payload}	20 / 80 / 180 / 350[A2]	×215 lb	payload mass
R	500 / 1500 / 3000 / 6000	nmi	range
V	77 / 233 / 233 / 249	m/s	cruise velocity

[A1]Values for current state of the art, conservative 2035, and optimistic 2035 technology assumptions, respectively, defined in Section 3.

[A2]Values for thin haul, regional, medium haul, and long haul, respectively.

A.2   Aero-Structure Sizing

The airframe empty mass is modeled using scaling based on approximate sizing of the wing, tail, and fuselage surface areas. The wing is sized based on an assumed wing loading for each vehicle class, the tails are sized using fixed tail volume coefficients, and the fuselage is sized based on specified cabin dimensions.

$$S_{\text{wing}} = \frac{m_{\text{TO}}}{W/S} \tag{A13}$$

$$S_{\text{HT}} = c_{\text{HT}} \frac{bS_{\text{wing}}}{\frac{1}{2}\ell_{\text{fuse}}\text{AR}} \tag{A14}$$

$$S_{\text{VT}} = c_{\text{VT}} \frac{bS_{\text{wing}}}{\frac{1}{2}\ell_{\text{fuse}}} \tag{A15}$$

$$S_{\text{fuse}} = \pi d_{\text{fuse}}\ell_{\text{fuse}} \tag{A16}$$

The mass of each component is determined using approximate correlation-based methods suggested by Raymer [15], with constants modified to better fit recent conceptual design data obtained using TASOPT [17].

$$m_{\text{wing}} = K_{\text{wing}} \frac{S_{\text{wing}}^2}{b} \tag{A17}$$

$$m_{\text{HT}} = K_{\text{HT}}S_{\text{HT}} \tag{A18}$$

$$m_{\text{VT}} = K_{\text{VT}}S_{\text{VT}} \tag{A19}$$

$$m_{\text{fuse}} = K_{\text{fuse}}S_{\text{fuse}} \tag{A20}$$

$$m_{\text{gear}} = K_{\text{gear}}m_{\text{TO}} \tag{A21}$$

$$m_{\text{misc}} = K_{\text{misc}}m_{\text{TO}} \tag{A22}$$

$$m_{\text{airframe}} = m_{\text{wing}} + m_{\text{HT}} + m_{\text{VT}} + m_{\text{fuse}} + m_{\text{gear}} + m_{\text{misc}} \tag{A23}$$

The airframe aerodynamic performance, characterized by the lift-to-drag ratio, is estimated based on the above vehicle surface areas and the wing aspect ratio, which is constrained by a specified max span, using a correlation suggested by Raymer [15].

$$S_{\text{wet}} = 2(S_{\text{wing}} + S_{\text{HT}} + S_{\text{VT}}) + S_{\text{fuse}} \tag{A24}$$

$$b \leq b_{\text{max}} \tag{A25}$$

$$\text{AR} = \frac{b^2}{S_{\text{wing}}} \tag{A26}$$

$$\frac{L}{D} = \frac{K_{(L/D)}\text{AR}}{2}\sqrt{\frac{S_{\text{wing}}}{S_{\text{wet}}}} \tag{A27}$$

Tables A3 and A4 list the design variables to be optimized and constant parameters related to the airframe sizing and aerodynamic efficiency.

Table A3: Aero-structure sizing design variables

Quantity	Dimension	Description
AR	-	wing aspect ratio
b	ft[A3]	wing span
c	ft	average wing chord
L/D	-	airframe lift-to-drag ratio
m_{fuse}	lb	fuselage mass
m_{gear}	lb	landing gear mass
m_{HT}	lb	horizontal tail mass
m_{misc}	lb	miscellaneous mass
m_{VT}	lb	vertical tail mass
m_{wing}	lb	wing mass
S_{fuse}	ft^2	fuselage wetted area
S_{HT}	ft^2	horizontal tail area
S_{VT}	ft^2	vertical tail area
S_{wet}	ft^2	airframe wetted area
S_{wing}	ft^2	wing area

Table A4: Aero-structure sizing constant parameters

Quantity	Value	Dimension	Description
c_{HT}	0.9 / 1.47[A4]	-	horizontal tail volume coefficient
c_{VT}	0.08 / 0.113	-	vertical tail volume coefficient
K_{fuse}	1.40 / 7.02	lb/ft^2	fuselage scaling factor
K_{gear} Kgear	0.057 / 0.053	-	landing gear scaling factor
K_{HT}	2 / 5.47	lb/ft^2	horizontal tail scaling factor
$K_{(L/D)}$	9.53 / 15.2	-	lift-to-drag ratio scaling factor
K_{misc} Kmisc	0.1 / 0.01	-	miscellaneous mass scaling factor
K_{VT}	2 / 6.50	lb/ft^2	vertical tail scaling factor
K_{wing}	0.61 / 1.12	lb/ft^3	wing scaling factor
b_{max}	65 / 90 / 118 / 200[A5]	ft	max wing span
d_{fuse}	6 / 11 / 12.5 / 20	ft	fuselage diameter
ℓ_{fuse}	52 / 105 / 130 / 242	ft	fuselage length
W/S	30 / 100 / 130 / 140	lb/ft^2	

[A3]Imperial units are used here to remain consistent with the suggested scaling coefficients [15]. GPkit has a built-in package to handle unit conversions, allowing specification of SI units everywhere else.

[A4]Values for thin haul and all other vehicle sizes, respectively.

[A5]Values for thin haul, regional, medium haul, and long haul, respectively.

A.3 Aero-Propulsive Performance

The aero-propulsive power requirements are defined using the one-dimensional version of the power balance method [2] described by Hall et al for BLI configurations [8]. The unpowered airframe drag is determined from takeoff mass and lift-to-drag ratio. The profile drag, related to the potential amount of boundary layer ingestion that can be achieved, is assumed to be a fixed fraction of the unpowered airframe drag. Nacelle drag contributions, scaled with total mass flow of all propulsors, is also included in the overall vehicle drag buildup.

$$D' = \frac{m_{\text{TO}}g}{L/D} \tag{A28}$$

$$D_p = \frac{D_p}{D}D' \tag{A29}$$

$$D_{\text{nace,e}} = r_{\text{nace}}\dot{m}_e^{0.7} \tag{A30}$$

$$D_{\text{nace,m}} = r_{\text{nace}}\dot{m}_m^{0.7} \tag{A31}$$

$$D'_{\text{tot}} = D' + D_{\text{nace,e}} + D_{\text{nace,m}} \tag{A32}$$

$$\tag{A33}$$

The power balance equation relates the propulsor mass flows, jet velocities, and amount of BLI to the total vehicle drag.

$$\dot{m}_e(V_{j,e} - V_\infty) + \dot{m}_m(V_{j,m} - V_\infty) = D'_{\text{tot}} - (f_{\text{BLI,e}} + f_{\text{BLI,m}})D_p \tag{A34}$$

$$f_{\text{BLI,e}} + f_{\text{BLI,m}} \leq 1 \tag{A35}$$

The mechanical flow power in each propulsive stream can then be determined as a function of the ingested profile dissipation and propuslor jet energy.

$$P_{K,m} = \frac{1}{2}\dot{m}_m(V_{j,m} - V_\infty)\big[2V_\infty + (V_{j,m} - V_\infty)\big] + f_{\text{BLI,m}}f_{\text{surf}}V_\infty D_p \tag{A36}$$

$$P_{K,e} = \frac{1}{2}\dot{m}_m(V_{j,e} - V_\infty)\big[2V_\infty + (V_{j,e} - V_\infty)\big] + f_{\text{BLI,e}}f_{\text{surf}}V_\infty D_p \tag{A37}$$

Tables A5 and A6 list the design variables to be optimized and constant parameters related to the aero-propulsive performance.

Table A5: Aero-propulsive performance design variables

Quantity	Dimension	Description
D'	N	unpowered airframe drag
$D_{\text{nace,e}}$	N	motor-driven propulsor nacelle drag
$D_{\text{nace,m}}$	N	turbine-driven propulsor nacelle drag
D'_{tot}	N	total (airframe + nacelle) drag
D_p	N	airframe profile drag
$\dot{m}_e$	kg/s	total motor-driven propulsor mass flow
$\dot{m}_m$	kg/s	total turbine-driven propulsor mass flow
$P_{K,e}$	W	total motor-driven propulsor mechanical flow power
$P_{K,m}$	W	total turbine-driven propulsor mechanical flow power
$(V_{j,e} - V_\infty)$	m/s	motor-driven propulsor jet velocity excess
$(V_{j,m} - V_\infty)$	m/s	turbine-driven propulsor jet velocity excess

Table A6: Aero-propulsive performance constant parameters

Quantity	Value	Dimension	Description
D_p/D	0.5	-	profile drag fraction
$f_{\text{BLI,e}}$	$[0,1]^{\text{A6}}$	-	motor-driven propulsor BLI fraction
$f_{\text{BLI,m}}$	$[0,1]$	-	turbine-driven propulsor BLI fraction
f_{surf}	0.9	-	airframe surface dissipation fraction
r_{nace}	51.9 / 33.0$^{\text{A7}}$	kg/(kg/s)$^{0.7}$	nacelle drag scaling factor

A.4 Electrified Propulsion System Architecture Model

A parametric description the general electrified propulsion system architecture shown in Fig. 4.3 allows the propulsion system sizing and performance to be modeled strictly as a function of propulsor powers and mass flows. Specification of the source and load electrification factors is sufficient to constrain the type of architecture (e.g., conventional, all-electric, turbo-electric, series or parallel hybrid-electric).

$$f_S = \frac{P_{\text{batt}}}{P_{\text{batt}} + P_{\text{core}}} \tag{A38}$$

$$f_L = \frac{P_{K,e}}{P_{K,e} + P_{K,m}} \tag{A39}$$

The propulsion system model consists of gas generator cores, ducted fans, electric motors, electric motors, rectifiers, inverters, batteries, and a thermal management system. The masses of the mechanical and electrical components are sized based on the power of each component using the scaling parameters listed in Tab. A8.

$$\dot{m}_{\text{core}} = \frac{P_{\text{core}}}{P_{\text{sp}}} \tag{A40}$$

$$m_{\text{core}} = K_{\text{core}} \dot{m}_{\text{core}}^{1.2} \tag{A41}$$

$$m_{\text{gen/mot}} = \left(\frac{P}{m}\right)_{\text{gen/mot}}^{-1} P_{\text{gen/mot}} \tag{A42}$$

$$m_{\text{rect/inv}} = \left(\frac{P}{m}\right)_{\text{rect/inv}}^{-1} P_{\text{rect/inv}} \tag{A43}$$

$$m_{\text{m.fan}} = K_{\text{fan}} \left(\frac{\dot{m}_m}{N_{\text{cores}}}\right)^{1.2} \tag{A44}$$

$$m_{\text{m.nace}} = K_{\text{nace}} \frac{\dot{m}_m}{N_{\text{cores}}} \tag{A45}$$

$$m_{\text{inv}} = \left(\frac{P}{m}\right)_{\text{inv}}^{-1} P_{\text{inv}} \tag{A46}$$

$$m_{\text{mot}} = \left(\frac{P}{m}\right)_{\text{mot}}^{-1} P_{\text{mot}} \tag{A47}$$

$$m_{\text{e.fan}} = K_{\text{fan}} \left(\frac{\dot{m}_e}{N_{\text{e.fan}}}\right)^{1.2} \tag{A48}$$

[A6]BLI fraction is treated as a constant in the current model formulation; see Section 5.1.6 for discussion of performance trends with variation in f_{BLI}.

[A7]Values for individual podded nacelles and arrays of distributed propulsors, respectively.

$$m_{\text{e.nace}} = K_{\text{nace}} \frac{\dot{m}_e}{N_{\text{e.fan}}} \tag{A49}$$

$$m_{\text{TMS}} = \left(\frac{P}{m}\right)_{\text{TMS}}^{-1} Q \tag{A50}$$

$$m_{\text{prop}} = N_{\text{cores}}(m_{\text{core}} + m_{\text{gen/mot}} + m_{\text{rect/inv}} + m_{\text{m.fan}} + m_{\text{m.nace}}) \\ + N_{\text{e.fan}}(m_{\text{inv}} + m_{\text{mot}} + m_{\text{e.fan}} + m_{\text{e.nace}}) + m_{\text{TMS}} \tag{A51}$$

The heat rejected from the electrical components, which ultimately sizes the thermal management system, is determined based on the power of each component and the efficiencies listed in Tab. A8.

$$Q_{\text{batt}} = P_{\text{batt}}(1 - \eta_{\text{batt}}) \tag{A52}$$

$$Q_{\text{gen/mot}} = P_{\text{gen/mot}}(1 - \eta_{\text{gen/mot}}) \tag{A53}$$

$$Q_{\text{inv}} = P_{\text{inv}}(1 - \eta_{\text{inv}}) \tag{A54}$$

$$Q_{\text{mot}} = P_{\text{mot}}(1 - \eta_{\text{mot}}) \tag{A55}$$

$$Q_{\text{rect/inv}} = P_{\text{rect/inv}}(1 - \eta_{\text{rect/inv}}) \tag{A56}$$

$$Q = Q_{\text{batt}} + Q_{\text{gen/mot}} + Q_{\text{inv}} + Q_{\text{mot}} + Q_{\text{rect/inv}} \tag{A57}$$

A mechanical and electrical system-level power balance relates the propulsor mechanical flow powers to the fuel consumption and battery power. It is assumed the efficiencies of all electric machines and all power electronics are equal.

$$\eta_{\text{gen/mot}} = \eta_{\text{mot}} = \eta_{\text{EM}} \tag{A58}$$

$$\eta_{\text{inv/rect}} = \eta_{\text{rect}} = \eta_{\text{PE}} \tag{A59}$$

Under these assumptions, the propulsion system can be considered a series architecture if the following inequality holds,

$$f_L(1 - f_S) > \eta_{\text{PE}} \eta_{\text{EM}} f_S(1 - f_L), \tag{A60}$$

otherwise the propulsion system may be considered a parallel architecture. Turbo-electric architectures may be considered a subset of series architectures, and conventional and all-electric architectures may be treated as either, where zero power in the mechanical and electric propulsors, respectively, yields the same power balance for both architectures.

A.4.1 Series Architecture Power Balance

For series architectures, power is taken off the gas generator shaft by an electric generator and distributed to the electric propulsor system.

$$N_{\text{cores}} P_{\text{core}} = \dot{m}_{\text{fuel}} h_{\text{fuel}} \eta_{\text{th}} \tag{A61}$$

$$P_{\text{gen/mot}} = P_{\text{core}} - P_{\text{m.fan}} \tag{A62}$$

$$P_{K,m} = N_{\text{cores}} P_{\text{m.fan}} \eta_{\text{fan}} \tag{A63}$$

$$P_{\text{rect/inv}} = P_{\text{gen/mot}} - Q_{\text{gen/mot}} \tag{A64}$$

$$N_{\text{e.fan}} P_{\text{inv}} = N_{\text{cores}}(P_{\text{rect/inv}} - Q_{\text{rect/inv}}) + P_{\text{batt}} \tag{A65}$$

$$P_{\text{mot}} = P_{\text{inv}} - Q_{\text{inv}} \tag{A66}$$

$$P_{\text{e.fan}} = P_{\text{mot}} - Q_{\text{mot}} \tag{A67}$$

$$P_{K,e} = N_{\text{e.fan}} P_{\text{e.fan}} \eta_{\text{fan}} \tag{A68}$$

A.4.2 Parallel Architecture Power Balance

For parallel architectures, battery power is added to the gas generator shaft through an electric motor.

$$N_{\text{cores}}P_{\text{core}} = \dot{m}_{\text{fuel}}h_{\text{fuel}}\eta_{\text{th}} \tag{A69}$$

$$P_{\text{m.fan}} = P_{\text{core}} + P_{\text{gen/mot}} \tag{A70}$$

$$P_{K,m} = N_{\text{cores}}P_{\text{m.fan}}\eta_{\text{fan}} \tag{A71}$$

$$P_{\text{gen/mot}} = P_{\text{rect/inv}} - Q_{\text{rect/inv}} \tag{A72}$$

$$P_{\text{batt}} = N_{\text{cores}}P_{\text{rect/inv}} + N_{\text{e.fan}}P_{\text{inv}} \tag{A73}$$

$$P_{\text{mot}} = P_{\text{inv}} - Q_{\text{inv}} \tag{A74}$$

$$P_{\text{e.fan}} = P_{\text{mot}} - Q_{\text{mot}} \tag{A75}$$

$$P_{K,e} = N_{\text{e.fan}}P_{\text{e.fan}}\eta_{\text{fan}} \tag{A76}$$

Tables A7 and A8 list the design variables to be optimized and constant parameters related to the propulsion system sizing and performance.

Table A7: Electrified propulsion system architecture design variables

Quantity	Dimension	Description
$m_{\text{e.fan}}$	kg	electric fan mass
$m_{\text{e.nace}}$	kg	electric fan nacelle mass
m_{core}	kg	gas generator core mass
$m_{\text{gen/mot}}$	kg	generator/motor mass
m_{inv}	kg	inverter mass
$m_{\text{m.fan}}$	kg	mechanical fan mass
$m_{\text{m.nace}}$	kg	mechanical fan nacelle mass
m_{mot}	kg	motor mass
$m_{\text{rect/inv}}$	kg	rectifier/inverter mass
m_{TMS}	kg	thermal management system mass
$\dot{m}_{\text{core}}$	kg/s	core mass flow
$\dot{m}_{\text{fuel}}$	kg/s	fuel flow rate
$N_{\text{e.fan}}$[A8]	-	number of electric fans
N_{cores}	-	number of gas generator cores
P_{batt}	W	battery power
P_{core}	W	gas generator core power
$P_{\text{e.fan}}$	W	electric fan shaft power
$P_{\text{gen/mot}}$	W	generator/motor power
P_{inv}	W	inverter power
$P_{\text{m.fan}}$	W	mechanical fan shaft power
P_{mot}	W	motor power
$P_{\text{rect/inv}}$	W	rectifier/inverter power
Q	W	total thermal dissipation
Q_{batt}	W	battery thermal dissipation
Q_{gen}	W	generator/motor thermal dissipation
Q_{inv}	W	inverter thermal dissipation
Q_{mot}	W	motor thermal dissipation
$Q_{\text{rect/inv}}$	W	rectifier/inverter thermal dissipation

---

[A8]Optimization of the propulsion configuration as in Section 5.1 can be carried out treating the number of fans and gas generators as continuous variables. Optimal designs can then be assessed by rounding to the integer values that yield the best performance.

Table A8: Electrified propulsion system architecture constant parameters

Quantity	Value	Dimension	Description
f_L	[0,1]	-	load electrification factor
f_S	[0,1]	-	source electrification factor
h_{fuel}	43	MJ/kg	fuel heating value
K_{core}	45.6	kg/(kg/s)$^{1.2}$	core mass scaling factor
K_{fan}	1.30	kg/(kg/s)$^{1.2}$	fan mass scaling factor
K_{nace}	4.56	kg/(kg/s)	nacelle scaling factor
P_{sp}	400	kJ/kg	core specific power
$(P/m)_{\text{TMS}}$	8	hp/lb	thermal management system specific power
η_{fan}	0.9	-	fan efficiency
η_{th}	0.5	-	core thermal efficiency
$(P/m)_{\text{gen/mot}}$	2 / 9 / 16[A9]	W/kg	generator/motor specific power
$(P/m)_{\text{inv}}$	2.2 / 9 / 19	W/kg	inverter specific power
$(P/m)_{\text{mot}}$	2 / 9 / 16	W/kg	motor specific power
$(P/m)_{\text{rect/inv}}$	2.2 / 9 / 19	W/kg	rectifier/inverter specific power
$\eta_{\text{gen/mot}}$	0.95 / 0.98 / 0.99	-	generator/motor efficiency
η_{inv}	0.95 / 0.98 / 0.99	-	inverter efficiency
$\eta_{\text{rect/inv}}$	0.95 / 0.98 / 0.99	-	rectifier/inverter efficiency
η_{mot}	0.95 / 0.98 / 0.99	-	motor efficiency

[A9]Values for current state of the art, conservative 2035, and optimistic 2035 technology assumptions, respectively, defined in Section 3.

Appendix B

Detailed Electric Component Models

This section describes the detailed electric component models used in the analysis in Section 6.1. Table B1 lists the components, and the following subsections present the model formulations and the variables, parameters, and constraints used in their GPKit implementation.

B.1 Cable Model

The cable model consists of a single cylindrical conductor with an outer insulation layer. The insulation of the cable must be sufficiently thick to prevent dielectric breakdown, and the conductor is sized based on acceptable voltage drop and hence cable ohmic heating losses. It is assumed that the cable conductor consists of stranded (Litz) wire for mitigating the skin and proximity effects - loss mechanisms that arise from time-varying signals. These losses are not modeled, but the impact of Litz wire on the mass and resistance of the cable is captured via a packing factor. This level of detail captures trade-offs in delivering propulsion power at specific voltage and current levels.

B.1.1 Cable Sizing

The cable has an inner radius a and outer radius b as in Fig. B1. The conductor Litz wire has a packing factor k_{pf} which represents the percent of the conductor area occupied by the conductive material. The

Table B1: Electric component models

Component	Sizing Model	Performance Model
Cable	voltage-current sizing	resistor circuit
Electrical Machine	voltage-current and torque-speed sizing	single-phase equivalent circuit
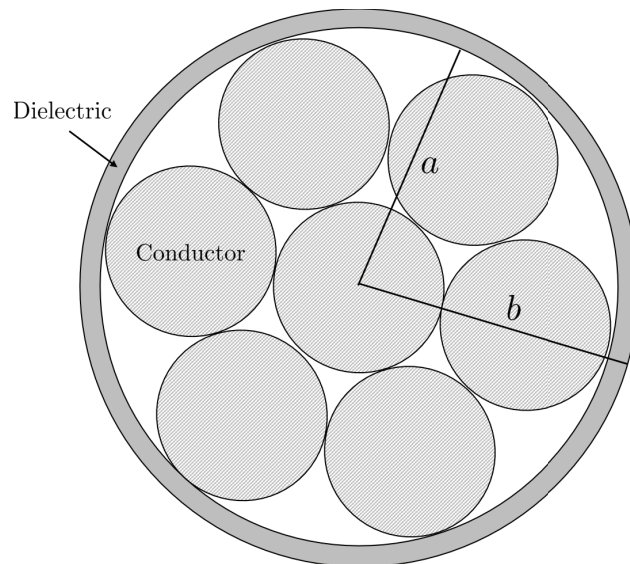
Figure B1: Cable geometry.

conductor area, A_c, is

$$A_c = \pi a^2 k_{\text{pf}} \tag{B1}$$

and the dielectric area, A_{di} is

$$\begin{aligned} A_{\text{di}} &= \pi \left(b^2 - a^2 \right) \\ &= \pi \left(b + a \right) t_{\text{di}} \end{aligned} \tag{B2}$$

where $t_{\text{di}} = b - a$ is the thickness of the dielectric. Assuming the cable has a length ℓ, its mass is

$$m = A_c \ell d_c + A_{\text{di}} \ell d_{\text{di}} \tag{B3}$$

where d_c and d_{di} are the densities of the conductor and insulation, respectively.

Dielectric breakdown occurs when the electric field in the cable insulation exceeds E_{max}, a dielectric material property. Assuming the insulator thickness is small compared to the conductor radius, a parallel-plate approximation is used for the electric field generated from the voltage difference between the conductor and cable exterior. The maximum electric field strength is

$$E_{\text{max}} = \frac{V_{\text{max}}}{t_{\text{di}}} \tag{B4}$$

where V_{max} is the maximum voltage in the cable relative to ground.

The conductor has a uniform cross-section, with resistance,

$$R = \rho \frac{\ell}{A_c}. \tag{B5}$$

The maximum cable power is,

$$P_{\text{max}} = V_{\text{max}} I_{\text{max}}. \tag{B6}$$

The variables used in this formulation are given in Table B2. The cable model is general in that different conductor and insulator materials can be used to examine material property trade-offs. The constant parameters used during the studies in Section 6.1 are given in Table B3. The conductor parameters correspond to an aluminum alloy, and the dielectric to polyimide tapes. The packing factor is derived assuming a hexagonal packing shape.

Table B2: Cable sizing design variables

Quantity	Dimension	Description
A_c	m^2	conductor area
A_{di}	m^2	dielectric area
a	m	inner insulation radius
b	m	outer insulation radius
I_{max}	A	max current
ℓ	m	cable length
m_{di}	kg	dielectric mass
m_{c}	kg	conductor mass
m	kg	total cable mass
P_{max}	W	maximum cable power
R	Ω	cable resistance
t_{di}	m	dielectric thickness
V_{max}	V	max cable voltage

Table B3: Cable sizing constant parameters

Quantity	Value	Dimension	Description
d_c	2.83e6	kg/m^3	conductor volumetric mass density
d_{di}	1.70e6	kg/m^3	dielectric volumetric mass density
E_{max}	1.00e7	V/m	dielectric max field strength
k_{pf}	0.91	-	Litz wire packing factor
ρ	2.65e-8	Ω m	conductor resistivity

B.1.2 Cable Performance

The cable performance is described by its resistance and terminal voltages, as in Fig. B2. From Kirchoff's
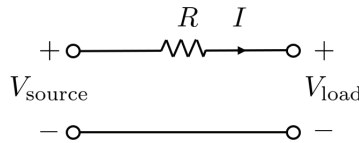
Figure B2: Cable appears as a resistor when connected to other components

voltage law,

$$V_{\mathrm{load}} + IR_{\mathrm{cable}} = V_{\mathrm{source}}. \tag{B7}$$

The ohmic heating losses are,

$$Q = I^2 R, \tag{B8}$$

and the load and source powers are,

$$P_{\mathrm{load}} = IV_{\mathrm{load}}, \tag{B9}$$

$$P_{\mathrm{source}} = IV_{\mathrm{source}}. \tag{B10}$$

The cable efficiency is,

$$\eta = \frac{P_{\mathrm{load}}}{P_{\mathrm{source}}} = 1 - \frac{P_{\mathrm{load}}}{P_{\mathrm{load}} + I^2 R}. \tag{B11}$$

Equation (B11) illustrates that, for a fixed load power, a low current or low resistance tend to maximize the cable efficiency. Table B4 lists the variables used for cable performance.

Table B4: Cable performance design variables

Quantity	Dimension	Description
η	-	efficiency
I	A	RMS current
P_{load}	W	load power
P_{source}	W	source power
Q	W	Ohmic losses
V_{load}	V	load voltage
V_{source}	V	source voltage

B.2 Electrical Machine Model

In Section 6.1, the electrical machine is a permanent magnet synchronous machine. The magnets are mounted radially on the rotor and the windings are in slots on the stator. It is assumed to have three phases and three slots per pole. The machine can either have the rotor interior to (inner rotor) or exterior to (outer rotor) the stator. Both generator and motor models were developed.

For a fixed geometry, the maximum machine output power is limited by electrical loading (thermal and breakdown issues), magnetic saturation, tip speed limitations, and electrical frequency/core loss considerations. The following sections describe the analysis used to capture these fundamental limitations.

B.2.1 Electrical Machine Sizing

This section details the sizing of an inner rotor electrical machine. The same approach was used for the outer rotor geometry available in the GPKit code, but for brevity is not included here. Figure. B3 shows a flattened cross-section of the inner rotor machine and the corresponding geometric variable definitions.

The total motor mass consists of the stator back iron mass, m_{sbi}, stator teeth mass, m_{teeth}, windings mass, m_{wind}, magnets mass, m_{magnet}, and rotor back iron mass, m_{rbi}. For an axial motor length ℓ, p pole pairs, and steel, magnet, and winding densities (d_{steel}, d_{magnet}, and d_{wind}, respectively), the motor mass m_{motor} is

$$
\begin{aligned}
m_{\text{sbi}} &= \pi \left(R_6^2 - R_5^2 \right) \ell d_{\text{stator}} \\
m_{\text{teeth}} &= A_{\text{teeth}} \ell d_{\text{stator}} \\
m_{\text{wind}} &= k_{\text{pf}} A_{\text{wind}} \left(\ell + 2L_{\text{et}} \right) d_{\text{wind}} \\
m_{\text{magnet}} &= \pi \left(R_3^2 - R_2^2 \right) \ell d_{\text{magnet}} \\
m_{\text{rbi}} &= \pi \left(R_2^2 - R_1^2 \right) \ell d_{\text{rotor}} \\
m_{\text{motor}} &= m_{\text{sbi}} + m_{\text{teeth}} + m_{\text{wind}} + m_{\text{magnet}} + m_{\text{rbi}}
\end{aligned}
\tag{B12}
$$
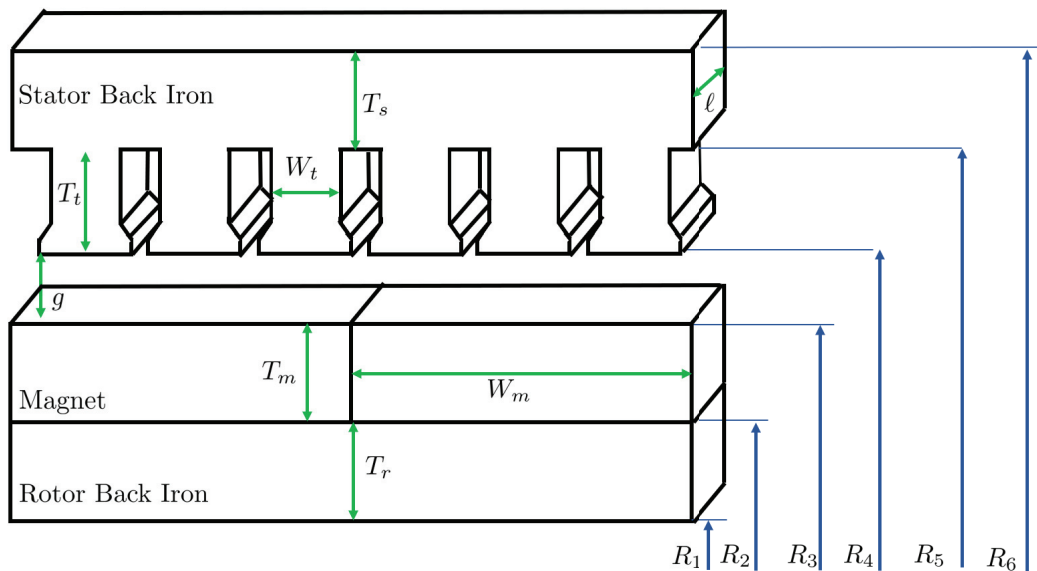
Figure B3: Cutout of inner rotor geometry showing dimensions.

where L_{et} is the winding end turn length, and

$$A_{teeth} = 6p T_t W_t,$$
$$A_{teeth} + A_{wind} = \pi \left(R_5^2 - R_4^2 \right). \tag{B13}$$

Several of the sizing variables are shown in Fig. B3.

The end turns of the motor, L_{et}, are modeled assuming a triangular pattern [20]. The length of these end turns is

$$L_{et} = \frac{\pi}{2p} R_4 \frac{\lambda}{\sqrt{1 - \lambda^2}}, \tag{B14}$$

where λ is the slot fraction

$$\lambda = \frac{A_{wind}}{A_{wind} + A_{teeth}}. \tag{B15}$$

The resistance of one slot of windings, R_{slot}, is

$$R_{slot} = \rho \frac{\ell + 2L_{et}}{k_{pf} A_{slot}}. \tag{B16}$$

The total resistance of all three phases, R_{tot}, is

$$R_{tot} = 6p R_{slot}, \tag{B17}$$

and the per phase resistance is

$$R_{ph} = \frac{1}{3} R_{tot}. \tag{B18}$$

The slot area limits the number of windings, N, and area of the windings, A_{slot}, that can be used. Specifically,

$$A_{slot} = \frac{A_{wind}}{6p}, \tag{B19}$$

where

$$A_{wind} = \frac{6p N A_{wire}}{k_{pf}}. \tag{B20}$$

The minimum number of windings is two. Increasing the number of windings decreases the size of the wire for a fixed winding area. The maximum winding is given by

$$A_{wire} = \frac{\eta_{cond} A_{wind}}{6p N} \geq A_{wire,min}, \tag{B21}$$

where $A_{wire,min}$ is typically the area of a 20 AWG wire.

A summary of the sizing variables is shown in Table B5. For the studies in this report, the motor is assumed to use Neodymium magnets and Alnico 50 steel. Table B6 gives their sizing parameters.

B.2.2 Electrical Machine Performance

The electrical machine performance model relates the input voltage and current to the output torque and angular speed. The torque is

$$\tau = (4p) \tilde{B}_{gap} N I_{rms} \ell R_3 \tag{B22}$$

The associated magnetic shear stress is

$$\sigma = \frac{\tau}{2\pi R_3^2 \ell} \tag{B23}$$

Table B5: Electrical machine sizing design variables

Quantity	Dimension	Description
A_{slot}	m^2	single slot area
A_{teeth}	m^2	stator teeth area
A_{wire}	m^2	single wire area
A_{wind}	m^2	total winding area
ℓ	m	axial length
λ	-	slot fraction
L_{et}	m	end turn length
m_{rbi}	kg	rotor back iron mass
m_{magnet}	kg	magnet mass
m_{sbi}	kg	stator back iron mass
m_{teeth}	kg	teeth mass
$m_{\text{mainwindings}}$	kg	axial windings mass
$m_{\text{endwindings}}$	kg	end windings mass
m	kg	total PM machine mass
N	-	number of winding turns
p	-	number of pole pairs
R_{ph}	V/A	phase resistance
R_{slot}	V/A	slot resistance
R_{tot}	V/A	total resistance
R_1	m	rotor back iron inner radius
R_2	m	rotor back iron outer radius
R_3	m	magnet outer radius
R_4	m	teeth inner radius
R_5	m	stator back iron inner radius
R_6	m	stator back iron outer radius
T_m	m	magnet thickness
T_r	m	rotor back iron thickness
T_s	m	stator back iron thickness
T_t	m	stator tooth thickness
U_{max}	V	max tip speed
W_m	m	magnet width
W_t	m	tooth width

The shear stress is limited by saturation in the teeth [21]. The magnetic flux in the tooth is the magnitude of the vector sum of the flux due to the magnets and the flux due to the armature reaction,

$$\sqrt{\left(\frac{\tilde{B}_{\text{gap}}}{\lambda}\right)^2 + (\mu_0 J_{\text{slot}} T_t)^2} = B_{\text{teeth}} \leq B_{\text{sat}} \tag{B24}$$

where

$$J_{\text{slot}} = \frac{4pNI_{\text{rms}}}{(1-\lambda)\pi R_4 T_t} \tag{B25}$$

The airgap flux can be found from line integral of the H-field around the contour in Figure B4.

$$2H_{\text{m}} T_{\text{m}} + 2H_{\text{gap}} g + (2T_t + W_{\text{out}} + W_{\text{in}}) H_{\text{steel}} = 0. \tag{B26}$$

Table B6: Electrical machine sizing constant parameters

Quantity	Value	Dimension	Description
$A_{\text{wire,min}}$	0.518	mm^2	minimum wire area
B_{sat}	2.4	N/m/A	saturation flux
d_{cond}	8930	kg/m^3	density of conductor
d_{stator}	8200	kg/m^3	density of stator
d_{rotor}	8200	kg/m^3	density of rotor
d_{magnet}	7501	kg/m^3	density of magnet
k_{pf}	0.35	-	packing factor of conductor
g	400e-6	m	airgap thickness
M	8.6e5	A/m	magnetization constant
ρ	1.67e-8	Vm/A	resistivity
μ_0	4πe-7	Vs/A/m	vacuum permittivity
μ_{sat}	120 4 πe-7	Vs/A/m	steel saturation permittivity
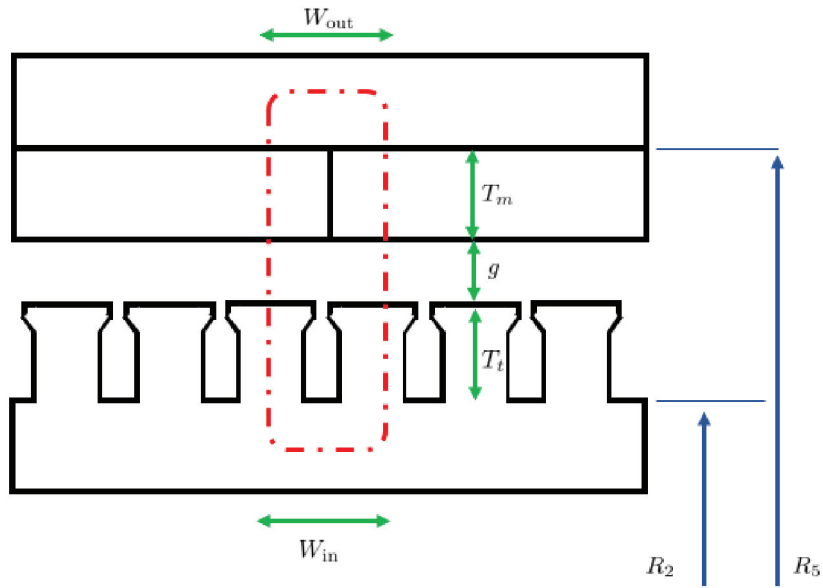
Figure B4: Ampere law contour for airgap flux estimation.

Substituting in Eqn. (B26)

$$H_{\text{m}} = \frac{B_{\text{gap}}}{\mu_0} - M \tag{B27}$$

$$H_{\text{gap}} = \frac{B_{\text{gap}}}{\mu_0} \tag{B28}$$

$$H_{\text{steel}} = \frac{B_{\text{steel}}}{\mu_s} \tag{B29}$$

B_{gap} is found as

$$B_{\text{gap}} = \frac{\mu_0 M T_m}{T_m + g} - \frac{2T_t + W_{\text{out}} + W_{\text{in}}}{2T_m + 2g} \mu_0 H_{\text{steel}}, \tag{B30}$$

where

$$W_{\text{in}} = \frac{\pi (R_1 + R_2)}{6p}, \tag{B31}$$

$$W_{\text{out}} = \frac{\pi (R_5 + R_6)}{6p}. \tag{B32}$$

The airgap size and pole count must be sufficiently small for the magnet flux to pass across the airgap to the stator teeth rather than leak from magnet-to-magnet. To capture this effect, the magnet-to-magnet leakage flux can be modeled as a circular-arc [27]. From this assumption, the flux that passes across the gap while accounting for leakage, $\tilde{B}_{\text{gap}}$, is

$$\tilde{B}_{\text{gap}} = B_{\text{gap}} \left(1 - \frac{4gp}{\pi^2 R_3} \right). \tag{B33}$$

The angular speed and voltage are related via a power balance between ohmic heating, eddy current, and hysteresis losses.

$$P_{\text{in}} = \tau \omega - Q_{\text{ohmic}} - Q_{\text{eddy}} - Q_{\text{hysteresis}}. \tag{B34}$$

Assuming the motor is controlled such that two phases are active at any given time, the ohmic losses are

$$Q_{\text{ohmic}} = I^2 (2R_{\text{wind}}). \tag{B35}$$

The electrical machine model is completed by characterizing the eddy and hysteresis losses:

$$Q_{\text{eddy}} = m_{\text{sbi}} \left(k_e f^2 B_{\text{sbi}}^2 \right) + m_{\text{teeth}} \left(k_e f^2 B_{\text{teeth}}^2 \right), \tag{B36}$$

$$Q_{\text{hyst}} = m_{\text{sbi}} \left(k_h f B_{\text{sbi}}^\alpha \right) + m_{\text{teeth}} \left(k_e f B_{\text{teeth}}^\alpha \right), \tag{B37}$$

where k_e and k_h are eddy current and hysteresis loss coefficients for a particular material, respectively, f is electrical frequency, B_{sbi} is the stator back-iron flux density, B_{teeth} is the stator teeth flux density, and α is an exponential fit coefficient.

Table B7: Electrical machine performance design variables

Quantity	Dimension	Description
B_{gap}	N/m/A	gap flux
$\tilde{B}_{\mathrm{gap}}$	N/m/A	derated gap flux
B_{rotor}	N/m/A	rotor back iron flux
B_{stator}	N/m/A	stator back iron flux
B_{teeth}	N/m/A	teeth flux
η	-	efficiency
f	Hz	electrical frequency
I_{rms}	A	rms current
J_{slot}	A/mm^2	slot current density
J_{wire}	A/mm^2	wire current density
P_{load}	W	load power
P_{source}	W	source power
Q_{ohmic}	W	Ohmic losses
Q_{core}	W	core losses
τ	Nm	torque
μ_r	Vs/A/m	rotor back iron permittivity
μ_s	Vs/A/m	stator back iron permittivity
μ_t	Vs/A/m	teeth permittivity
V_{rms}	V	rms voltage
ω	rad/s	angular speed

Table B8: Electrical machine constant parameters

Quantity	Value	Dimension	Description
k_e	32.183e-6	W/lb/Hz	eddy current loss coefficient
k_h	10.664e-3	W/lb/Hz	hysteresis loss coefficient

Appendix C

Aircraft Conceptual Design Model

This section describes the details of airframe component sizing and performance models used in the aircraft conceptual design analysis presented in Section 6.2.

C.1 Free Stream State Model

Free stream conditions fluid conditions are calculated as a function of altitude using an SP atmosphere model. All calculations were carried out for an altitude of of 37,000 ft, and the variables required for the airframe drag buildup, listed in Tab. C1, can be assumed constant, with the model formulation providing sensitivity of the vehicle performance to the input constant altitude.

Table C1: Flight state variables

Quantity	Value	Dimension	Description
V_∞	423	kt	cruise free stream velocity
ν_∞	4.02×10^{-5}	kg/m/s	free stream kinematic viscosity
ρ_∞	0.3511	kg/m^3	free stream density

C.2 Fuselage Model

C.2.1 Fuselage Sizing

The fuselage mass is calculated using the buildup of Torenbeek [24], which includes contributions proportional to fuselage shell and floor structural weight and a scaling factor to account for composite weight saving.

$$S_{\text{wet}} = \pi d_{\text{fuse}} \ell_{\text{fuse}} \tag{C1}$$

$$m_{\text{fuse}} g = f_{\text{comp}} \left[C_{\text{shell}} d_{\text{fuse}}^2 (\ell_{\text{fuse}} + \ell_{\text{ref}}) + \Omega_{\text{fl}} N_z^{0.5} d_{\text{fuse}} \ell_{\text{fuse}} \right] \tag{C2}$$

A fuselage body form factor, used in the fuselage performance model below, is defined as a function of the fuselage fineness ratio.

$$\text{FR} = \frac{\ell_{\text{fuse}}}{d_{\text{fuse}}} \tag{C3}$$

$$K = 1.4509 \cdot \text{FR}^{-0.255} \tag{C4}$$

Tables C2 and C3 list the variables to be optimized and constant parameters related to the fuselage sizing.

[C1]Values for conventional and composite fuselage design, respectively.

Table C2: Fuselage sizing design variables

Quantity	Dimension	Description
d_{fuse}	ft	fuselage maximum diameter
FR	-	fuselage fineness ratio
K	-	fuselage body form factor
ℓ_{fuse}	ft	fuselage length
m_{fuse}	lb	fuselage mass
N_z	-	ultimate load factor
S_{ref}	ft^2	wing reference area
S_{wet}	ft^2	fuselage wetted area

Table C3: Fuselage sizing constant parameters

Quantity	Value	Dimension	Description
C_{shell}	60	N/m^3	fuselage shell density
f_{comp}	1.0 / 0.9[C1]	-	composite mass scaling factor
ℓ_{ref}	1.5	m	reference length
Ω_{fl}	160	N/m^2	non-shell mass scaling factor

C.2.2 Fuselage Performance

The fuselage profile drag is modeled using a Reynolds number scaling of turbulent skin friction and the form factor scaling of Schaufele [25].

$$\text{Re}_\ell = \frac{V_\infty \ell_{\text{fuse}}}{\nu_\infty} \tag{C5}$$

$$C_f = \frac{0.74}{\text{Re}_\ell^{0.2}} \tag{C6}$$

$$C_{D_p,\text{fuse}} = C_f \frac{K S_{\text{wet}}}{S_{\text{ref}}} \tag{C7}$$

$$D_{p,\text{fuse}} = \frac{1}{2}\rho_\infty V_\infty^2 S_{\text{ref}} f_{\text{excr,fuse}} C_{D_p,\text{fuse}} \tag{C8}$$

$$D_{\text{fuse}} = D_{p,\text{fuse}} \tag{C9}$$

Tables C4 and C5 list the variables to be optimized and constant parameters related to the fuselage performance.

Table C4: Fuselage performance design variables

Quantity	Dimension	Description
$C_{D_p,\text{fuse}}$	-	fuselage profile drag coefficient
C_f	-	skin friction coefficient
$D_{p,\text{fuse}}$	lbf	fuselage profile drag
D_{fuse}	lbf	fuselage total drag
Re_ℓ	-	fuselage length-reference Reynolds number

Table C5: Fuselage performance constant parameters

Quantity	Value	Dimension	Description
$f_{\text{excr,fuse}}$	1.00	-	fuselage excrescence drag factor

C.3 Wing Model

C.3.1 Wing Sizing

The wing mass is modeled as function of maximum lift, wing area, aspect ratio, thickness-to-chord ratio, taper ratio, sweep, and approximate control surface area using the statistical correlation of Raymer [15].

$$S_{\text{CSW}} = 0.5 S_{\text{ref}} \tag{C10}$$

$$\text{AR} = \frac{b^2}{S_{\text{ref}}} \tag{C11}$$

$$m_{\text{wing}} g = f_{\text{comp}} \left[F_w L_{\text{max}}^{0.557} S_{\text{ref}}^{0.649} \text{AR}^{0.5} (t/c)_{\text{root}}^{-0.4} (\lambda + 1)^{0.1} (\cos \Lambda)^{-0.1} S_{\text{CSW}}^{0.1} \right] \tag{C12}$$

$$b_{\text{max}} \geq b \tag{C13}$$

Tables C6 and C7 list the variables to be optimized and constant parameters related to wing sizing.

Table C6: Wing sizing design variables

Quantity	Dimension	Description
AR	-	wing aspect ratio
b	ft	wing span
b_{max}	ft	max wing span
$\bar{c}$	ft	mean aerodynamic chord
$\cos \Lambda$	-	cosine of wing sweep angle
L_{max}	lbf	max wing lift
m_{wing}	lb	wing mass
S_{CSW}	ft^2	control surface area
S_{ref}	ft^2	wing reference area
$\lambda + 1$	-	taper ratio plus one

Table C7: Wing sizing constant parameters

Quantity	Value	Dimension	Description
F_w	0.00612	lbf$^{0.443}$/(ft^2)$^{0.749}$	wing mass factor
f_{comp}	-	1.0 / 0.875[C2]	composite mass scaling factor
$(t/c)_{\text{root}}$	0.127	-	airfoil thickness ratio

[C2]Values for conventional and composite wing design, respectively.

C.3.2 Wing Performance

The wing induced drag is calculated based on the wing lift coefficient using the typical span loading efficient relation.

$$L_{\text{wing}} = \frac{1}{2}\rho_\infty V_\infty^2 S_{\text{ref}} C_{L,w} \tag{C14}$$

$$C_{L,w} \leq C_{L,\max} \tag{C15}$$

$$L_{\text{wing}} \leq L_{\max} \tag{C16}$$

$$C_{D_i,w} = \frac{C_{L,w}^2}{\pi e \text{AR}} \tag{C17}$$

$$D_{i,w} = \frac{1}{2}\rho_\infty V_\infty^2 S_{\text{ref}} C_{D_i,w} \tag{C18}$$

The wing profile drag is calculated as a function of wing lift, Reynolds number, Mach number, sweep, and thickness-to-drag ratio using a GP fit of TASOPT wing profile drag data [17].

$$\text{Re}_c = \frac{V_\infty \bar{c}}{\nu_\infty} \tag{C19}$$

$$
\begin{aligned}
1.6515 C_{D_p,w} = {} & 1.61418 \left(\frac{\text{Re}_c}{1000}\right)^{-0.550434} (t/c)_{\text{root}}^{1.29151} (M_\infty \cos\Lambda)^{3.03609} C_{L,w}^{1.77743} \\
& + 0.0466407 \left(\frac{\text{Re}_c}{1000}\right)^{-0.389048} (t/c)_{\text{root}}^{0.784123} (M_\infty \cos\Lambda)^{-0.340157} C_{L,w}^{0.950763} \\
& + 190.811 \left(\frac{\text{Re}_c}{1000}\right)^{-0.218621} (t/c)_{\text{root}}^{3.94654} (M_\infty \cos\Lambda)^{19.2524} C_{L,w}^{1.15233} \\
& + 2.82283(10^{-12}) \left(\frac{\text{Re}_c}{1000}\right)^{1.18147} (t/c)_{\text{root}}^{-1.75664} (M_\infty \cos\Lambda)^{0.10563} C_{L,w}^{-1.44114}
\end{aligned} \tag{C20}
$$

$$D_{p,w} = \frac{1}{2}\rho_\infty V_\infty^2 S_{\text{ref}} f_{\text{excr,wing}} C_{D_p,w} \tag{C21}$$

$$D_{\text{wing}} = D_{p,w} + D_{i,w} \tag{C22}$$

Tables C8 and C9 list the variables to be optimized and constant parameters related to wing performance.

Table C8: Wing performance design variables

Quantity	Dimension	Description
$C_{D_i,w}$	-	wing induced drag coefficient
$C_{D_p,w}$	-	wing profile drag coefficient
$C_{L,w}$	-	wing lift coefficient
$D_{i,w}$	lbf	wing induced drag
$D_{p,w}$	lbf	wing profile drag
D_{wing}	lbf	wing total drag
L_{wing}	lbf	wing total lift force
Re_c	-	chord-referenced Reynolds number

Table C9: Wing performance constant parameters

Quantity	Value	Dimension	Description
$C_{L,\text{max}}$	1.85	-	max clean wing lift coefficient
e	0.9	-	wing Oswald efficiency
$f_{\text{excr,wing}}$	1.00	-	wing excrescence drag factor

C.4 Horizontal Tail Model

C.4.1 Horizontal Tail Sizing

The horizontal tail mass is calculated using the approximate tail area sizing and mass scaling described by Torenbeek [24].

$$S_h \ell_h \text{AR} = 2 S_h \ell_h + 0.2 (S_{\text{ref}} \bar{c} + 2 d_{\text{fuse}}^2 \ell_{\text{fuse}})(A_w + 2) f_{\text{comp}} \tag{C23}$$

$$\bar{c}_h = \frac{S_h}{b_h} \tag{C24}$$

$$A_h = \frac{b_h^2}{S_h} \tag{C25}$$

$$m_v g = f_{\text{comp}} [F_h S_h] \tag{C26}$$

Tables C10 and C11 list the variables to be optimized and constant parameters related to horizontal tail sizing.

Table C10: Horizontal tail sizing design variables

Quantity	Dimension	Description
A_h	-	horizontal tail aspect ratio
b_h	ft	horizontal tail span
$\bar{c}_h$	ft	horizontal tail mean aerodynamic chord
ℓ_h	ft	horizontal tail moment arm
m_h	lb	horizontal tail mass
S_h	ft^2	horizontal tail area

Table C11: Horizontal tail sizing constant parameters

Quantity	Value	Dimension	Description
F_h	250	N/m^2	horizontal tail mass factor
f_{comp}	-	1.0 / 0.855[C3]	composite mass scaling factor
$(t/c)_{\text{root}}$	0.10	-	airfoil thickness ratio

[C3]Values for conventional and composite tail design, respectively.

C.4.2 Horizontal Tail Performance

The horizontal tail drag is calculated as a function of Reynolds number, Mach number and tail thickness-to-chord ratio using a GP fit of TASOPT wing profile drag data [17].

$$\text{Re}_c = \frac{V_\infty \bar{c}}{\nu_\infty} \tag{C27}$$

$$
\begin{aligned}
C_{D_p,h}^{0.119392} = {} & 6.9696 \times 10^{-2} \left(\frac{\text{Re}_c}{1000}\right)^{-0.0021665} (100(t/c)_{\text{root}})^{0.104391} M_\infty^{-0.0177484} \\
& + 0.273439 \left(\frac{\text{Re}_c}{1000}\right)^{-0.0017356} (100(t/c)_{\text{root}})^{-0.164667} M_\infty^{-0.0233832} \\
& + 0.0001504 \left(\frac{\text{Re}_c}{1000}\right)^{-0.186771} (100(t/c)_{\text{root}})^{1.52706} M_\infty^{3.89794} \\
& + 0.27215 \left(\frac{\text{Re}_c}{1000}\right)^{-0.00170564} (100(t/c)_{\text{root}})^{-0.175197} M_\infty^{0.0242146} \\
& + 0.0608952 \left(\frac{\text{Re}_c}{1000}\right)^{-0.00195720} (100(t/c)_{\text{root}})^{0.22082} M_\infty^{-0.0439115}
\end{aligned}
\tag{C28}
$$

$$D_{p,h} = \tfrac{1}{2} \rho_\infty V_\infty^2 S_h C_{D_p,h} f_{\text{excr},h} \tag{C29}$$

$$D_h = D_{p,h} \tag{C30}$$

Tables C12 and C13 list the variables to be optimized and constant parameters related to horizontal tail performance.

Table C12: Horizontal tail performance design variables

Quantity	Dimension	Description
$C_{D_p,h}$	-	horizontal tail profile drag coefficient
D_h	lbf	horizontal tail drag
$D_{p,h}$	lbf	horizontal tail profile drag
Re_c	-	chord-referenced Reynolds number

Table C13: Horizontal tail performance constant parameters

Quantity	Value	Dimension	Description
$f_{\text{excr},h}$	1.0	-	horizontal tail excrescence drag factor

C.5 Vertical Tail Model

C.5.1 Vertical Tail Sizing

The vertical tail mass is calculated using the approximate tail area sizing and mass scaling described by Torenbeek [24].

$$S_v \ell_v = 0.03 \left(S_{\mathrm{ref}} b + 10 d_{\mathrm{fuse}}^2 \ell_{\mathrm{fuse}} \right) \tag{C31}$$

$$\bar{c}_v = \frac{S_v}{b_v} \tag{C32}$$

$$A_v = \frac{b_v^2}{S_v} \tag{C33}$$

$$m_v g = f_{\mathrm{comp}} \left[F_v S_v \right] \tag{C34}$$

Tables C14 and C15 list the variables to be optimized and constant parameters related to vertical tail sizing.

Table C14: Vertical tail sizing design variables

Quantity	Dimension	Description
A_v	-	vertical tail aspect ratio
b_v	ft	vertical tail span
$\bar{c}_v$	ft	vertical tail mean aerodynamic chord
ℓ_v	ft	vertical tail moment arm
m_v	lb	vertical tail mass
S_v	ft^2	vertical tail area

Table C15: Vertical tail sizing constant parameters

Quantity	Value	Dimension	Description
F_v	250	N/m^2	vertical tail weight factor
f_{comp}	-	1.0 / 0.855[C4]	composite mass scaling factor
$(t/c)_{\mathrm{root}}$	0.11	-	airfoil thickness ratio

[C4]Values for conventional and composite tail design, respectively.

C.5.2 Vertical Tail Performance

The vertical tail drag is calculated as a function of Reynolds number and tail thickness-to-chord ratio using a GP fit of TASOPT wing profile drag data [17].

$$\text{Re}_c = \frac{V_\infty \bar{c}_v}{\nu_\infty} \tag{C35}$$

$$C_{D_p,v}^{0.125} = 0.19\text{Re}_c^{0.0017}(t/c)_{\text{root}}^{0.0075} + 1.83 \times 10^4 \left(\frac{\text{Re}_c}{1000}\right)^{-0.494}(t/c)_{\text{root}}^{3.54}$$
$$+ 0.118\left(\frac{\text{Re}_c}{1000}\right)^{0.00165}(t/c)_{\text{root}}^{0.0082} + 0.198\left(\frac{\text{Re}_c}{1000}\right)^{0.00168}(t/c)_{\text{root}}^{0.00168} \tag{C36}$$

$$D_{p,v} = \tfrac{1}{2}\rho_\infty V_\infty^2 S_v C_{D_p,v} f_{\text{excr},v} \tag{C37}$$

$$D_v = D_{p,v} \tag{C38}$$

Tables C16 and C17 list the variables to be optimized and constant parameters related to vertical tail performance.

Table C16: Vertical tail performance design variables

Quantity	Dimension	Description
$C_{D_p,v}$	-	vertical tail profile drag coefficient
D_v	lbf	vertical tail drag
$D_{p,v}$	lbf	vertical tail profile drag
Re_c	-	chord-reference Reynolds number

Table C17: Vertical tail performance constant parameters

Quantity	Value	Dimension	Description
$f_{\text{excr},v}$	1.0	-	vertical tail excrescence drag factor

C.6 Nacelle Model

C.6.1 Nacelle Sizing

The TASOPT nacelle sizing model [17] is GP and is implemented directly.

$$S_{\text{nace}} = N_e r_{S_{\text{nace}}} \tfrac{1}{4}\pi d_{\text{fan}}^2 \tag{C39}$$

$$A_{\text{inlet}} = 0.4 S_{\text{nace}} \tag{C40}$$

$$A_{\text{fan cowl}} = 0.2 S_{\text{nace}} \tag{C41}$$

$$A_{\text{exh}} = 0.4 S_{\text{nace}} \tag{C42}$$

$$d_{\text{LPC}} = \tfrac{1}{3}d_{\text{fan}} \tag{C43}$$

$$A_{\text{core cowl}} = 3\pi d_{\text{LPC}}^2 \tag{C44}$$

$$m_{\text{nace}} = f_{\text{comp}}(\rho_{A_{\text{nace}}} S_{\text{nace}}) \tag{C45}$$

$$m_{\text{pylon}} = (m_{\text{nace}} + m_{\text{py,ref}}) f_{\text{pylon}} \tag{C46}$$

$$m = m_{\text{nace}} + m_{\text{pylon}} \tag{C47}$$

$$\ell_{\text{nace}} = 0.15 r_{S_{\text{nace}}} d_{\text{fan}} \tag{C48}$$

Tables C18 and C19 list the variables to be optimized and constant parameters related to nacelle sizing.

Table C18: Nacelle sizing design parameters

Quantity	Dimension	Description
$A_{\text{core cowl}}$	ft^2	core cowl area
A_{exhaust}	ft^2	exhaust area
$A_{\text{fan cowl}}$	ft^2	fan cowl area
A_{inlet}	ft^2	inlet area
d_{fan}	in	fan diameter
d_{LPC}	in	LPC diameter
ℓ_{nace}	ft	nacelle length
m	lb	nacelle + pylon mass
m_{nace}	lb	nacelle mass
m_{pylon}	lb	pylon mass
$m_{\text{py,ref}}$	lb	pylon reference mass
S_{nace}	ft^2	nacelle wetted area

Table C19: Nacelle sizing constant parameters

Quantity	Value	Dimension	Description
f_{comp}	1.0 / 0.925[C5]	-	composite mass scaling factor
f_{pylon}	0.1	-	pylon mass fraction
N_e	2 / 1[C6]	-	number of engines
$r_{S_{\text{nace}}}$	16.0	-	nacelle wetted-to-flow area ratio
$\rho_{A_{\text{nace}}}$	4.15	lb/ft^2	nacelle weight per wetted area

C.6.2 Nacelle performance

The TASOPT nacelle drag model [17] is GP and is implemented directly.

$$\text{Re}_{\text{nace}} = \frac{V_\infty \ell_{\text{nace}}}{\nu_{\text{inf}}} \tag{C49}$$

$$C_{f,\text{turb}} = \frac{0.074}{\text{Re}_{\text{nace}}^{0.2}} \tag{C50}$$

$$C_{f,\text{nace}} = f_{\text{excr,nace}} C_{f,\text{turb}} \tag{C51}$$

$$V_{n\text{LE}} = 1.2 r_{V_{\text{nac}}} V_\infty \tag{C52}$$

$$r_{V_{\text{surf}}^3} = 0.25 \left(\frac{V_{n\text{LE}}}{V_\infty} + r_{V_{\text{nace}}} \right) \left[\left(\frac{V_{n\text{LE}}}{V_\infty} \right)^2 + r_{V_{\text{nace}}}^2 \right] \tag{C53}$$

$$D_{\text{nace}} = \tfrac{1}{2} \rho_\infty V_\infty^2 S_{\text{nace}} r_{V_{\text{surf}}^3} C_{f,\text{nace}} \tag{C54}$$

Tables C20 and C21 list the variables to be optimized and constant parameters related to nacelle performance.

[C5]Values for conventional and composite nacelle design, respectively.

[C6]Values for under wing turbofan-generator and tail cone thruster nacelles, respectively.

Table C20: Nacelle performance design variables

Quantity	Dimension	Description
D_{nace}	lbf	nacelle drag
$C_{f,\text{nace}}$	-	nacelle skin friction coefficient
$C_{f,\text{turb}}$	-	turbulent skin friction coefficient
Re_{nace}	-	nacelle Reynolds number
$r_{V^3_{\text{surf}}}$	-	surface velocity ratio cubed
$V_{n\text{LE}}$	m/s	$V_{n\text{LE}}$

Table C21: Nacelle performance constant parameters

Quantity	Value	Dimension	Description
$f_{\text{excr,nace}}$	1.0	-	nacelle excrescence drag factor
$r_{V_{\text{nace}}}$	1.0	-	nacelle velocity ratio

C.7 Landing Gear Sizing Model

The landing gear mass is assumed to be proportional to vehicle max takeoff mass, m_{MTO}, decomposed into contributions from the nose and main gear.

$$m_{\text{main}} = f_{\text{LG,main}} m_{\text{MTO}} \tag{C55}$$

$$m_{\text{nose}} = f_{\text{LG,nose}} m_{\text{MTO}} \tag{C56}$$

$$m_{\text{gear}} = m_{\text{main}} + m_{\text{nose}} \tag{C57}$$

Tables C22 and C23 list the variables to be optimized and constant parameters related to landing gear sizing.

Table C22: Landing gear sizing design variables

Quantity	Dimension	Description
m_{gear}	lb	total landing gear mass
m_{main}	lb	main gear mass
m_{nose}	lb	nose gear mass

Table C23: Landing gear sizing constant parameters

Quantity	Value	Dimension	Description
$f_{\text{LG,main}}$	0.03	-	main gear mass fraction
$f_{\text{LG,nose}}$	0.007	-	nose gear mass fraction

C.8 Systems and Equipment Sizing Model

The systems and equipment mass is assumed to consist of a fixed mass and components proportional to max takeoff mass and payload mass.

$$m_{\text{equip}} = f_{\text{equip,mTO}} m_{\text{MTO}} + f_{\text{equip,pay}} m_{\text{payload}} + m_{\text{fix}} \tag{C58}$$

Tables C24 and C25 list the design variables to be optimized and constant parameters related to systems and equipment sizing.

Table C24: Systems and equipment sizing design variables

Quantity	Dimension	Description
m_{equip}	lb	systems and equipment mass

Table C25: Systems and equipment sizing constant parameters

Quantity	Value	Dimension	Description
$f_{\text{equip,mTO}}$	0.0557	-	equipment MTOW scaling
$f_{\text{equip,pay}}$	0.221	-	equipment payload scaling
m_{fix}	2500	lb	fixed mass

C.9 Operational Items Sizing Model

The operational item mass is assumed to consist of a fixed mass and a component proportional to payload mass.

$$m_{\text{items}} = f_{\text{items,pay}} m_{\text{payload}} + m_{\text{fix}} \tag{C59}$$

Tables C26 and C27 list the design variables to be optimized and constant parameters related to operational items sizing.

Table C26: Operational items sizing design variables

Quantity	Dimension	Description
m_{items}	lb	operational items mass

Table C27: Systems and equipment sizing constant parameters

Quantity	Value	Dimension	Description
$f_{\text{items,pay}}$	0.15	-	equipment payload scaling
m_{fix}	440	lb	fixed mass

References

1. Hepperle, M., "Electric Flight – Potential and Limitations," Workshop on Energy Efficient Technologies and Concepts Operation, 2012.

2. Drela, M., "Power Balance in Aerodynamic Flows," *AIAA Journal*, Vol. 47, No. 7, 2009, pp. 1761-1771.

3. Epstein, A.H., "Aeropropulsion for Commercial Aviation in the 21st Centuray and Research Directions Needed," 51st AIAA Aerospace Sciences Meeting including the New Horizons Forum and Aerospace Exposition, Aerospace Sciences Meetings, AIAA Paper 2013-0001, 2013.

4. National Academies of Sciences, Engineering, and Medicine, *Commercial Aircraft Propulsion and Energy Systems Research: Reducing Global Carbon Emissions*, National Academy Press, 2016.

5. Jansen, R.H., Bowman, C., Jankovsky, A., Dyson, R., and Felder, J., "Overview of NASA Electrified Aircraft Propulsion (EAP) Research for Large Subsonic Transports," 53rd AIAA/SAE/ASEE Joint Propulsion Conference, AIAA Propulsion and Energy Forum, AIAA Paper 2017-4701, 2017.

6. Uranga, A., Drela, M., Greitzer, E.M., Hall, D.K., Titchener, N.A., Lieu, M.K., Siu, N.M., Huang, A.C., Gatlin, G.M., and Hannon, J.A., "Boundary Layer Ingestion Benefit of the D8 Aircraft," *AIAA Journal,* Vol. 55, No. 11, 2017, pp. 3693-3708.

7. Smith, L.H., "Wake Ingestion Propulsion Benefit," *Journal of Propulsion and Power*, Vol. 9, No. 1, 1993, pp. 74-82.

8. Hall, D.K., Huang, A.C., Uranga, A., Greitzer, E.M., Drela, M., and Sato, S., "Boundary Layer Ingestion Benefit for Transport Aircraft," *Journal of Propulsion and Power,* Vol. 33, No. 5, 2017, pp. 1118-1129.

9. Straubel, J.B., "Energy Storage, EVs and the Grid," (Presentation), 2015 EIA Conference, 2015, https://www.eia.gov/conference/2015/pdf/presentations/straubel.pdf, Accessed August 2, 2016.

10. National Transportation Safety Board, "Auxiliary Power Unit Battery Fire Japan Airlines Boeing 787-8, JA829 Boston, Massachusetts January 7, 2013," (Incident Report), 2014, https://www.ntsb.gov/investigations/AccidentReports/Reports/AIR1401.pdf, Accessed August 2, 2016.

11. Airbus Group, "E-Fan The New Way to Fly," (Brochure), 2015, http://www.airbusgroup.com/service/mediacenter/download/uuid=48b1bd2c-a428-4c6, Accessed July 26, 2015.

12. Zhang, T., Imanishi, N., Shimonishi, Y., Hirano, A., and Takeda, Y., "A Novel High Energy Density Rechargeable Lithium/Air Battery," *Chemical Communications*, Vol. 46, 2010, pp. 1661-1663.

13. Bradley, M. K., and Droney, C. K., "Subsonic Ultra Green Aircraft Research: Phase I Final Report," NASA CR-2011-216847, April 2011.

14. Gibbs, Y., "NASA Armstrong Fact Sheet: NASA X-57 Maxwell," 2017, https://www.nasa.gov/centers/armstrong/news/FactSheets/FS-109.html, Accessed May 7, 2018.

15. Raymer, D.P., *Aircraft Design: A Conceptual Approach,* Fifth Edition, American Institute of Aeronautics and Astronautics, 2012.

16. Burnell, E., and Hoburg, W., "GPkit Software for Geometric Programming," https://github.com/convexengineering/gpkit, Version 0.7.0, 2018.

17. Drela, M., "TASOPT 2.00 Transport Aircraft System OPTimization: Technical Description," 2010, http://web.mit.edu/drela/Public/N+3/TASOPT_doc.pdf, Accessed May 8, 2018.

18. Zhang, X., and Haran, K., "High-Specific-Power Electric Machines for Electrified Transportation Applications – Technology Options," IEEE Energy Conversion Congress and Exposistion (ECCE), 2016.

19. Farve, N., "Design of a Low-Mass High-Torque Brushless Motor for Application in Quadruped Robotics," S.M. Thesis, Massachusetts Institute of Technology, Cambridge, MA, 2012.

20. Ofori-Tenkorang, J., "Permanent-Magnet Synchronous Motors and Associated Power Electrics for Direct-Drive Vehicle Propulsion," Ph.D. Dissertation, Massachusetts Institute of Technology, Cambridge, MA, 1996.

21. Riddle, R.R., and Dix. D.M., *Technology Assessment of Advanced Propulsion Systems for Some Classes of Combat Vehicles, Volume III*, Institute for Defense Analyses, 1979.

22. Welstead, J.R., and Felder, J.L., "Conceptual Design of a Single-Aisle Turboelectric Commercial Transport with Fuselage Boundary Layer Ingestion," 54th AIAA Aerospace Sciences Meeting, AIAA SciTech Forum, AIAA Paper 2016-1027, 2016.

23. Welstead, J., Felder, J., Guynn, M., Haller, B., Tong, M., Jones, S., Ordaz, I., Quinlan, J., and Mason, B., "Overview of the NASA STARC-ABL (Rev. B) Advanced Concept," One Boeing NASA Electric Aircraft Workshop, March 2017.

24. Torenbeek, E., *Advanced Aircraft Design: Conceptual Design, Analysis, and Optimization of Subsonic Civil Airplanes,* The Netherlands: Delft University of Technology, 2013.

25. Schaufele, R. D., *The Elements of Aircraft Preliminary Design,* Aries Publications, 2000.

26. Greitzer, E. M., Bonnefoy, P. A., de la Rosa Blanco, E., Dorbian, C. S., Drela, M., Hall, D. K., Hansman, R. J., Hileman, J. I., Liebeck, R. H., Lovegren, J., Mody, P., Pertuze, J. A., Sato, S., Spakovszky, Z. S., Tan, C. S., Hollman, J. S., Duda, J. E., Fitzgerald, N., Houghton, J., Kerrebrock, J. L., Kiwada, G. F., Kordonowy, D., Parrish, J. C., Tylko, J., and Wen, E. A., "N+3 Aircraft Concept Designs and Trade Studies, Final Report," NASA CR-2010-216794, December 2010.

27. Qu, R., and Lipo, T.A., "Analysis and modeling of air-gap and zigzag leakage fluxes in a surface-mounted permanent-magnet Machine." *IEEE Transactions on Industry Applications.* Vol. 40, No. 1, pp. 121-127, Feb 2004.

28. Ilic, M., "Multi-layered interactive energy space modeling for near-optimal electrification of aircraft systems," LEARN Final Report, to appear.